Doctoral theses at NTNU, 2024:7

Atousa Elahidoost

Stability Improvement of MMC-Based Multiterminal HVDC Grids

Doctoral thesis

NTNU
Norwegian University of Science and Technology
Thesis for the Degree of Philosophiae Doctor
Faculty of Information Technology and Electrical Engineering
Departement of Electric Energy

NTNU
Norwegian University of Science and Technology

Atousa Elahidoost

Stability Improvement of MMC-Based Multiterminal HVDC Grids

Thesis for the Degree of Philosophiae Doctor

Trondheim, January 2024

Norwegian University of Science and Technology
Faculty of Information Technology and Electrical Engineering
Departement of Electric Energy

NTNU
Norwegian University of
Science and Technology

NTNU
Norwegian University of Science and Technology

Thesis for the Degree of Philosophiae Doctor

Faculty of Information Technology and Electrical Engineering
Departement of Electric Energy

ISBN 978-82-326-7614-9 (printed ver.)
ISBN 978-82-326-7613-2 (electronic ver.)
ISSN 1503-8181 (printed ver.)
ISSN 2703-8084 (online ver.)

Doctoral theses at NTNU, 2024:7

Printed by NTNU Grafisk senter

Abstract

The 100% renewable European smart grid cannot be implemented without reliance on wind energy from the offshore wind farms in the North Sea. High-voltage direct current (HVDC) cables are generally used to transfer power from long-distance offshore wind farms to onshore grids at relatively low costs and energy loss. According to European expansion planning scenarios, the interconnection and expansion of the existing and newly built offshore point-to-point HVDC grids in the North Sea are inevitable. Implementation of the multiterminal HVDC grid configuration demands control measures to ensure grid stability since such grids were not initially designed to be multiterminal. Hence, dynamic interactions, either on the AC- or DC-side of the multiterminal grid, can be a source of detrimental oscillations and propagate to the entire network due to the droop control action of the HVDC converters, resulting in stability deterioration, faults, and subsequent blackouts with considerable damages and costs.

This thesis aims to present an optimal analytical methodology to improve the stability of the multiterminal HVDC grids, focusing on offshore wind applications. The analysis is performed in MMC-based HVDC grids, the preferred offshore technology, to account for the converter's control and dynamic challenges and opportunities originating from the arm capacitor energies.

First, a centralized optimal linear feedback controller is introduced to ensure network stability under the worst-case perturbation scenario. The main aim of the centralized optimal controller is to minimize the oscillations caused by the poorly damped modes under the worst-case perturbation scenario while considering the constraints on the control inputs and state variables. The optimal controller can be found by running the optimization problem formulation once without analyzing the time-consuming dynamic and transient time-domain simulations for different scenarios. Additionally, there will be no need for repetitive tuning of the grid controllers under the interconnection and expansion procedure since the optimal controller alone can guarantee stability. The performance of the centralized optimal controller in minimizing DC voltage oscillations is investigated via small-signal eigenvalue stability analysis and time-domain simulations. DC voltage stability is a sign of power balance in multiterminal HVDC grids, and DC voltage oscillations can propagate to connected networks due to the droop control action and lead to voltage instability and faults, ultimately resulting in blackouts with significant costs. This thesis shows that the centralized optimal controller can ensure DC voltage stability under the worst-case perturbation scenario when implemented either in the presence or absence of the droop control gain, i.e., it can optimally readjust or substitute the droop gain in a multiterminal configuration to improve

DC voltage stability.

Second, the centralized optimal controller is replaced by the decentralized one to create the desired sparsity pattern such that there is no need for long-distance data communication between converter stations, resulting in a more reliable and stable solution. In the decentralized problem formulation, the constraints on the initial state variables' perturbations and control inputs can be decoupled, which is physically more practical and sensible. This thesis investigates the applicability of the decentralized optimal controller in reducing oscillations caused by the poorly damped modes under the worst-case perturbation scenario and decoupled grid control inputs' and state variables' constraints in MMC-based multiterminal hybrid AC/DC grids. It is shown via the eigenvalue stability analysis and time-domain simulations that the proposed decentralized optimal controller can efficiently enhance the grid stability margins and reduce the oscillations, not only under the worst-case perturbation scenario but also under other critical fault conditions. Furthermore, the controller's superior performance is validated in the absence or presence of the power system stabilizer (PSS) and MMC droop controller under small and large disturbances, and its robustness is assessed against the uncertainties in control parameters, grid parameters, and operating conditions under the disturbances on the AC- and DC-side of the grid.

Finally, this thesis introduces a stability (oscillation) index that can be integrated into the transmission expansion planning (TEP) problems as a further decision-support criterion in the preliminary stages of expansion planning in multiterminal HVDC grids. This index can identify the HVDC link placement among several options with minimum oscillations on critical and poorly damped state variables under the worst-case perturbation scenario. For instance, the DC voltage oscillation index is applied as a potential decision-support criterion for placing a new HVDC link between two independent point-to-point MMC-based offshore HVDC grids while considering the wind intermittency effect on grid operating conditions.

Acknowledgements

This thesis summarizes the research conducted during my PhD study at the Department of Electric Energy at the Norwegian University of Science and Technology (NTNU). The PhD was partially supported by the Norwegian Research Council and the DNV GL Group through the IDeCON "Integrated Approach to Design and Control of Offshore HVDC Networks" Project.

First and foremost, I would like to express my sincere gratitude to my supervisor Professor Elisabetta Tedeschi for providing me with this great opportunity to work on this topic and for her continuous encouragement and invaluable support. I cannot thank her enough for being such a wonderful supervisor throughout the PhD period; her insight, guidance, and constructive feedback have always been precious in my learning path. I would also like to thank my co-supervisor, Dr Maider Santos – Mugica from the Energy and Environment Division at Tecnalia in Spain, for her support in giving me a chance as a guest researcher to spend six months at Tecnalia.

I would like to extend my deepest gratitude to Professor Maryam Kamgarpour and Postdoctoral researcher Luca Furieri from EPFL for their fruitful collaboration and technical support. I am particularly grateful to Professor Maryam Kamgarpour for her advice and feedback in effectively presenting my research work.

I would like to express my appreciation to all my colleagues and friends at NTNU who helped me throughout my research work and for all the memorable moments at lunchtime and coffee breaks. I am grateful to Professor Gilbert Bergna-Diaz for his advice and guidance on MMC modeling methodologies. My special thanks go to my colleague Dr Abel Assegid Taffese, who always found time to help me with my technical questions and give me the most to-the-point answers, and to my office-mates Razieh Nejati Fard, Erick Fernando Alves, Spyridon Chapaloglou, and Babak Abdolmaleki for being such good friends. I finalized the thesis while working for Norske tog, and I would like to thank everyone there for their support in providing me with the time I needed to finish writing my thesis.

Finally, I would like to thank my family. They have always supported and believed in me, and words cannot express how grateful I am for all their love and motivation. Last but not least, my husband, Ali, deserves my most profound appreciation for his endless love and invaluable support during my PhD studies. My thanks for all his patience and for believing in me. Moreover, it is impossible not to mention my beloved daughter, Ariana, who is my true source of energy and encouragement.

Contents

List of Tables

List of Figures

List of Symbols

Acronyms

AAM	Average Arm Model
AC	Alternating Current
AVR	Automatic Voltage Regulator
CB	Circuit Breaker
CCSC	Circulating Current Suppression Control
DAE	Differential and Algebraic Equations
DC	Direct Current
DER	Distributed Energy Resources
EMT	Electromagnetic Transient
ESS	Energy Storage System
FC	Flying Capacitor
GEI	Global Energy Interconnection
HTG	Hydro Turbine Governor
HVAC	High Voltage Alternating Current
HVDC	High Voltage Direct Current
KVL	Kirchhoff's Voltage Law
IED	Intelligent Electronic Device
IGBT	Insulated-Gate Bipolar Transistor
LCC	Line Commutated Converter
LMI	Linear Matrix Inequality
LPF	Low Pass Filter
MMC	Modular Multilevel Converter
MPC	Model Predictive Control
NPC	Neutral Point Clamped
NSOG	North Sea Offshore Grid
PCC	Point of Common-Coupling
PCI	Projects of Common Interest

PHIL	Power Hardware In the Loop
PLL	Phase-Locked Loop
POD	Power Oscillation Damping
PSS	Power System Stabilizer
PWM	Pulse Width Modulation
REC	Renewable Energy Curtailment
RMS	Root Mean Square
SCR	Short Circuit Ratio
SDP	Semi-Definite Programming
SISO	Single-Input-Single-Output
SM	Submodule
SSTI	Steady-State Time-Invariant
SSTP	Steady-State Time-Periodic
TEP	Transmission Expansion Planning
THD	Total Harmonic Distortion
ULM	Universal Line Model
VSC	Voltage Source Converter

Parameters and variables

MMC and HVDC cable modelling

Z_b^{ac}, Z_b^{dc}	AC-side and DC-side base impedances
L_b^{ac}, L_b^{dc}	AC-side and DC-side base inductances
R_a, L_a	Arm resistance and inductance
r_a, l_a	Per-unit arm resistance and inductance
R_t, L_t	Transformer resistance and inductance
R_{ac}, L_{ac}	Equivalent AC resistance and inductance
r_{ac}, l_{ac}	Per-unit equivalent AC resistance and inductance
R_{dc}, L_{dc}	Equivalent DC cable resistance and inductance
r_{dc}, l_{dc}	Per-unit equivalent DC cable resistance and inductance
C_b^{ac}, C_b^{dc}	AC-side and DC-side base capacitances
C_{sm}	Submodule capacitance
C_a	Equivalent arm capacitance
c_a	Per-unit equivalent arm capacitance
C_{dc}	Equivalent DC-side capacitance
c_{dc}	Per-unit equivalent DC-side capacitance
N	Number of submodules in each arm
$N_{ins,u}$, $N_{ins,u}$	Number of inserted upper and lower arm submodules
n_u, n_l	Upper and lower arm insertion indices

n_Δ, n_Σ	Differential and common-mode insertion indices
S_{rated}	Rated apparent power
S_b	Base apparent power
V_{rated}	Rated voltage
V_b^{ac}, V_b^{dc}	AC-side and DC-side base voltages
v_g	AC grid Thevenin equivalent (generator) voltage
v_{dc}	Voltage at DC terminals of the converter
v_u, v_l	Upper and lower arm output voltages
v_{cu}, v_{cl}	Upper and lower arm capacitor voltages sum
v_{ac}, v_c	Differential (AC-side) and common-mode voltages
v_Δ, v_Σ	Differential and common-mode arm capacitor voltages sum
$v_{smi,u}$, $v_{smi,l}$	i^{th} upper and lower arm SM capacitor voltages
v_{norm}	Normalizing voltage
I_b^{ac}, I_b^{dc}	AC-side and DC-side base currents
i_u, i_l	Upper and lower arm output currents
i_{ac}, i_c	Differential (AC-side) and common-mode (circulating) currents
i_{dc}	DC-side current
W_b	Base arm capacitor energy
w_u, w_l	Upper and lower arm capacitor energies
w_Δ, w_Σ	Arm capacitor energy difference and sum
p_{ac}, q_{ac}	Active and reactive powers
ρ	DC voltage droop gain
θ_g	Reference frame (generator) angle
θ_{pll}	PLL angle
ω_g	Reference frame angular frequency/velocity
ω_{pll}	PLL angular frequency/velocity
k_p, k_i	PI controller proportional and integral gains
T_f	LPF time constant
T_{conv}	Converter PWM delay
ξ	PI controller integral state
$(.)^*$	Reference value
$(.)^{conj}$	Complex conjugate operator
$(.)_{pu}$	Per-unit value
d, q	Direct and quadrature components

Small-signal eigenvalue analysis

$\mathbf{x}$, $\mathbf{u}$, $\mathbf{z}$	State, control input, and output vectors
$\mathbf{A}$, $\mathbf{B}$, $\mathbf{C}$, $\mathbf{D}$	State, control input, output, and feedforward matrices
λ, σ, ζ	Eigenvalue, damping, and damping ratio

$\mathbf{\Phi}$, $\mathbf{\Psi}$	Right and left eigenvectors
$\mathbf{\Lambda}$	Diagonal matrix of the matrix $\mathbf{A}$ eigenvalues
$\mathbf{P}$, p_{ik}	Participation matrix, and participation factor

Optimal linear feedback controller

J_{osci}	Oscillation index
$\mathbf{K}$	Optimal linear feedback controller
n, m	Number of the grid state variables and control inputs
$\mathbf{E_x}$, $\mathbf{E_u}$	Symmetric positive definite matrices
r	Number of the grid state variables' ellipsoidal constraints
q	Number of the grid control inputs' ellipsoidal constraints
$\mathbf{P}$	Unique solution of the Lyapunov equation
$\mathbf{Y}$, $\mathbf{Q}$	Matrices such that $\mathbf{Q} = \mathbf{P}^{(-1)}$ and $\mathbf{Y} = \mathbf{KQ}$
s_i, y_i, and w	Decision variables

AC grid modelling

ω_m, δ	Rotor angular velocity and position
ψ_{fd}, ψ_{1d}, ψ_{1q}, ψ_{2q}	Per-unit rotor flux linkages
γ	PI controller integral state

Chapter 1

Introduction

1.1 Background and motivation

The 100% renewable European smart grid cannot be achieved without relying on the wind energy from the offshore wind farms in the North Sea [1, 2]. High Voltage Direct Current (HVDC) technology is currently the best solution for transferring renewable energy over long subsea distances at higher energy efficiency and lower costs than the conventional High Voltage Alternating Current (HVAC) technology [3]. In other words, HVDC grids are playing a pivotal role in the green shift towards the carbon-free renewable energy-based power system. This paradigm is due to the significant evolution of the HVDC technology in recent years, resulting in higher power capacity and improved control and protection methodologies [4]. Hence, HVDC grids have become a viable solution for realizing the multiterminal configuration interconnecting offshore wind farms and onshore grids, as well as synchronous and asynchronous zones over ultra-long distances [3].

As yet, there are two primary converter technologies for HVDC power transmission: Line Commutated Converter (LCC) and Voltage Source Converter (VSC). The former has the advantage of higher power and voltage rating compared to the latter one. Until now, the largest LCC-based grid reported has a power/voltage rating of 12 GW/$\pm$1100 kV [5] whereas the largest VSC-based HVDC grid, which is under construction as a three-terminal HVDC system in China, is rated at 5 GW/$\pm$800 kV [6]. Recent developments in power electronics, particularly wide band-gap semiconductors, are expected to narrow the technological gap between the VSC and LCC from the power/voltage capacity standpoint. Furthermore, VSC-converters are superior in terms of power flow control and AC/DC fault handling, making them the most feasible alternative for multiterminal HVDC grid configur-

ations [3].

The Modular Multilevel Converter (MMC) has emerged as the most promising VSC for HVDC applications. The main characteristics of the MMC are modularity, voltage, and power scalability, and high-quality output waveforms with low Total Harmonic Distortion (THD) [7]. The converter technology is fault-tolerant with a transformer-less operation and can provide ancillary grid services such as frequency and voltage support [8]. Currently, MMC-based HVDC transmission systems are commercialized and realized from point-to-point to multiterminal configurations, particularly in offshore wind farm applications. For instance, offshore wind farms in the North Sea are generally connected to the onshore AC networks through MMC-based point-to-point HVDC grids [9]. Commercialized MMC-based multiterminal HVDC grids can be identified in China, such as the three-terminal Nanao project for delivering wind power from the island of Nanao to the mainland and the five-terminal Zhoushan project for distributing power among different regions [7, 10, 11].

MMC-based HVDC grids are envisioned as the backbone for future power systems and the realization of a Global Energy Interconnection (GEI) to exchange a high amount of power over ultra-long distances worldwide. Interconnection of the currently operating and future HVDC grids, given the former may have been designed and developed without initial detailed studies on different aspects of grid expansion, can impose interoperability issues, including control interactions and stability challenges. Such dynamic interactions can propagate throughout the entire network, resulting in instability, faults, and eventual blackouts with significant damages and costs. As the wind energy association Wind Europe explained:

> Grid stability will also become one of the major power system challenges in the following decades. Real-time observability and controllability are basic needs to integrate renewables and a must for incentivizing the participation of renewables in system service. Today renewables are marginally modelled and represented in Network Management Systems; their characteristics and controls are not adequately integrated. As a result, their potential cannot be fully exploited for optimizing grid operation [12].

Within the same analysis, unveiling the pivotal role of grid optimization technologies (including HVDC systems) to make massive wind exploitation viable, they underline that:

> The use of such technologies and their foreseen benefits should also be reflected in the system planning mechanism and system operation.

> Their wide deployment would not only accelerate renewables integration but could also contribute to deferring particular grid expansion or reinforcement projects, reducing new transfer capacity needs (e.g. new corridors) or reducing re-dispatching and renewables' curtailment needs [12].

Traditional Transmission Expansion Planning (TEP) approaches aim to determine the installation plan for new facilities (type, number, place, and time) to meet the anticipated energy demand while minimizing cost and losses and considering reliability constraints [13]. However, TEP strategies need to evolve to capture the HVDC grids' technical characteristics to properly exploit their advantages and reflect their challenges, which are distinct from conventional AC networks.

Such recognized system needs open new perspectives and highlights research gaps, among which is the one effectively summarized in [12]:

> Certainly, adapting system planning to reflect new needs given the whole spectrum of short- and long-term uncertainties is a very challenging task. From a technical point of view, how can we capture the difference between the prospective system (planned system) and the real-time conditions during actual operations?

This PhD work stems from a reflection on the above-presented aspects and emerging research needs, and it recognizes that to properly integrate HVDC stability, control, and operational considerations into system planning, efficient tools to adjust system planning decisions to evolving optimization needs [12], as well as reliable simulation models to accurately represent the dynamic interactions and instability sources in complex AC/DC systems are crucial. From this perspective, the capability of identifying, during expansion planning, the worst-case scenario that could arise from the interconnections and dynamic interactions and the possibility of an early design of optimized control strategies to assure the grid stability in such conditions are of great relevance.

Therefore, this thesis primarily focuses on developing an optimal controller for improving the stability in MMC-based multiterminal HVDC grids. Moreover, it also aims to propose a stability decision-support criterion for TEP analysis to address the abovementioned research gap.

1.2 Scope of the thesis

The work of this thesis contributes to establishing a more stability-informed approach to expansion planning for hybrid AC/DC high voltage transmission systems

integrating large amounts of intermittent renewable sources. It does so by:

- Introducing a stability index to be integrated into TEP as a further decision-support criterion.
- Identifying the worst-case scenarios, which are of paramount importance in grid planning stages, for different configurations and with no need for long simulations.
- Designing an optimal controller that can enhance stability in MMC-based HVDC/AC grids and outperform traditional controllers under the worst-case scenarios and other operational conditions.

This PhD work has been developed in three different stages to achieve this overarching goal, characterized by a growing level of complexity and generality:

The first stage goal is to introduce a potential stability criterion for TEP problems to distinguish the HVDC link placement among several options that gives minimum DC voltage oscillations under the worst-case-perturbation scenario while considering the renewables intermittency effect. Therefore, the research question group at this stage is defined as below.

Research question group 1: How can we define a potential stability decision-support criterion that can quantify DC voltage oscillations under the worst-case perturbation scenario to be applicable for TEP problems? How can the wind intermittency effect be considered in the stability index calculation?

The second stage focuses on developing a methodology for an optimal controller to maximize stability under the worst-case perturbation scenario in VSC-based multiterminal HVDC grids. Namely, the controller should ensure multiterminal HVDC grids' stability when the worst-case perturbation scenario occurs while eliminating the need to build up dynamic models and operating time-consuming simulations for readjusting and retuning control parameters during expansion planning. To this end, the following research question group is addressed by the thesis at this stage.

Research question group 2: Which methodology should be applied that can efficiently identify an optimal controller together with the worst-case perturbation scenario? How can we define the optimal controller objective and variables prone to oscillations and instability? How can the optimal controller be reliably configured to overcome long-distance communication delays and failures?

In the third stage, the applicability and performance of the optimal controller in minimizing the oscillations under the worst-case perturbation scenario are invest-

igated in an MMC-based multiterminal HVDC grid and then a more realistic case of an MMC-based multiterminal hybrid AC/DC grid through detailed analysis and simulations. Moreover, the dynamic interactions between/within AC and DC subgrids are analyzed to recognize the dominant modes responsible for oscillations and instability. Thus, the research question group stated in the last stage is given as follows.

Research question group 3: How does the optimal controller perform in minimizing the oscillations under the worst-case perturbation scenario as well as in a broader range of dynamics and transients? How robust is the optimal controller against parametric uncertainties in the grid? What are the dynamic interactions between/within AC and DC subgrids?

1.3 Main scientific contributions

This thesis has resulted in the main contributions summarized as follows.

- **Presenting a centralized optimal linear feedback controller:** An analytical control methodology is presented to ensure multiterminal HVDC grid stability by minimizing the oscillations of critical variables under the worst-case perturbation scenario. The possibility of analytically and simultaneously identifying the worst-case perturbation/oscillation scenario and designing an appropriate stabilizing controller can benefit HVDC grids expansion planning when a multitude of parameters and variables are to be contemplated, and detailed and time-consuming dynamic simulations of all the scenarios are prohibitive. Namely, the optimization formulation is initially inspired by the approach presented in [14, 15], which evaluates the placement of HVDC links for AC grid reinforcement by minimizing the generator frequency deviations. However, the control methodology is further adapted to the thesis's primary objective, which is the minimization of the DC voltage oscillations in multiterminal HVDC grids. DC voltage oscillations can affect the power balance in multiterminal HVDC grids. Moreover, DC voltage oscillations can propagate to connected AC networks due to the conventional droop control action and lead to voltage instability and faults, resulting in high-cost blackouts. Therefore, a centralized optimal linear feedback controller is developed to achieve the abovementioned objective under the worst-case perturbation scenario while considering system physical constraints such as converter current rating. Its performance is evaluated via the small-signal eigenvalue stability analysis and time-domain simulations.

- **Applying a decentralized optimal linear feedback controller:** The de-

centralized optimal linear feedback controller eliminates the need for long-distance communication between converter stations, which may result in delays and failure. The decentralized optimal controller is supposed to be more reliable than the centralized one by only relying on local information. Moreover, system physical constraints are naturally decoupled, allowing for more flexibility and sensibility in the design. The performance of the decentralized optimal linear feedback controller is evaluated in minimizing DC voltage oscillations under the worst-case perturbation scenario through the small-signal eigenvalue stability analysis and time-domain simulations. Furthermore, the applicability of the optimal controller is investigated in minimizing oscillations caused by the grid dominant modes that are poorly damped under the worst-case perturbation scenario in a more realistic case of an MMC-based multiterminal hybrid AC/DC grid. Its performance is assessed against small and large disturbances, and its robustness is validated against parametric uncertainties.

- **Introducing a stability-based decision-support criterion for TEP analysis:** A potential stability decision-support criterion is introduced that can identify the HVDC link placement with minimum oscillations on critical variables among several options under the worst-case perturbation scenario while considering the wind intermittency effect on grid operating conditions. The stability index can be implemented in the preliminary stages of the expansion planning for multiterminal HVDC grids.

1.4 Overview of the publications

The following papers have been published as part of the PhD research:

P1 A. Elahidoost and E. Tedeschi, "Expansion of offshore HVDC grids: An overview of contributions, status, challenges and perspectives," *2017 IEEE 58th International Scientific Conference on Power and Electrical Engineering of Riga Technical University (RTUCON)*, 2017, pp. 1-7, doi: 10.1109/RTUCON.2017.8124767 [9].

P2 A. Elahidoost, L. Furieri, E. Tedeschi and M. Kamgarpour, "Optimizing HVDC grid expansion and control for enhancing DC stability," *2018 Power Systems Computation Conference (PSCC)*, 2018, pp. 1-7, doi: 10.23919/PSCC.2018.8442753 [16].

P3 A. Elahidoost, L. Furieri, E. Tedeschi and M. Kamgarpour, "Reducing HVDC network oscillations considering wind intermittency through optimized grid

expansion decision," *2018 IEEE Energy Conversion Congress and Exposition (ECCE)*, 2018, pp. 2683-2690, doi: 10.1109/ECCE.2018.8557546 [17].

P4 A. Elahidoost and E. Tedeschi, "Control optimization of the offshore HVDC grid based on modular multilevel converter for improving DC voltage stability," 18^{th} *International Conference on Renewable Energies and Power Quality (ICREPQ'20),* later republished in The *Renewable Energy & Power Quality Journal (RE&PQJ)*, vol. 18, no. 273, 2020, pp. 207–212, doi: 10.24084/ repqj18.273 [18].

P5 A. Elahidoost, L. Furieri, M. Kamgarpour and E. Tedeschi, "Optimal linear controller for minimizing DC voltage oscillations in MMC-based offshore multiterminal HVDC grids," *in IEEE Access*, vol. 9, pp. 98731-98745, 2021, doi: 10.1109/ACCESS.2021.3096291 [19].

P6 A. Elahidoost and E. Tedeschi, "Stability improvement of MMC-based hybrid AC/DC grids through the application of a decentralized optimal controller," *IET Gener. Transm. Distrib.* 00, 1– 19 (2022), doi: 10.1049/gtd2.12497 [20].

The abovementioned publications contribute to the content of the thesis, as presented in the following table.

Table 1.1: Thesis chapters and publications.

Chapter	2	3	4	5	6
Publication	P1	P4, P5, P6	P2, P3, P5, P6	P4, P5	P6

1.5 Outline of the thesis

Chapter 2 presents the existing and planned HVDC grids and their converter technologies in the North Sea. Next, the role of the multiterminal HVDC grids in the future smart grids and their potential configurations and topologies are introduced. Finally, HVDC grids' expansion challenges and research requirements are investigated.

Chapter 3 deals with the modeling and control of the HVDC grids. The MMC modeling technique, together with its control strategy applicable to large power systems with a sufficient degree of accuracy, is presented. Additionally, the HVDC cable model suitable for the state-space representation is reintroduced. Lastly, the background knowledge associated with the small-signal eigenvalue stability analysis is reviewed.

The chapter's primary goal is to present the theory and modeling principles required in the subsequent chapters.

Chapter 4 presents an analytical optimization methodology to minimize the oscillations caused by the poorly damped modes under the worst initial perturbation scenario by an optimal controller. Moreover, a stability index is introduced to measure the oscillations under the worst-case perturbation scenario that can be implemented as a decision-support criterion in TEP problems. It is shown that the proposed centralized optimal linear feedback controller can be developed into a decentralized configuration to eliminate the need for communication among converter stations to improve reliability and mitigate delays. Furthermore, the constraints on the control inputs and state variables can be decoupled to enhance the feasibility and tractability of the methodology. Finally, to evaluate the applicability of the introduced optimization methodology in TEP problems, the placement of a new HVDC link between two independent 2-level VSC-based point-to-point HVDC grids in the North Sea is assessed while using the actual wind data for accounting for the wind intermittency effect. The goal is to include the DC voltage stability maximization under the worst-case perturbation scenario as an additional support criterion in a multi-objective optimization for the HVDC network expansion decision.

Chapter 5 explores the minimizing of DC voltage oscillations under the worst-case perturbation scenario in an MMC-based offshore four-terminal HVDC grid that is considered as the study case. First, challenges associated with the MMC's internal dynamics due to the arm capacitor voltages and circulating currents in the expansion of the multiterminal HVDC grids are investigated. Second, the performance of the centralized and decentralized optimal linear feedback controllers in minimizing the DC voltage oscillations is evaluated/compared under different scenarios in the presence or absence of the droop control function. This is ascertained via small-signal eigenvalue stability analysis and time-domain simulations.

Chapter 6 outlines how the stability of multiterminal hybrid AC/DC grids can be ensured via the decentralized optimal controller. The introduced methodology analytically identifies both the decentralized optimal controller and the worst-case perturbation scenario under the grid control inputs' and state variables' constraints without the need for detailed and time-consuming dynamic simulations of all possible scenarios. First, eigenvalue stability analysis and time-domain simulations

are performed to show that the proposed controller can efficiently enhance the test grid stability margins and reduce the oscillations, not only under the worst-case perturbation scenario but also under other critical fault conditions. Furthermore, the controller's superior performance is validated through comparison with the power system stabilizer (PSS) and MMC droop controller under small and large disturbances. Finally, the controller's robustness is assessed against uncertainties in control and grid parameters and operating conditions.

Chapter 7 summarizes the main findings of the thesis and presents its conclusions.

Chapter 2

Multiterminal HVDC grids

2.1 Introduction

In recent years, the idea of a global smart grid based on Distributed Energy Resources (DER), especially renewables, has been widely evolving. The motivation for integrating renewables into the global energy network is not only to meet the increasing energy demand but also to improve energy availability, reliability, security, and quality, as well as to compensate for the adverse impact of fossil fuels on global warming. To this end, several scenarios have been proposed for achieving a 100% renewable power system in Europe by 2050, including e-Highway 2050 [1], Energy Revolution (5^{th} Edition) [21], EU Energy Roadmap 2050 [22], Re-thinking 2050 [23], and Roadmap 2050 [24].

Among renewables, wind energy plays a significant role in the effort to meet the 2050 European climate target, given that the North Sea is an enormous source of offshore wind power [9]. Accordingly, it is expected that wind alone can supply about half of the European energy demand by 2050 [12]. Compared to the conventional AC one, HVDC transmission is currently the best solution for transferring a high amount of wind energy from offshore wind farms to the onshore power grid at reasonable costs and losses over long distances [25]. Hence, an AC-DC converter is required to convert the standard AC generation to HVDC for power transmission at the offshore wind farm, and a DC-AC converter is needed to convert it back to AC at the onshore power grid. A conventional point-to-point HVDC grid configuration is shown in Fig. 2.1.

The applicability of the HVDC grid is thus reliant on the development of power converters. The invention and improvement of the Insulated-Gate Bipolar Tran-

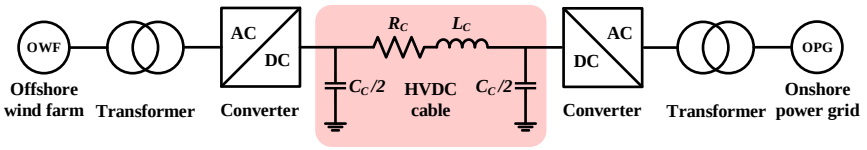

Figure 2.1: Conventional point-to-point HVDC grid configuration.

sistor (IGBT) revolutionized HVDC transmission by introducing VSC technology with the series connection of IGBTs to reach the required high DC voltage. Indeed, VSC-based HVDC technology is superior to the LCC-based one from many perspectives, including independent active and reactive power control, black start capability, the smaller size of the converter station, and standard transformer compatibility [25]. The introduction of the MMC in the early 2000s was a significant breakthrough in VSC-based HVDC applications. Ever since, MMC has become the preferred VSC technology in HVDC transmission due to its modularity and scalability, high-energy efficiency, and the high quality of the produced current and voltage waveforms, which eliminates the need for filters and reduces losses [26]. Hence, all these characteristics have made the VSC-based HVDC technology an attractive and viable solution for multiterminal grid configuration. There have not been many multiterminal VSC-based HVDC grids in service worldwide until recently. China is the leading country with the ± 160 kV three-terminal Nanao, ± 200 kV five-terminal Zhoushan, and ± 500 kV four-terminal Zhangbei VSC-based HVDC grids [3].

The point-to-point connection, which is the conventional configuration for the existing and planned offshore HVDC grids in the North Sea, is expected to gradually evolve into multiterminal/meshed networks as a prerequisite for the 100% renewable European power system. The interconnection of the independently developed point-to-point offshore HVDC grids with different technologies may introduce interoperability issues caused by control interactions and stability challenges [3, 9]. Therefore, this chapter begins by reviewing the existing and planned offshore HVDC grids in the North Sea. Next, the role of multiterminal HVDC grids in the future smart grid and their various configurations and topologies are introduced. Finally, potential technical challenges and research opportunities arising from the gradual interconnection and expansion of the HVDC grids are discussed.

2.2 HVDC grids in the North Sea

The currently existing and future planned offshore HVDC grids in the North Sea are shown in Fig. 2.2, and their characteristics are summarized in Table 2.1. The data used to create the figure and table were extracted either from the "https://www.wikipedia .org/" or "https://www.4coffshore.com/" web sites or manufacturers' fact sheets [27, 28, 29, 30, 31, 32, 33, 34, 35, 36, 37, 38, 39, 40, 41, 42, 43].

As is apparent from Fig. 2.2 and Table 2.1, all the offshore HVDC grids in the North Sea are of the point-to-point configuration. They are mainly used to transfer power from offshore wind farms to onshore power grids or between two onshore locations separated by the North Sea. The HVDC grids under operation with the highest capacity are the NordLink (Norway – Germany) and the North Sea Link (Norway – United Kingdom), with a power transfer capability of 1.4 GW, whereas the Eastern Link in the United Kingdom is planned to be commissioned by 2024 with a 2 GW capacity. The longest HVDC submarine cables belong to the North Sea Link (Norway – United Kingdom) and Viking Link (Denmark – United Kingdom), with a power transmission length of 730 and 765 km, respectively.

Since 2015, MMC has become the favored converter technology in almost all offshore HVDC projects in the North Sea. This VSC technology has reached the DC voltage level of $\pm$ 525 kV, and ABB and Siemens are the two leading manufacturers worldwide that are realizing MMCs.

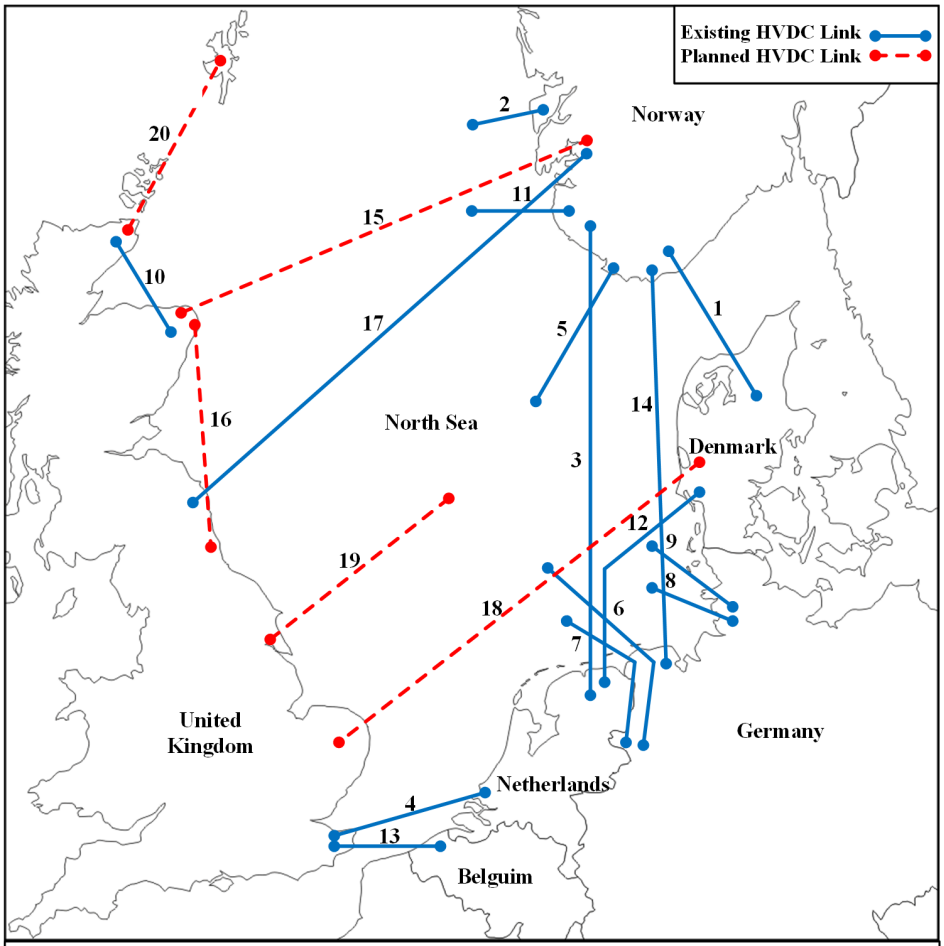

Figure 2.2: Existing and planned offshore HVDC grids in the North Sea.

Table 2.1: HVDC grids' characteristics in the North Sea.

No.	Name	Country	Commissioning year	Power (MW)	DC voltage (kV)	DC transmission length (km)	Converter type	Manufacturer
1	Skagerrak 1&2	Norway - Denmark	1976 - 77 (Upgrade: 2007)	500	250	113 (OHL) 127 (SMC)	HVDC Classic	ABB
	Skagerrak 3	Norway - Denmark	1993 (Upgrade: 2014)	440	350	113 (OHL) 127 (SMC)	HVDC Classic	ABB
	Skagerrak 4	Norway - Denmark	2014	700	500	104 (OHL) 140 (SMC)	HVDC Light (VSC MMC)	ABB
2	Troll A 1&2	Norway	2005	88	±60	4 × 70 (SMC)	HVDC Light (2-Level-VSC)	ABB
	Troll A 3&4	Norway	2015	100	±60	4 × 70 (SMC)	HVDC Light (2-Level-VSC)	ABB
3	NorNed	Norway - Netherlands	2008	700	±450	580 (SMC)	HVDC Classic	ABB
4	BritNed	UK - Netherlands	2011	1000	±450	18 (UGC) 494 (SMC)	LCC	ABB & Siemens
5	Valhall	Norway	2011	78	150	292 (SMC)	HVDC Light (2-Level-VSC)	ABB & Hitachi
6	BorWin1	Germany	2015	400	±150	2 × 125 (UGC) 2 × 75 (SMC)	HVDC Light (2-Level-VSC)	ABB & Hitachi
	BorWin2	Germany	2015	800	±300	2 × 75 (UGC) 2 × 120 (SMC)	HVDC PLUS (VSC MMC)	Siemens
	BorWin3	Germany	2019	900	±320	2 × 30 (UGC) 2 × 130 (SMC)	HVDC PLUS (VSC MMC)	Siemens
7	DolWin1	Germany	2015	800	±320	2 × 90 (UGC) 2 × 75 (SMC)	HVDC Light (VSC MMC)	ABB & Hitachi
	DolWin2	Germany	2017	916	±320	2 × 90 (UGC) 2 × 45 (SMC)	HVDC Light (VSC MMC)	ABB & Hitachi
	DolWin3	Germany	2019	900	±320	2 × 79 (UGC) 2 × 83 (SMC)	VSC MMC	GE
8	HelWin1	Germany	2015	576	±250	2 × 45 (UGC) 2 × 85 (SMC)	HVDC PLUS (VSC MMC)	Siemens
	HelWin2	Germany	2015	690	±320	2 × 46 (UGC) 2 × 85 (SMC)	HVDC PLUS (VSC MMC)	Siemens

9	SylWin1	Germany	2015	864	±320	2 × 45 (UGC) 2 × 160 (SMC)	HVDC PLUS (VSC MMC)	Siemens
10	Caithness - Moray	UK	2018	1200	±320	160	HVDC Light (VSC MMC)	ABB
11	Johan Sverdrup	Norway	2019	100	±80	2 × 200 (SMC)	HVDC Light	ABB
12	COBRA Cable	Denmark - Netherland	2019	700	±320	26 (UGC) 299 (SMC)	HVDC PLUS (VSC MMC)	Siemens
13	NEMO Link	Belgium - UK	2019	1000	±400	10 (UGC) 130 (SMC)	HVDC PLUS (VSC MMC)	Siemens
14	Nord Link	Norway - Germany	2020	1400	±525	53 (OHL) 2 × 54 (UGC) 2 × 516 (SMC)	HVDC Light (VSC MMC)	ABB & Hitachi
15	NorthConnect	Norway - UK	2022	1400	±525	665 (SMC)	N.A.	N.A.
16	Eastern Link	UK	2024	2000	400	305 (SMC)	N.A.	N.A.
17	North Sea Link (NSN)	Norway - UK	2021	1400	±525	730 (SMC)	HVDC Light (VSC MMC)	ABB & Hitachi
18	Viking Link	Denmark - UK	2023	1400	±525	765 (SMC)	HVDC PLUS (VSC MMC)	Siemens
19	Dogger Bank A	UK	2023	1200	±320	35 (UGC) 173 (SMC)	HVDC Light (VSC MMC)	ABB & Hitachi
	Dogger Bank B	UK	2024	1200	±320	35 (UGC) 173 (SMC)	HVDC Light (VSC MMC)	ABB & Hitachi
	Dogger Bank C	UK	2025	1200	±320	35 (UGC) 173 (SMC)	HVDC Light (VSC MMC)	ABB & Hitachi
20	Shetland HVDC Connection	UK	2024	600	±320	260 (SMC)	HVDC Light (VSC MMC)	ABB & Hitachi

UK: United Kingdom
OHL: Over Head Line
SMC: Submarine Cable
UGC: Underground Cable
N.A.: Not Available

2.3 Multiterminal HVDC grids

The interconnection between/within the point-to-point HVDC grids in the North Sea and large onshore electrical areas is considered critical in addressing the challenges concerning the growing energy demand and renewable-based power systems in Europe. By 2050, the electricity demand is anticipated to rise by two to three-fold, yet Europe aims to become climate-neutral. Wind energy is envisioned to supply about half of this demand [12] and can significantly contribute to the security of supply of the European energy network. Hence, the multiterminal offshore HVDC grids in the North Sea can play a prominent role in this regard.

2.3.1 HVDC grids' role in the future smart grid

The VSC-based HVDC technology has advanced significantly in recent years and has overcome numerous challenges concerning the converter technology, overhead line and submarine cable, DC switchgear, system configuration and grounding, control and stability, and protection [3], making it a sustainable solution for multiterminal configuration implementation in the future smart grid.

The characteristics that make the VSC-based HVDC grids a potential solution as the backbone of future power systems are [3]:

- Independent controllability of the active and reactive power
- High availability, reliability, and security by providing ancillary services
- High flexibility for interconnections between asynchronous zones
- High efficiency for offshore wind energy transmission over long distances
- Reasonable costs and losses for long-distance bulk energy transmission.

2.3.2 HVDC grids' topologies

The point-to-point HVDC connections in the North Sea are anticipated to interconnect and evolve into multiterminal configurations as a prerequisite for achieving a climate-neutral Europe by 2050. Namely, HVDC grids comprise the DC transmission within links and nodes on the DC-side of the grid. Three different HVDC grid topologies, consisting of radial, ring, and mesh, are illustrated in Fig. 2.3. The radial configuration is designed to look like a star with offshore converters in the centre. It is relatively simple to implement; however, its reliability is low compared with the other two topologies since the onshore converters are connected to the network through only one HVDC link. The ring configuration has slightly higher reliability, with two HVDC link connections per converter station, since

each node can be supplied even if one link fails. The grid's reliability can be considerably improved by realizing a mesh configuration, though this solution can be very costly due to the high number of required HVDC cables [44].

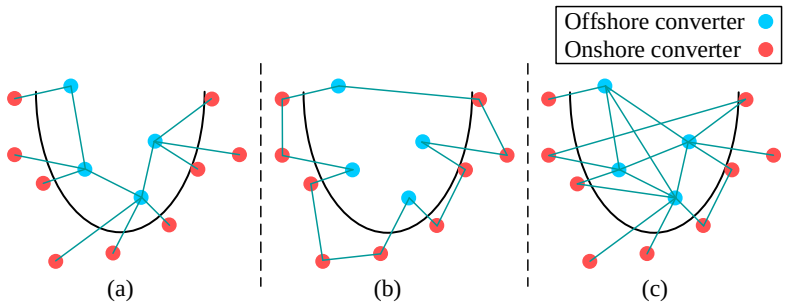

Figure 2.3: HVDC grid topologies: a) radial, b) ring, c) meshed.

2.4 Expansion challenges of the HVDC grids

The anticipated development and interconnection of the independently designed MMC-based offshore HVDC grids in the North Sea demands an appropriate TEP methodology to optimize the performance and minimize the costs of such an extensive complex infrastructure. Moreover, TEP problems are required to integrate techno-economical aspects to address the characteristics and issues specific to HVDC systems.

Despite the achievements obtained so far in the expansion of the HVDC grids, challenges and potential opportunities can be found in numerous areas, including technology development, control and stability, operation and protection, available software and tools, and non-technical issues:

- **Technology development:** The HVDC technology development is highly reliant on the grid equipment, including converters, lines and cables, and switchgears and Circuit Breakers (CBs). The focus is on achieving technologies with higher power capacities and voltage levels, smaller sizes and weights, and lower costs and losses. For instance, further standardization of the HVDC technology can considerably minimize investment costs, implementation time, and maintenance costs. Additionally, novel converter topologies can be attained by applying the latest power electronic switches and realizing hybrid VSCs with embedded thyristors. Moreover, improving the insulating materials to tolerate stronger electric fields can result in higher

voltage ratings at a constant diameter of the HVDC cables. Furthermore, superconducting technology, which can significantly reduce transmission losses and limit fault currents, may play an essential role in future HVDC grids' lines, cables, and CBs. And last but not least, HVDC Intelligent Electronic Devices (IEDs) can be applied for faster and more accurate communication among converter stations, measurement and protection devices, and switchgears [3, 12]:.

- **Control and stability:** Control interactions and stability issues are among the most significant challenges faced by the multiterminal HVDC grids. The interactions that may occur between or within AC and DC subgrids are identified by three categories: voltage control, electromechanical, and electromagnetic [45]. Namely, the most dominant system modes with the lowest damping ratios can be excited due to these interactions leading to disruptive and persistent oscillations throughout the whole network. Hence, MMC modeling simplifications, by ignoring the typical internal dynamics of this converter or substituting it with the conventional two-level VSC, can yield misleading and unreliable results. An optimal control strategy for multiterminal multi-vendor HVDC grids is required to assure grid stability by improving the stability margins and damping the oscillations and dynamic interactions caused by the dominant poles with the lowest damping ratios. The control methodology should be immune to long-distance communication delays and failures threatening the network's reliability and stability. Moreover, due to interoperability, renewables intermittency, and load variability, the control strategy should be robust enough to tolerate parametric uncertainties in control parameters, grid parameters, and operating conditions under disturbances on the AC- and DC-side of the grid [3, 9, 12].

- **Operation and protection:** Reliability and security of supply are essential elements in the operation of the multiterminal HVDC grids. The intermittent nature of renewable resources such as wind and uncertainties of load consumption profile can adversely impact the grid's reliability and security. Multiterminal HVDC grids can improve the real-time supply and demand balance and reduce the Renewable Energy Curtailment (REC) by transferring the surplus energy from the distributed and intermittent resources to the neighboring load centres. Moreover, incorporating Energy Storage Systems (ESSs) such as batteries into the hybrid AC/DC grids can significantly enhance reliability and security. In contrast, contingencies on the DC-side of the grid, such as outages and faults, can propagate into the entire network, deteriorating supply security. Hence, robust and fast protection algorithms, preferably not reliant on time-consuming long-distance communications,

should be developed to protect the multiterminal HVDC grids against all potential faults in any condition. Furthermore, VSC-based converters' control flexibility and ancillary services support can play an essential role in protection and fault clearing to assure grid stability and reliability [3, 9].

- **Available software and tools:** Available software and tools for hybrid AC/DC grids generally consider HVDC equipment such as MMCs as specific components and lack accurate and efficient HVDC technology models (detailed, averaged) and representations (steady-state, dynamic) as an integral part of the power systems. Hence, there is a demand for comprehensive development and implementation of the HVDC equipment into time-efficient modeling, control, and protection tools as well as optimal operational and expansion planning algorithms [3, 9].

- **Grid codes and standards:** Harmonized international grid codes and standards, which incorporate requirements on both the AC- and DC-side of the grid while addressing technical, economic, and environmental issues, are indispensable for the feasibility of the HVDC grids and eventually the corresponding expansion planning [9].

The work of this PhD contributes towards addressing the challenges of "control and stability" and "available software and tools".

2.5 Summary

This chapter presented the existing and planned point-to-point HVDC grids in the North Sea, as well as their technical specifications and converter manufacturers. It has been shown that MMC has become the dominant converter technology in the HVDC grids in the North Sea, with its DC voltage reaching up to ± 525 kV. Next, the HVDC technology's role in the future smart grid was investigated. It is anticipated that MMC-based HVDC grids can be a potential solution as the backbone of the future renewable power network considering their particular features and latest achievements. Finally, the expansion challenges of the HVDC grids were discussed. Dynamic interactions and stability issues are among the most significant challenges, which demand a decentralized, optimal, and robust control strategy to assure multiterminal HVDC grids' stability. Furthermore, the TEP problem formulation needs to be modified to reflect the HVDC grids' challenges and potential opportunities.

The discussion in this chapter was partially supported by the following contribution by the author:

A. Elahidoost and E. Tedeschi, "Expansion of offshore HVDC grids: An overview of contributions, status, challenges and perspectives," *2017 IEEE 58th International Scientific Conference on Power and Electrical Engineering of Riga Technical University (RTUCON)*, 2017, pp. 1-7, doi: 10.1109/ RTUCON.2017.8124767 [9].

Chapter 3

HVDC grid modeling and control

3.1 Introduction

In power system studies, various analyses and simulation methodologies are generally used based on the application, including steady-state analysis, small-signal stability analysis, Electromagnetic Transient (EMT) simulation, and Root Mean Square (RMS) or phasor simulation [46]. These modeling techniques contain a particular degree of trade-off between precision and tractability and can be defined according to the purpose of the analysis.

The steady-state analysis is a means to evaluate system operating conditions (operating point and power flow study) and typically requires a minimum amount of modeling details as system dynamics and transients are beyond the scope of this study. On the other hand, the small-signal stability analysis demands a higher degree of modeling accuracy since it is a tool to investigate power system stability under small disturbances (dynamics and transients) around the operating point obtained from the steady-state analysis.

In RMS or phasor simulations, voltage and current sinusoidal waveforms are written in the phasor form; i.e., system differential equations are turned into algebraic ones, leading to time-efficient simulations. This study type is basically developed for analyzing dynamics of the large power systems in the ms to s time-scale. In contrast, EMT simulations are applicable in analyzing phenomena in the ms to μs range; thus, while being accurate, they are very time-consuming and complicated to implement. Namely, all power system equations are represented in differential form with capacitive and inductive reactances corresponding to frequency variations in the time-domain. Hence, EMT simulations can be very sluggish due to

requiring detailed datasets and are typically limited to small-scale power systems.

The choice of the modeling and simulation methodology is dependent on the analysis purpose and is a compromise between accuracy and practicality. Hence, this chapter focuses on the modeling and control of the HVDC grids and presents the required theoretical basis and applied simulation methodology as a prerequisite for the remainder of the thesis.

3.2 modeling of the MMC

Modular multilevel converters, initially proposed for high-power, high-voltage applications [26], are currently the heart of any modern HVDC project. The most distinctive characteristic of these converters is the high quality of the produced voltage and current waveforms with low THD. This quality is achieved due to the converter's modular realization formed by series connections of submodules (SMs) with low-voltage components. Submodules, which are the converter's building blocks, can be of different structures based on their applications. The half-bridge commutation cell is the simplest submodule structure, and it can operate in two quadrants (uni-directional voltage and bi-directional current) and generate two voltage levels (0 and V_{sm}) [25]. Moreover, MMCs have high availability and reliability due to standard components and redundant operation and are fault-tolerant owing to fail-safe operation during component failures. Last but not least, MMCs have high efficiency and low losses and are scalable to various power and voltage ratings, allowing the converter to be the best alternative for HVDC applications [25, 26].

A three-phase MMC topology is depicted in Fig. 3.1. The converter structure is similar to the conventional two-level VSC but with a string of submodules in each phase, also called a leg. Each leg is divided into the upper and lower arms, denoted with the subscripts "*u*" and "*l*", respectively. Thus, every three-phase MMC comprises three legs and six arms, as shown in Fig. 3.1. The MMC AC terminals are taken from the midpoint of each leg, where there is an arm inductor, L_a, and an arm resistor, R_a. The arm inductor's task is to limit the arm current harmonics and fault currents, whereas the arm resistor is representative of the arm inductor's inner resistance and converter losses. The MMC DC terminals are located at the endpoints of the converter legs, and the energy storage elements that are the submodule capacitors, C_{sm}, are placed at each arm [47, 48].

As mentioned earlier, submodules are the building blocks of the MMCs. Various submodule topologies for specific applications have been introduced, including half-bridge, full-bridge, mixed, asymmetrical double, cross- or parallel-connected, clamped-double, Flying Capacitor (FC), and Neutral Point Clamped-type (NPC-

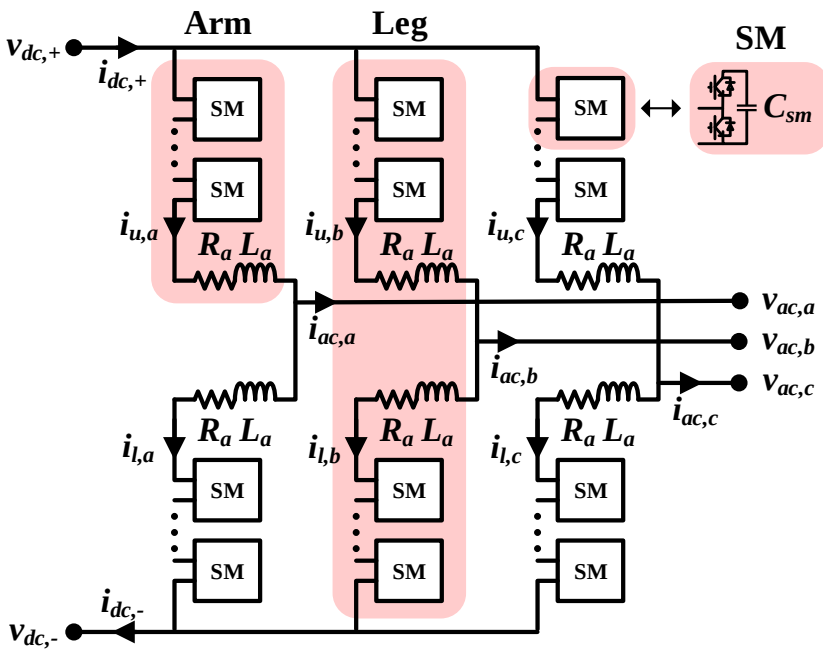

Figure 3.1: MMC topology.

type) commutation cells [25]. The simplest, most common and cost-efficient submodule topology, which consists of two switches (each switch is a combination of an IGBT and a freewheeling diode) and a capacitor bank, is the half-bridge commutation cell as shown in Fig. 3.2. The operation principle of the half-bridge submodule is as follows:

- Inserted: S_1 is on, and S_2 is off, the capacitor can be charged or discharged through the freewheeling diode or IGBT, respectively, and the submodule output voltage is V_{SM}.
- Bypassed: S_1 is off, and S_2 is on, the capacitor voltage remains constant, and the submodule output voltage is 0.

An appropriate modulation strategy is required to insert or bypass the desired number of the submodules at each cycle to form the MMC three-phase sinusoidal voltage and current waveforms. The higher the number of submodules in each

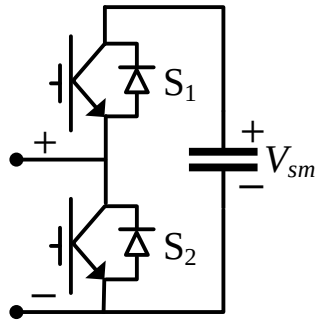

Figure 3.2: Submodule topology: half-bridge.

arm, the better the voltage and current waveforms quality. By assuming N to be the number of the submodules in each arm, the insertion indices for the upper and lower arms can be defined as:

$$n_u = \frac{v_u}{v_{cu}} = \frac{\sum_{i=1}^{N_{ins,u}} v_{smi,u}}{\sum_{i=1}^{N} v_{smi,u}} \quad n_l = \frac{v_l}{v_{cl}} = \frac{\sum_{i=1}^{N_{ins,l}} v_{smi,l}}{\sum_{i=1}^{N} v_{smi,l}} \tag{3.1}$$

where n_u and n_l are the upper and lower arm insertion indices, v_u and v_l are the upper and lower arm output voltages, v_{cu} and v_{cl} are the upper and lower arm capacitor voltages sum, $N_{ins,u}$ and $N_{ins,u}$ are the number of inserted upper and lower arm submodules, and $v_{smi,u}$ and $v_{smi,l}$ are the i^{th} upper and lower arm submodule capacitor voltages, respectively.

The upper and lower arm insertion indices in the above equations are assumed to be continuous variables instead of one of the $1 + N$ discrete variables between 0 and 1 with a step size of $1/N$. This assumption is made for the sake of converter modeling and control simplification and is only valid under the infinite switching frequency and the infinite number of submodules in each arm [46, 49].

The MMC upper (u) and lower (l) arm insertion indices (n), voltages (v), capacitor voltages sum (v_c), and currents (i) can be defined through the differential (Δ/ac) and common-mode (Σ/c) representation to simplify the converter modeling and

control:

$$n_\Delta = \frac{n_l - n_u}{2} \qquad n_\Sigma = \frac{n_u + n_l}{2} \tag{3.2}$$

$$v_{ac} = \frac{v_l - v_u}{2} \qquad v_c = \frac{v_u + v_l}{2} \tag{3.3}$$

$$v_\Delta = \frac{v_{cu} - v_{cl}}{2} \qquad v_\Sigma = \frac{v_{cu} + v_{cl}}{2} \tag{3.4}$$

$$i_{ac} = i_u - i_l \qquad i_c = \frac{i_u + i_l}{2} \tag{3.5}$$

where v_{ac} and i_{ac} are the AC-side voltage and current. The common-mode variable i_c is known as the circulating current and v_c is the voltage driving it.

The MMC differential/common-mode representation classifies the converter variables into two frequency groups: the differential variables, which are mainly associated with the frequency of ω and 3ω, and the common-mode variables, which mainly contain the DC and -2ω components. If the circulating current's second harmonic (-2ω) is suppressed via a modulation or control strategy, then the MMC differential and common-mode variables only correspond to the fundamental frequency of ω and DC-component, respectively [50]. It should be noted that the MMC internal dynamics are primarily affected by the arm capacitor voltages and circulating currents, which are specific to this converter and should not be overlooked in grid stability and expansion studies [18].

3.2.1 MMC average arm model (AAM)

MMCs are modeled in various forms with different application purposes [4, 7, 46, 48, 49, 50, 51, 52, 53, 54]. Simulation of the MMC with all the submodules in each arm is relevant in component-level dynamic studies in which the focus is on the converter's fast dynamics and transients arising from the switching action. On the other hand, in system-level dynamic analysis, the MMC's average arm model (AAM) is generally used, assuming infinite switching frequency, infinite number of submodules, and balanced submodule capacitor voltages in each arm. Hence, MMC arms can be represented as variable capacitances or voltage sources whose values correspond to the insertion indices that are assumed to be continuous variables [49].

Considering the MMC single-phase diagram shown in Fig. 3.3, the dynamics of the AAM of the MMC can be attained as follows:

AC grid current dynamics can be derived by applying Kirchhoff's Voltage Law

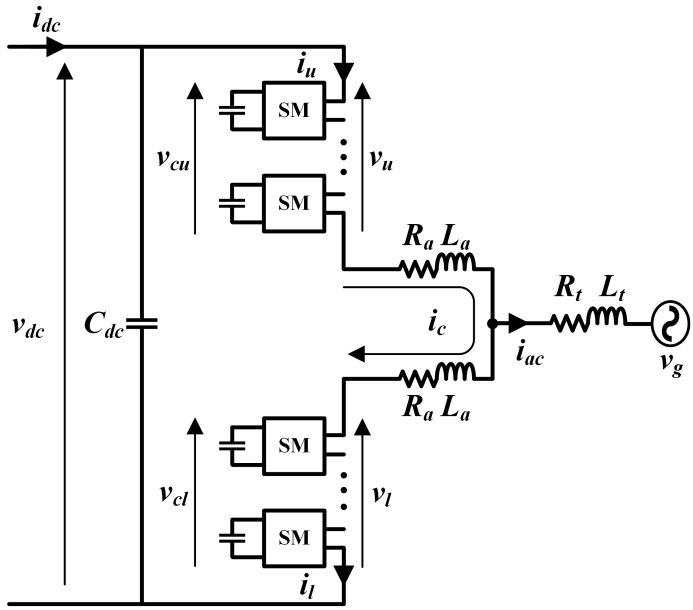

Figure 3.3: MMC single-phase diagram.

(KVL) on the AC-side of the converter:

$$\frac{d}{dt}i_{ac} = \frac{1}{L_{ac}}(v_{ac} - v_g - R_{ac}i_{ac}) \tag{3.6}$$

where v_g is the AC grid Thevenin equivalent voltage, $R_{ac} = R_t + R_a/2$, $L_{ac} = L_t + L_a/2$, R_t, and L_t are the transformer resistance and inductance, respectively.

By substituting (3.3) in (3.6), and using (3.1) and (3.2), (3.6) becomes:

$$\frac{d}{dt}i_{ac} = \frac{1}{L_{ac}}(n_\Delta v_\Sigma - n_\Sigma v_\Delta - v_g - R_{ac}i_{ac}) \tag{3.7}$$

Next, the dynamics of the circulating current can be obtained by applying the KVL on the DC-side of the converter:

$$\frac{d}{dt}i_c = \frac{1}{L_a}(\frac{v_{dc}}{2} - v_c - R_a i_c) \tag{3.8}$$

where v_{dc} is the voltage at DC terminals of the MMC.

Following the same procedure as for deriving (3.7), (3.8) can be written as:

$$\frac{d}{dt}i_c = \frac{1}{L_a}(\frac{v_{dc}}{2} + n_\Sigma v_\Sigma - n_\Delta v_\Delta - R_a i_c) \tag{3.9}$$

The dynamics of the arm capacitors can be defined through the submodule capacitor voltages in each arm. Thus, the upper arm voltage dynamics can be derived as follows:

$$\sum_{i=1}^{N} C_{smi} \frac{d}{dt} v_{smi,u} = N_{ins,u} i_u \tag{3.10}$$

$$C_{sm} \frac{d}{dt} N v_{sm,u} = N_{ins,u} i_u \tag{3.11}$$

$$C_{sm} \frac{d}{dt} v_{cu} = N_{ins,u} i_u \tag{3.12}$$

$$\frac{C_{sm}}{N} \frac{d}{dt} v_{cu} = \frac{N_{ins,u}}{N} i_u \tag{3.13}$$

$$C_a \frac{d}{dt} v_{cu} = n_u i_u \tag{3.14}$$

where C_a is the equivalent arm capacitance.

Similarly, the lower arm voltage dynamics can be written as:

$$C_a \frac{d}{dt} v_{cl} = n_l i_l \tag{3.15}$$

By adding and subtracting (3.14) and (3.15), and using (3.2), (3.4), and (3.5), the arm voltage dynamics can be reformulated as:

$$\frac{d}{dt} v_\Delta = \frac{1}{C_a} (\frac{1}{2} n_\Sigma i_{ac} - n_\Delta i_c) \tag{3.16}$$

$$\frac{d}{dt} v_\Sigma = \frac{1}{C_a} (n_\Sigma i_c - \frac{1}{2} n_\Delta i_{ac}) \tag{3.17}$$

Therefore, (3.7), (3.9), (3.16), and (3.17) are representative of the per-phase average arm model of the MMC. Hence, three sets of these equations are required to characterize the three-phase AAM of the MMC. Furthermore, this representation of the MMC average arm model is called voltage-based modeling due to the presence of the v_Δ and v_Σ state variables in the MMC arm dynamics. The insertion indices, n_Δ and n_Σ, appear explicitly in voltage-based modeling formulation [50]. The direct (uncompensated) modulation technique is generally applied to regulate the insertion indices to achieve the desired voltage level from the inserted arm capacitor voltages:

$$v_u = n_u v_{cu} = \frac{v_u^*}{v_{norm}} v_{cu} = v_u^* \frac{v_{cu}}{v_{dc}} \tag{3.18}$$

$$v_l = n_l v_{cl} \ = \frac{v_l^*}{v_{norm}} v_{cl} = v_l^* \frac{v_{cl}}{v_{dc}} \tag{3.19}$$

where $(.)^*$ denotes the reference value, and v_{norm} is a normalizing voltage such that the continuous upper and lower arm insertion indices vary within 0 and 1.

The v_{norm} in direct modulation is typically defined by the rated or measured value of the v_{dc}, and the insertion indices can simply be calculated by dividing the reference arm voltages by the DC voltage. The drawback of this modulation technique is that since the v_{dc} is a constant value, it cannot compensate for the second harmonics of the arm capacitor voltages and, consequently, circulating currents. These harmonics are transferred to the output arm voltages of the MMC as a result of the multiplication of the insertion indices to the arm capacitor voltages. Hence, a control strategy called Circulating Current Suppression Control (CCSC) is applied to dampen the effect of the second harmonics [55].

3.2.2 MMC energy-based model

The MMC energy-based model is another representation of the converter average arm model that can utilize the compensated modulation to suppress the second harmonic of the arm capacitor voltages and circulating currents [54]. Hence, the derivation of the MMC arm dynamics based on the energy-based modeling is given as follows:

Equations (3.14) and (3.15) are repeated here as the starting points:

$$C_a \frac{d}{dt} v_{cu} = n_u i_u \qquad C_a \frac{d}{dt} v_{cl} = n_l i_l \tag{3.20}$$

Both sides of the equations are multiplied by the corresponding arm capacitor voltages:

$$C_a v_{cu} \frac{d}{dt} v_{cu} = v_u i_u \qquad C_a v_{cl} \frac{d}{dt} v_{cl} = v_l i_l \tag{3.21}$$

On the other hand, the upper and lower arm capacitor energies, w_u and w_l, are defined as below:

$$w_u = \frac{1}{2} C_a v_{cu}^2 \qquad w_l = \frac{1}{2} C_a v_{cl}^2 \tag{3.22}$$

Then, the derivative of the arm capacitor energies with respect to the time is calculated.

$$\frac{d}{dt} w_u = C_a v_{cu} \frac{d}{dt} v_{cu} \qquad \frac{d}{dt} w_l = C_a v_{cl} \frac{d}{dt} v_{cl} \tag{3.23}$$

The resulting equations are compared with (3.21):

$$\frac{d}{dt} w_u = v_u i_u \qquad \frac{d}{dt} w_l = v_l i_l \tag{3.24}$$

The upper and lower arm voltages and currents are expanded using (3.3) and (3.5):

$$\frac{d}{dt}w_u = (v_c - v_{ac})(i_c + \frac{i_{ac}}{2}) \tag{3.25}$$

$$\frac{d}{dt}w_l = (v_c + v_{ac})(i_c - \frac{i_{ac}}{2}) \tag{3.26}$$

Finally, arm capacitor energy difference ($w_\Delta = w_u - w_l$) and sum ($w_\Sigma = w_u + w_l$) are developed as follows:

$$\frac{d}{dt}w_\Delta = v_c i_{ac} - 2v_{ac}i_c \tag{3.27}$$

$$\frac{d}{dt}w_\Sigma = 2v_c i_c - v_{ac}i_{ac} \tag{3.28}$$

Unlike (3.16) and (3.17), which are representative of the MMC arm dynamics in the voltage-based model, the insertion indices do not appear in the energy-based MMC arm dynamics. Namely, the inclusion of the insertion indices in (3.27) and (3.28) using (3.1) and (3.3) introduces complexity and nonlinearity in the model. Hence, compensated modulation is applied in the MMC energy-based modeling. In this modulation technique, v_{norm} is being replaced by the arm capacitor voltages (v_{cu} and v_{cl}) such that the arm voltages (v_u and v_l) become independent of the arm capacitor voltages as given in (3.29) and (3.30). Therefore, instead of the insertion indices, the reference arm voltages (v_u^* and v_l^*) are implemented as the inputs into the MMC arm dynamics. The primary advantage of compensated modulation in the ideal case is preventing the ripples in the arm capacitor voltages from propagating into the arm voltages. Hence, the circulating current can be controlled only to contain the DC-component, and there will be no need for the CCSC to mitigate the second harmonic component [46, 54].

$$v_u = v_u^* \frac{v_{cu}}{v_{norm}} = v_u^* \frac{v_{cu}}{v_{cu}} = v_u^* \tag{3.29}$$

$$v_l = v_l^* \frac{v_{cl}}{v_{norm}} = v_l^* \frac{v_{cl}}{v_{cl}} = v_l^* \tag{3.30}$$

Considering (3.3), it can be concluded that the voltages v_{ac} and v_c are also equal to their reference values. Therefore, the MMC energy-based model can be written

as follows:

$$\frac{d}{dt}i_{ac} = \frac{1}{L_{ac}}(v^*_{ac} - v_g - R_{ac}i_{ac}) \tag{3.31}$$

$$\frac{d}{dt}i_c = \frac{1}{L_a}(\frac{v_{dc}}{2} - v^*_c - R_a i_c) \tag{3.32}$$

$$\frac{d}{dt}w_\Delta = v^*_c i_{ac} - 2v^*_{ac} i_c \tag{3.33}$$

$$\frac{d}{dt}w_\Sigma = 2v^*_c i_c - v^*_{ac} i_{ac} \tag{3.34}$$

3.2.3 MMC energy-based phasor model

The energy-based model of the MMC presented in the previous section is Steady-State Time-Periodic (SSTP), which is only applicable to time-domain simulations. The Steady-State Time-Invariant (SSTI) representation of the MMC is required for linearization at equilibrium and small-signal eigenvalue stability analysis. The phasor-based modeling of the harmonic components can be utilized to facilitate acquiring the SSTI model from the SSTP model [46, 51], and it can be derived while considering the following assumptions for simplifications:

- i_{ac}, v^*_{ac}, v_g, and w_Δ only have a first harmonic component (i_{ac1}, v^*_{ac1}, v_{g1}, and $w_{\Delta 1}$)
- i_c, and v^*_c only have a DC component (i_{c0}, and v^*_{c0})
- w_Σ has both DC and second harmonic components ($w_{\Sigma 0}$+$w_{\Sigma 2}$).

In the above assumptions, two main simplifications have been made: First, the DC component (average) of the arm capacitor energy difference, $\vec{w}_{\Delta 0}$, is ignored with the assumption that the MMC arm voltages are balanced on average through the control actions. Second, the second harmonic of the circulating current and voltage, i_{c2}, and v^*_{c2}, are disregarded as a result of the compensated modulation, as discussed earlier [46, 54].

The phasor representation of the time-domain signals $x(t) = X\cos(k_x\omega t + \phi_x)$ and $y(t) = Y\cos(k_y\omega t + \phi_y)$ can be shown as $\vec{x} = Xe^{j\phi_x}$ and $\vec{y} = Ye^{j\phi_y}$, respectively. Accordingly, the product of the two signals is calculated as follows

[46]:

$$\begin{aligned} x(t)y(t) = \frac{1}{2}XY\Big[&\cos\big((k_x+k_y)\omega t + (\phi_x+\phi_y)\big) \\ &+\cos\big((k_x-k_y)\omega t + (\phi_x-\phi_y)\big)\Big] \\ =&\frac{1}{2}(\vec{x}\vec{y} + \vec{x}\vec{y}^{conj}) \end{aligned} \tag{3.35}$$

where $(.)^{conj}$ is the complex conjugate operator.

The derivative of the signal $x(t)$ with respect to time while considering the time rotation of the phasor is as below [46]:

$$\frac{d}{dt}x(t) = \frac{d}{dt}(\vec{x}e^{j\omega t})e^{-j\omega t} = \frac{d}{dt}\vec{x} + j\omega\vec{x} \tag{3.36}$$

Hence, the phasor representation of the MMC energy-based model can be written as follows:

$$\frac{d}{dt}\vec{i}_{ac1} = \frac{1}{L_{ac}}(\vec{v}^*_{ac1} - \vec{v}_{g1} - R_{ac}\vec{i}_{ac1} - j\omega L_{ac}\vec{i}_{ac1}) \tag{3.37}$$

$$\frac{d}{dt}i_{c0} = \frac{1}{L_a}(\frac{v_{dc}}{2} - v^*_{c0} - R_a i_{c0}) \tag{3.38}$$

$$\frac{d}{dt}\vec{w}_{\Delta 1} = v^*_{c0}\vec{i}_{ac1} - 2\vec{v}^*_{ac1}i_{c0} - j\omega\vec{w}_{\Delta 1} \tag{3.39}$$

$$\frac{d}{dt}w_{\Sigma 0} = 2v^*_{c0}i_{c0} - \frac{1}{2}Re\{\vec{v}^*_{ac}\vec{i}^{conj}_{ac}\} \tag{3.40}$$

$$\frac{d}{dt}\vec{w}_{\Sigma 2} = -\frac{1}{2}\vec{v}^*_{ac}\vec{i}_{ac} - j\omega\vec{w}_{\Sigma 2} \tag{3.41}$$

The MMC energy-based phasor model can further be simplified as follows by ignoring the dynamics associated with the first harmonic component of the arm capacitor energy difference, $\vec{w}_{\Delta 1}$, and the second harmonic component of the arm capacitor energy sum, $\vec{w}_{\Sigma 2}$ [54, 56, 57]. The resultant representation is the MMC simplified zero-sequence phasor model, which contains information regarding the power balance in the AC-side, DC-side, and internally stored energy of the MMC. This model is primarily applicable to large-scale power system stability studies and is applied throughout this thesis in many cases.

$$\frac{d}{dt}\vec{i}_{ac} = \frac{1}{L_{ac}}(\vec{v}^*_{ac} - \vec{v}_g - R_{ac}\vec{i}_{ac} - j\omega L_{ac}\vec{i}_{ac}) \tag{3.42}$$

$$\frac{d}{dt}i_{c0} = \frac{1}{L_a}(\frac{v_{dc}}{2} - v^*_{c0} - R_a i_{c0}) \tag{3.43}$$

$$\frac{d}{dt}w_{\Sigma 0} = 2v^*_{c0}i_{c0} - \frac{1}{2}Re\{\vec{v}^*_{ac}\vec{i}^{conj}_{ac}\} \tag{3.44}$$

3.2.4 MMC per-unit representation

In power system analysis, the per-unit system that normalizes the system parameters and variables is typically utilized in contrast with the physical units. Namely, the per-unit quantity is the ratio of the actual quantity to the base value of the quantity [58]. While some base values are usually chosen arbitrarily, the rest should be selected based on the fundamental relations between the system's parameters and variables. It is computationally more convenient to choose the base values in the system such that the primary per-unit quantities become equal to one at the rated condition. Furthermore, the per-unit quantities facilitate evaluation and comparison among several systems and components. The MMC per-unit base values used in this thesis are presented in Table 3.1.

Table 3.1: MMC per-unit base values.

MMC per-unit base values	
Parameter	Base value
Base apparent power	$S_b = S_{rated}$
AC-side base voltage	$V_b^{ac} = \sqrt{\frac{2}{3}} V_{rated}$
DC-side base voltage	$V_b^{dc} = 2V_b^{ac}$
AC-side base current	$I_b^{ac} = \frac{2}{3}\frac{S_b}{V_b^{ac}}$
DC-side base current	$I_b^{dc} = \frac{S_b}{V_b^{dc}} = \frac{3}{4} I_b^{ac}$
AC-side base impedance	$Z_b^{ac} = \frac{V_b^{ac}}{I_b^{ac}}$
DC-side base impedance	$Z_b^{dc} = \frac{V_b^{dc}}{I_b^{dc}}$
AC-side base inductance	$L_b^{ac} = Z_b^{ac}$
DC-side base inductance	$L_b^{dc} = Z_b^{dc}$
AC-side base capacitance	$C_b^{ac} = \frac{1}{Z_b^{ac}}$
DC-side base capacitance	$C_b^{dc} = \frac{1}{Z_b^{dc}}$
Base arm capacitor energy	$W_b = \frac{1}{2} C_a (V_b^{dc})^2$

Hence, in accordance with the base values given in Table 3.1 the per-unit repres-

entation of the MMC energy-based phasor model can be written as follows:

$$\frac{d}{dt}\vec{i}_{ac,pu} = \frac{1}{l_{ac}}(\vec{v}^{*}_{ac,pu} - \vec{v}_{g,pu} - r_{ac}\vec{i}_{ac,pu} - j\omega l_{ac}\vec{i}_{ac,pu}) \tag{3.45}$$

$$\frac{d}{dt}i_{c0,pu} = \frac{1}{l_a}(\frac{v_{dc,pu}}{2} - v^{*}_{c0,pu} - r_a i_{c0,pu}) \tag{3.46}$$

$$\frac{d}{dt}w_{\Sigma 0,pu} = \frac{2}{c_a}(2v^{*}_{c0,pu}i_{c0,pu} - \frac{1}{3}Re\{\vec{v}^{*}_{ac,pu}\vec{i}^{conj}_{ac,pu}\}) \tag{3.47}$$

where $(.)_{pu}$ is the notation to show the per-unit values. The parameters r_{ac} and l_{ac} are the per-unit equivalent AC resistance and inductance, r_a and l_a are the per-unit arm resistance and inductance, and c_a is the per-unit equivalent arm capacitance. In this thesis, the arm resistance and inductance are chosen to be per-unitized with respect to the DC-side base values.

3.3 modeling of the HVDC cable

Cables can generally be modeled based on either lumped or distributed parameters, i.e., resistance, inductance, and capacitance. The conventional pi-model of the cable is an example of cable modeling with lumped parameters. However, cable lumped parameter representation overlooks the frequency dependency of the parameters. On the other hand, the VSC-HVDC grids, compared with the traditional large-scale power systems, are dominated by faster control loops and system dynamics, and transients [59, 60]. Hence, the HVDC cable representation should be improved to be accurate enough to account for the frequency dependency (low, intermediate, and high-frequency oscillations) and appropriate for dynamic and interaction analysis between/within AC and DC subgrids.

An example of such an accurate cable representation is the Universal Line Model (ULM), developed based on numerical implementations and tailored for EMT analysis and time-domain simulations [61]. The model is generally accepted as a reference to benchmark the performance of the other cable representations. However, it is not straightforward to convert the ULM into the state-space representation for eventual linearization and small-signal eigenvalue stability analysis. To this end, the single or cascaded pi-equivalent cable model is utilized. The results presented in [59, 60] show that the pi-equivalent representation is slightly conservative and can lead to invalid stability assessments. That is, wrongly predicted oscillatory modes that are poorly damped might appear while analyzing the system stability using the cable's conventional (cascaded) pi-model. Increasing the number of pi-sections in the cable model does not improve the accuracy of the results. It is also evident that ignoring the inductance and, accordingly, the current dynamics from the cable model, can at least avoid the false prediction of the oscillatory modes at

intermediate and high frequencies and represent a reasonably precise cable model at slower dynamics.

A frequency-dependent cable model with cascaded pi-sections and parallel series RL-branches is proposed in [59], which is suitable for state-space representation and small-signal eigenvalue stability analysis. The series impedance elements of the cable can be found through vector fitting [62]. It is demonstrated that the cable model is accurate enough both in frequency- and time-domains. Furthermore, it is more relevant to have a model with parallel series RL-branches than cascaded pi-sections. To this end, the HVDC cable model used in this thesis comprises one pi-section and three parallel series RL-branches (as shown in Fig. 3.4 with its parameters given in Table 3.2) to account for the frequency dependency and model simplicity simultaneously.

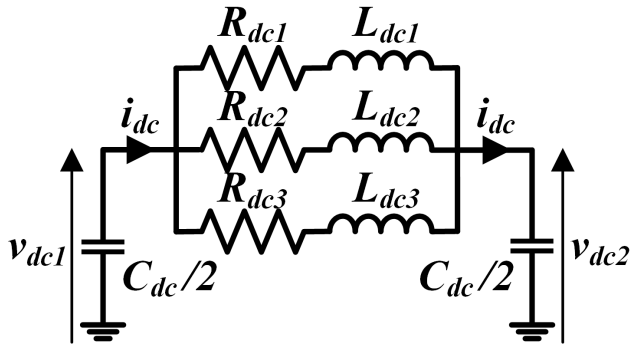

Figure 3.4: HVDC cable model with one pi-section and three parallel series RL-branches.

Table 3.2: HVDC cable parameters.

HVDC cable			
Parameter	Value	Parameter	Value
R_{dc1}	2.65 Ω/km	L_{dc1}	0.6016 mH/km
R_{dc2}	0.1218 Ω/km	L_{dc2}	0.302 mH/km
R_{dc3}	0.016 Ω/km	L_{dc3}	2.8 mH/km
C_{dc}	0.16 μF/km		

The dynamics of the HVDC cable, suitable for the state-space representation, can

be written as follows:

$$\frac{d}{dt}i_{dck} = \frac{1}{L_{dck}}(v_{dc1} - v_{dc2} - R_{dck}i_{dck}) \quad k = 1, 2, 3 \tag{3.48}$$

$$\frac{d}{dt}v_{dcj} = \frac{2}{C_{dc}}i_{dc} \quad j = 1, 2 \tag{3.49}$$

where i_{dck} is the DC current of each cable branch with $k = 1, 2, 3$, and v_{dcj} is the DC voltage on each side of the cable pi-section with $j = 1, 2$.

Thanks to the choice of the base values given in Table 3.1, the equations' structure can remain unchanged after per-unit conversion:

$$\frac{d}{dt}i_{dck,pu} = \frac{1}{l_{dck}}(v_{dc1,pu} - v_{dc2,pu} - r_{dck}i_{dck,pu}) \quad k = 1, 2, 3 \tag{3.50}$$

$$\frac{d}{dt}v_{dcj,pu} = \frac{2}{c_{dc}}i_{dc,pu} \quad j = 1, 2 \tag{3.51}$$

where r_{dc}, l_{dc}, and c_{dc} are the per-unit cable resistance, inductance, and capacitance, respectively.

3.4 MMC control hierarchy

MMC control in HVDC applications can be categorized into high-, mid-, and low-level control [46, 63], and accordingly, the converter control hierarchy used in this thesis can be shown as in Fig. 3.5.

The high-level control is almost independent of the converter topology. It is mainly associated with controlling the converter terminal characteristics that interact with the rest of the grid, including the active power, reactive power, and DC-side voltage controllers, as well as the Phase-Locked Loop (PLL). On the other hand, the low-level control is specific to the converter structure and is concerned with balancing the submodule capacitor voltages, Pulse Width Modulation (PWM), and submodule switching. It should be noted that the low-level control is not considered in this thesis and is out of the scope of work since the average model of the converter is being used with the assumption of ideal low-level control. The mid-level control, which is specific to MMC topology, has high interaction with the high-level and low-level controllers. The mid-level controllers are zero-sequence energy sum and circulating current controls together with the modulation to obtain the arm insertion indices.

3.5 High-level control

The high-level control comprises inner-loop AC-side current control, PLL, outer-loop active power control with DC voltage droop gain, and reactive power control.

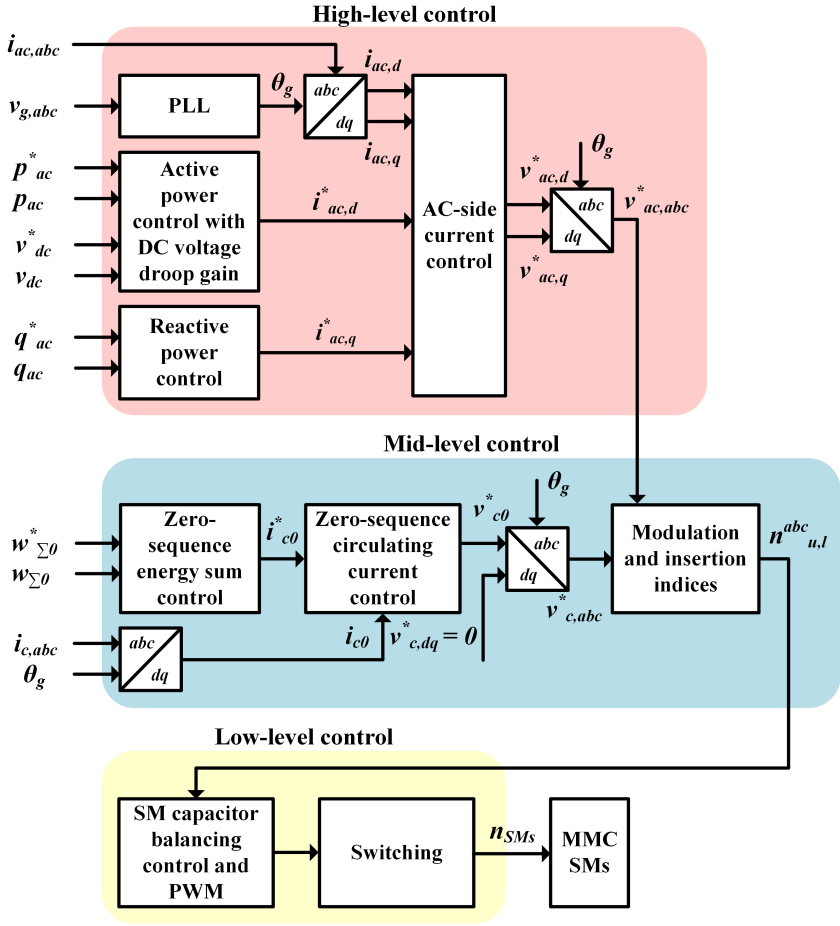

Figure 3.5: MMC control hierarchy.

The inner-loop AC-side current control is based on the vector control or synchronously rotating dq-reference frame. This control methodology regulates the direct (d) and quadrature (q) components of the AC-side current that are synchronously rotating at the reference frame with the angle θ_g, which is the angle of voltage ($v_{g,abc}$) at the Point of Common-Coupling (PCC) and is obtained via the PLL. The reference values of the dq-components of the AC-side current ($i^*_{ac,d}$ and $i^*_{ac,q}$) are the products of the outer-loop active power control with DC voltage droop gain and reactive power control, where the references to these outer-loop controllers (p^*_{ac}, q^*_{ac} and v^*_{dc}) are defined by the grid operators according to the grid codes, industry agreements, and economic considerations [63].

3.5.1 Phase-locked loop (PLL)

As mentioned above, the primary role of the PLL is to track θ_g, that is, the voltage angle at the PCC, which is then used to establish the synchronously rotating *dq*-reference frame of the converter. The PLL topology implemented in this thesis is adapted from [64, 65], and its operation principle and block diagram are depicted in Fig. 3.6 and 3.7, respectively. The global reference frame is arbitrarily selected as the synchronously rotating *dq*-reference frame of one of the system's generators referred to as a reference machine. Accordingly, the control objective is to reduce $\Delta\Theta_{pll}$ such that v_{gq} equals zero; therefore, $v_{pcc} = v_g = v_{g,d}$ and $\Theta_{pll} = \Theta_{pcc} = \Theta_g$. The PI controller that keeps $v_{gq} = 0$ can be tuned through the symmetric optimum technique [66]. The Low-Pass Filter (LPF) with T_f time constant is applied to block the high-frequency noise and disturbances from entering the PI controller and can also represent the sampling delay. The transfer function of the LPF can be ignored when deriving the PLL first-order differential equations due to the negligible value of T_f [64].

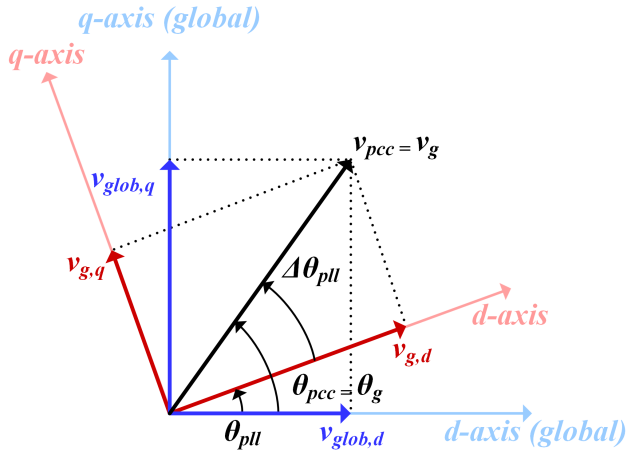

Figure 3.6: PLL operation principle.

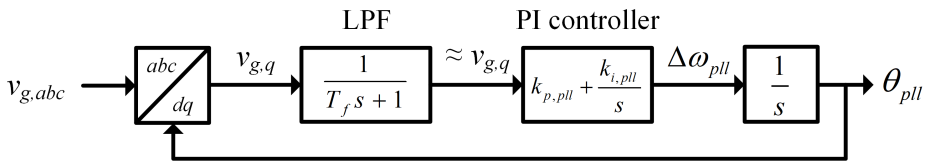

Figure 3.7: PLL block diagram.

Hence, the first-order differential equations of the PLL control loop can be written

as follows:

$$\frac{d}{dt}\Theta_{pll} = \Delta\omega_{pll} = k_{p,pll}v_{g,q} + k_{i,pll}\xi_{pll} \tag{3.52}$$

$$\frac{d}{dt}\xi_{pll} = v_{g,q} = v_g \sin\left(\Delta\Theta_{pll}\right) = v_g \sin\left(\Theta_g - \Theta_{pll}\right) \tag{3.53}$$

where Θ_{pll} and ω_{pll} are the PLL angle and angular frequency/velocity, respectively, and $k_{p,pll}$ and $k_{i,pll}$ are the PLL PI controller proportional and integral gains. The variable ξ_{pll} is related to the PI controller's integral state. It is worth mentioning that the control equations are written in per-unit representation, and the $(.)_{pu}$ index of the variables is omitted for the sake of simplification.

3.5.2 Inner-loop AC-side current control

Inner-loop AC-side current control with converter dynamics block diagram in synchronously rotating *dq*-reference frame is shown in Fig. 3.8. The AC-side current references ($i^*_{ac,dq}$), which are the inputs of the control loop, are the outputs of the outer-loop active and reactive power controls, as can be seen in Fig. 3.5. The other control loop inputs are produced as a result of measuring the generator voltages ($v_{g,dq}$) and AC-side currents ($i_{ac,dq}$).

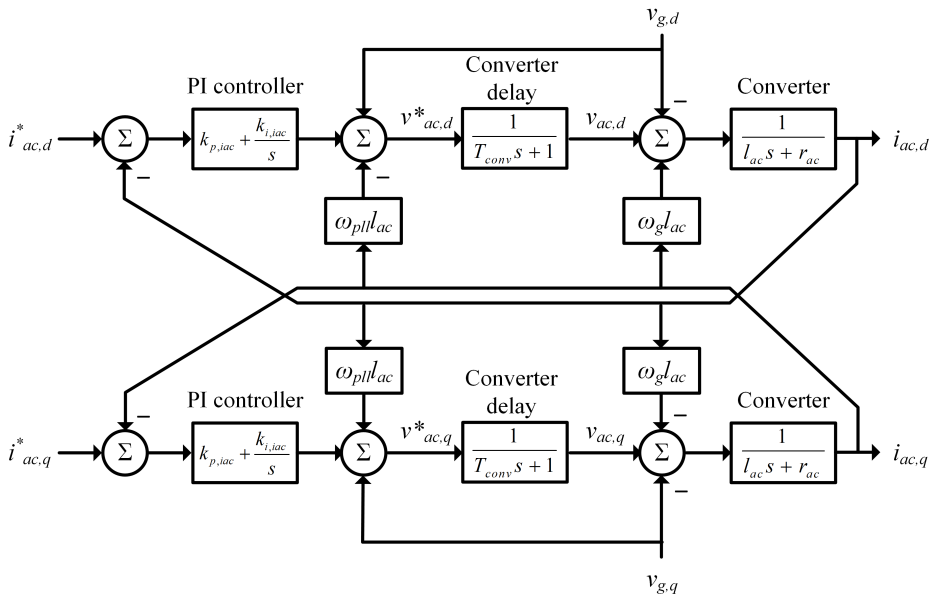

Figure 3.8: AC-side current control with converter dynamics block diagram in synchronously rotating *dq*-reference frame.

The PI controller that removes the error between the AC-side current references and measured values can be tuned via the modulus optimum methodology (refer to Appendix A) [66]. The converter delay block diagram with T_{conv} time constant represents the latency caused by the PWM and communications, and it can be ignored when deriving the first-order differential equations due to the negligible value of T_{conv}. The AC-side current dynamic equations, which are given in phasor representation in (3.45), can be converted into synchronously rotating *dq*-reference frame in per-unit as follows:

$$\frac{d}{dt}i_{ac,d} = \frac{1}{l_{ac}}(v^*_{ac,d} - v_{g,d} - r_{ac}i_{ac,d} + \omega_g l_{ac} i_{ac,q}) \tag{3.54}$$

$$\frac{d}{dt}i_{ac,q} = \frac{1}{l_{ac}}(v^*_{ac,q} - v_{g,q} - r_{ac}i_{ac,q} - \omega_g l_{ac} i_{ac,d}) \tag{3.55}$$

where $x_d = \Re\{\vec{x}\}$ and $x_q = \Im\{\vec{x}\}$. It should be noted that the cross-coupling terms in the above equations can be eliminated by applying the decoupling terms, $\pm\omega_{pll} l_{ac} i_{ac,dq}$, into the AC-side current control loops.

The other Differential and Algebraic Equations (DAE) describing the AC-side current control dynamics in per-unit can be written as:

$$v^*_{ac,d} = k_{p,iac}(i^*_{ac,d} - i_{ac,d}) + k_{i,iac}\xi_{iacd} + v_{g,d} - \omega_{pll} l_{ac} i_{ac,q} \tag{3.56}$$

$$v^*_{ac,q} = k_{p,iac}(i^*_{ac,q} - i_{ac,q}) + k_{i,iac}\xi_{iacq} + v_{g,q} + \omega_{pll} l_{ac} i_{ac,d} \tag{3.57}$$

$$\frac{d}{dt}\xi_{iacd} = (i^*_{ac,d} - i_{ac,d}) \tag{3.58}$$

$$\frac{d}{dt}\xi_{iacq} = (i^*_{ac,q} - i_{ac,q}) \tag{3.59}$$

where $k_{p,iac}$ and $k_{i,iac}$ are the AC-side current PI controller proportional and integral gains. The variables ξ_{iacd} and ξ_{iacq} are related to the PI controller's integral state.

3.5.3 Outer-loop control

The outer-loop comprises the active power control with DC voltage droop gain and reactive power control, which receives the p^*_{ac}, v^*_{dc}, and q^*_{ac} from the grid operators and generates the $i^*_{ac,d}$ and $i^*_{ac,q}$ to be sent to the inner-loop control. The equations for calculating the active and reactive powers are given as follows:

$$p_{ac} = v_{g,d} i_{ac,d} + v_{g,q} i_{ac,q} = v_{g,d} i_{ac,d} \tag{3.60}$$

$$q_{ac} = v_{g,q} i_{ac,d} - v_{g,d} i_{ac,q} = -v_{g,d} i_{ac,q} \tag{3.61}$$

Since the PLL regulates the $v_{g,q}$ to be zero, the active and reactive powers can be controlled separately by regulating the $i_{ac,d}$ and $i_{ac,q}$, respectively. The outer-loop control block diagram is shown in Fig. 3.9, and the symmetrical optimum

methodology can be implemented for tuning the PI controllers (refer to Appendix A) [66]. The DC voltage and active power control are closely coupled. Hence, if the DC voltage droop gain, ρ, is set to infinity, the control loop is on p_{ac} mode control; otherwise, it is on $p_{ac} - v_{dc}$ droop mode control.

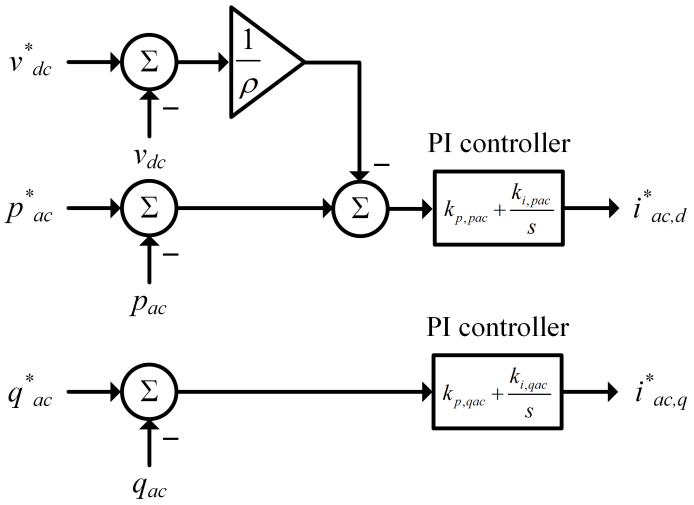

Figure 3.9: Outer-loop active power control with DC voltage droop gain and reactive power control block diagram.

Accordingly, the outer-loop control DAE in per-unit can be written as follows:

$$i^*_{ac,d} = k_{p,pac}\big(p^*_{ac} - v_{g,d}i_{ac,d} - \frac{1}{\rho}(v^*_{dc} - v_{dc})\big) + k_{i,pac}\xi_{pac} \tag{3.62}$$

$$i^*_{ac,q} = k_{p,qac}\big(q^*_{ac} - (-v_{g,d}i_{ac,q})\big) + k_{i,qac}\xi_{qac} \tag{3.63}$$

$$\frac{d}{dt}\xi_{pac} = \big(p^*_{ac} - v_{g,d}i_{ac,d} - \frac{1}{\rho}(v^*_{dc} - v_{dc})\big) \tag{3.64}$$

$$\frac{d}{dt}\xi_{qac} = \big(q^*_{ac} - (-v_{g,d}i_{ac,q})\big) \tag{3.65}$$

3.6 Mid-level control

The mid-level control is specific to MMCs and comprises the modulation and zero-sequence circulating current and energy sum controls, as shown in Fig. 3.5. The primary task of this control level is to ensure the power balance between the AC- and DC-sides of the converter. As mentioned earlier, the compensated modulation this thesis adopts compensates for the second harmonic component of the circulating current. Hence, the mid-level control only concerns regulating the zero-

sequence component of the circulating current and energy sum as explained in the following section.

3.6.1 Arm energy control

The arm energy can be controlled using the cascaded arrangement with the inner-loop zero-sequence circulating current control and outer-loop zero-sequence energy sum control, as shown in Fig. 3.10. The cascaded controller is derived based on (3.46) and (3.47). Accordingly, the inner and outer-loops manipulate the v^*_{c0} and i^*_{c0} to control the i_{c0} and $\omega_{\Sigma 0}$, respectively. It should be noted that the DC term, v_{dc}, from (3.46) and the AC term, $\vec{v}^*_{ac}\vec{i}^{conj}_{ac}$, from (3.47) are considered as external disturbances that should be rejected by the controller.

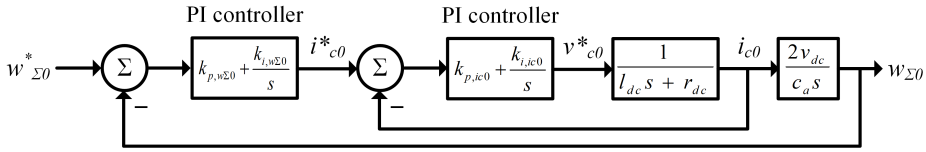

Figure 3.10: Cascaded arm energy control block diagram.

Finally, the cascaded arm energy control DAE in per-unit can be written as follows:

$$v^*_{c0} = k_{p,ic0}(i^*_{c0} - i_{c0}) + k_{i,ic0}\xi_{ic0} \tag{3.66}$$

$$i^*_{c0} = k_{p,\omega\Sigma 0}(\omega^*_{\Sigma 0} - \omega_{\Sigma 0}) + k_{i,\omega\Sigma 0}\xi_{\omega\Sigma 0} \tag{3.67}$$

$$\frac{d}{dt}\xi_{ic0} = (i^*_{c0} - i_{c0}) \tag{3.68}$$

$$\frac{d}{dt}\xi_{\omega\Sigma 0} = (\omega^*_{\Sigma 0} - \omega_{\Sigma 0}) \tag{3.69}$$

3.7 Small-signal eigenvalue analysis

Small-signal eigenvalue analysis is a methodology to investigate the stability of the power system when it is linearized around the equilibrium/operating point and is subject to small disturbances/perturbations [58]. This local/small-signal stability technique provides valuable information about the system's inherent dynamics and interactions that can be used to tune controllers to ensure the stable and proper performance of the system. In addition, the linearized system characteristics obtained from the eigenvalues/modes in the complex s-plane can be highly insightful and be a basis for evaluating the global/large-signal stability of the non-linear hybrid AC/DC grids in time-domain simulations [67]. This section briefly reviews the small-signal eigenvalue stability analysis terms, and theory [58, 68, 69, 70, 71], which are frequently used in the following chapters.

3.7.1 State-space representation

The dynamic behavior of the autonomous power system can be explained through the state-space representation [58]:

$$\begin{aligned}\dot{\mathbf{x}} &= f(\mathbf{x}, \mathbf{u}) \\ \mathbf{z} &= g(\mathbf{x}, \mathbf{u}) \\ \mathbf{x} &= \begin{bmatrix} x_1 & x_2 & \dots & x_n \end{bmatrix}^T \\ \mathbf{u} &= \begin{bmatrix} u_1 & u_2 & \dots & u_m \end{bmatrix}^T\end{aligned} \tag{3.70}$$

where $\mathbf{x}$, $\mathbf{u}$, and $\mathbf{z}$ are the state, control input, and output vectors, respectively. The derivative of $\mathbf{x}$ with respect to time is written as $\dot{\mathbf{x}}$, and if $\dot{\mathbf{x}}$ is not an explicit function of time, then the system is said to be autonomous [58]. State variables of the state vector are the minimum number of linearly independent variables that, together with the control inputs, can describe the system's dynamic behavior.

3.7.2 Linearization

As mentioned earlier, the power system can be linearized around the equilibrium/operating point where all the state variables are constant and unvarying with time [58]. Hence, the equilibrium point should satisfy the following equation:

$$\dot{\mathbf{x}}_\mathbf{0} = f(\mathbf{x}_\mathbf{0}, \mathbf{u}_\mathbf{0}) = 0 \tag{3.71}$$

where $\mathbf{x_0}$, and $\mathbf{u_0}$ are the initial state and control input vectors corresponding to the equilibrium point.

If the system is subject to perturbation from its equilibrium point, then the new state vector can be written as:

$$\dot{\mathbf{x}} = \dot{\mathbf{x}}_\mathbf{0} + \boldsymbol{\Delta}\dot{\mathbf{x}} = f[(\mathbf{x}_\mathbf{0} + \boldsymbol{\Delta}\mathbf{x}), (\mathbf{u}_\mathbf{0} + \boldsymbol{\Delta}\mathbf{u})] \tag{3.72}$$

where prefix $\boldsymbol{\Delta}$ defines small variation.

The equation can further be expanded through Taylor's series for every state variable x_i while neglecting the second and higher order power terms:

$$\begin{aligned}\dot{x}_i = \dot{x}_{i0} + \Delta\dot{x}_i &= f_i[(\mathbf{x}_\mathbf{0} + \boldsymbol{\Delta}\mathbf{x}), (\mathbf{u}_\mathbf{0} + \boldsymbol{\Delta}\mathbf{u})] \\ &= f_i(\mathbf{x}_\mathbf{0}, \mathbf{u}_\mathbf{0}) + \frac{\partial f_i}{\partial x_1}\Delta x_1 + \dots + \frac{\partial f_i}{\partial x_n}\Delta x_n + \frac{\partial f_i}{\partial u_1}\Delta u_1 + \dots + \frac{\partial f_i}{\partial u_m}\Delta u_m\end{aligned} \tag{3.73}$$

Since $\dot{x}_{i0} = f_i(\mathbf{x}_\mathbf{0}, \mathbf{u}_\mathbf{0})$, and similarly $z_{j0} = g_j(\mathbf{x}_\mathbf{0}, \mathbf{u}_\mathbf{0})$; hence, the linearized form of (3.70) can be written as:

$$\begin{aligned}\boldsymbol{\Delta}\dot{\mathbf{x}} &= \mathbf{A}\boldsymbol{\Delta}\mathbf{x} + \mathbf{B}\boldsymbol{\Delta}\mathbf{u} \\ \boldsymbol{\Delta}\mathbf{z} &= \mathbf{C}\boldsymbol{\Delta}\mathbf{x} + \mathbf{D}\boldsymbol{\Delta}\mathbf{u}\end{aligned} \tag{3.74}$$

$$\mathbf{A} = \begin{bmatrix} \frac{\partial f_1}{\partial x_1} & \cdots & \frac{\partial f_1}{\partial x_n} \\ \cdots & \cdots & \cdots \\ \frac{\partial f_n}{\partial x_1} & \cdots & \frac{\partial f_n}{\partial x_n} \end{bmatrix}_{n\times n} \qquad \mathbf{B} = \begin{bmatrix} \frac{\partial f_1}{\partial u_1} & \cdots & \frac{\partial f_1}{\partial u_m} \\ \cdots & \cdots & \cdots \\ \frac{\partial f_n}{\partial u_1} & \cdots & \frac{\partial f_n}{\partial u_m} \end{bmatrix}_{n\times m}$$

$$\mathbf{C} = \begin{bmatrix} \frac{\partial g_1}{\partial x_1} & \cdots & \frac{\partial g_1}{\partial x_n} \\ \cdots & \cdots & \cdots \\ \frac{\partial g_r}{\partial x_1} & \cdots & \frac{\partial g_r}{\partial x_n} \end{bmatrix}_{r\times n} \qquad \mathbf{D} = \begin{bmatrix} \frac{\partial g_1}{\partial u_1} & \cdots & \frac{\partial g_1}{\partial u_m} \\ \cdots & \cdots & \cdots \\ \frac{\partial g_r}{\partial u_1} & \cdots & \frac{\partial g_r}{\partial u_m} \end{bmatrix}_{r\times m}$$

where matrices $\mathbf{A}$, $\mathbf{B}$, $\mathbf{C}$, and $\mathbf{D}$ are the state, control input, output, and feedforward matrices, respectively. The partial derivatives of the above matrices should be calculated around the equilibrium point.

The Laplace transform can be used to obtain the above state equations in the frequency domain as follows:

$$\begin{aligned} \mathbf{s}\boldsymbol{\Delta}\mathbf{x}(\mathbf{s}) - \boldsymbol{\Delta}\mathbf{x}(\mathbf{0}) &= \mathbf{A}\boldsymbol{\Delta}\mathbf{x}(\mathbf{s}) + \mathbf{B}\boldsymbol{\Delta}\mathbf{u}(\mathbf{s}) \\ \boldsymbol{\Delta}\mathbf{z}(\mathbf{s}) &= \mathbf{C}\boldsymbol{\Delta}\mathbf{x}(\mathbf{s}) + \mathbf{D}\boldsymbol{\Delta}\mathbf{u}(\mathbf{s}) \end{aligned} \tag{3.75}$$

By rearranging (3.75), the state and output vectors' Laplace transforms can be written as:

$$\begin{aligned} \boldsymbol{\Delta}\mathbf{x}(\mathbf{s}) &= \frac{\mathbf{adj}(\mathbf{sI} - \mathbf{A})}{\mathbf{det}(\mathbf{sI} - \mathbf{A})}(\boldsymbol{\Delta}\mathbf{x}(\mathbf{0}) + \mathbf{B}\boldsymbol{\Delta}\mathbf{u}(\mathbf{s})) \\ \boldsymbol{\Delta}\mathbf{z}(\mathbf{s}) &= \mathbf{C}\frac{\mathbf{adj}(\mathbf{sI} - \mathbf{A})}{\mathbf{det}(\mathbf{sI} - \mathbf{A})}(\boldsymbol{\Delta}\mathbf{x}(\mathbf{0}) + \mathbf{B}\boldsymbol{\Delta}\mathbf{u}(\mathbf{s})) + \mathbf{D}\boldsymbol{\Delta}\mathbf{u}(\mathbf{s}) \end{aligned} \tag{3.76}$$

Then, the poles/roots of the above equations can be obtained as follows:

$$\mathbf{det}(\mathbf{sI} - \mathbf{A}) = 0 \tag{3.77}$$

where (3.77) is represented as the characteristic equation of the matrix $\mathbf{A}$, and the solutions in the unknown "$\mathbf{s}$" are called the eigenvalues/modes, λ, of the matrix $\mathbf{A}$.

According to Lyapunov's first method, a nonlinear system is asymptotically stable and returns to its equilibrium point after small perturbations if all the eigenvalues have negative real parts. Indeed, eigenvalues can be real or complex. Negative real eigenvalues correspond to decaying non-oscillatory modes, whereas the complex eigenvalues are in conjugate pairs, and each pair with negative real components corresponds to a damped oscillatory mode. Hence, a complex eigenvalue pair can be represented as:

$$\lambda = \sigma \pm j\omega \tag{3.78}$$

where the real component gives the damping and the imaginary component gives the oscillation frequency in Hz ($f = \frac{\omega}{2\pi}$). Accordingly, the damping ratio is defined as:

$$\zeta = \frac{-\sigma}{\sqrt{\sigma^2 + \omega^2}} \tag{3.79}$$

3.7.3 Eigenvalues and eigenvectors

For any eigenvalue, λ_i, there exists an n-column vector $\mathbf{\Phi_i}$ that satisfies [58]:

$$\begin{aligned} \mathbf{A\Phi_i} &= \lambda_i \mathbf{\Phi_i} \quad i = 1, ..., n \\ \mathbf{\Phi_i} &= \begin{bmatrix} \phi_{1i} \\ \vdots \\ \phi_{ni} \end{bmatrix} \end{aligned} \tag{3.80}$$

where $\mathbf{\Phi_i}$ is called the right eigenvector of the matrix $\mathbf{A}$ associated with the eigenvalue λ_i.

Similarly, the left eigenvector of the matrix $\mathbf{A}$ associated with the eigenvalue λ_i can be defined via an n-row vector $\mathbf{\Psi_i}$ such that:

$$\begin{aligned} \mathbf{\Psi_i A} &= \lambda_i \mathbf{\Psi_i} \quad i = 1, ..., n \\ \mathbf{\Psi_i} &= \begin{bmatrix} \psi_{1i} & ... & \psi_{ni} \end{bmatrix} \end{aligned} \tag{3.81}$$

It is worth mentioning that the left and right eigenvectors corresponding to different eigenvalues are orthogonal, i.e., their dot product is zero, while in the case of the eigenvectors associated with the same eigenvalue, the dot product is equal to a non-zero constant.

It is a common practice to introduce the matrix $\mathbf{A}$ eigenproperties such that:

$$\mathbf{\Phi} = \begin{bmatrix} \mathbf{\Phi_1} & ... & \mathbf{\Phi_n} \end{bmatrix} \tag{3.82}$$

$$\mathbf{\Psi} = \begin{bmatrix} \mathbf{\Psi_1}^T & ... & \mathbf{\Psi_n}^T \end{bmatrix}^T \tag{3.83}$$

Hence, (3.80) and (3.81) can be written as:

$$\mathbf{A\Phi} = \mathbf{\Phi\Lambda} \tag{3.84}$$

$$\mathbf{\Psi A} = \mathbf{\Lambda\Psi} \tag{3.85}$$

where $\mathbf{\Lambda}$ is a $n \times n$ diagonal matrix of the matrix $\mathbf{A}$ eigenvalues as diagonal elements. Accordingly, since $\mathbf{\Psi\Phi} = \mathrm{I}$, then $\mathbf{\Psi A\Phi} = \mathbf{\Lambda}$.

A new state vector $\mathbf{y} = [y_1^T y_2^T ... y_n^T]^T$ can be introduced to avoid cross-coupling among the state variables in (3.74) under the free motion (with zero input) such that:

$$\mathbf{\Delta x} = \mathbf{\Phi y} \quad or \quad \mathbf{y} = \mathbf{\Psi\Delta x} \tag{3.86}$$

The variables y_1, y_2, ..., y_n are the transformed state variables that each variable is correlated with only one mode. Thus, the right eigenvector gives the mode shape.

The mode shape's magnitude gives the state variables' activity when a specific mode is excited, while the mode shape's angle gives the phase displacement of the state variables with respect to that mode.

Accordingly,

$$\mathbf{\Delta \dot{x}} = \mathbf{A \Delta x} \tag{3.87}$$

$$\mathbf{\Phi \dot{y}} = \mathbf{A \Phi y} \tag{3.88}$$

$$\mathbf{\dot{y}} = \mathbf{\Lambda y} \tag{3.89}$$

Comparing (3.89) with (3.87), the variation of each state variable is no longer a linear combination of all the other state variables, thanks to the diagonal structure of the matrix Λ.

3.7.4 Controllability and observability

The state equation (3.74) can be reformulated using the transformed state vector $\mathbf{y}$ as follows:

$$\begin{aligned} \mathbf{\Phi \dot{y}} &= \mathbf{A \Phi y} + \mathbf{B \Delta u} \\ \mathbf{\Delta y} &= \mathbf{C \Phi z} + \mathbf{D \Delta u} \end{aligned} \tag{3.90}$$

Then, (3.90) can be written in the standard form:

$$\begin{aligned} \mathbf{\dot{y}} &= \mathbf{\Lambda y} + \mathbf{B' \Delta u} \\ \mathbf{\Delta y} &= \mathbf{C' \Phi z} + \mathbf{D \Delta u} \end{aligned} \tag{3.91}$$

where $\mathbf{B'} = \mathbf{\Phi^{-1} B}$ is the mode controllability matrix and $\mathbf{C'} = \mathbf{C \Phi}$ is the mode observability matrix. In other words, if any row of the matrix $\mathbf{B'}$ is zero, then the inputs have no control over that mode. Likewise, if any column of the matrix $\mathbf{C'}$ is zero, then the corresponding mode is unobservable in the outputs.

3.7.5 Participation factor

The participation matrix, P, is a powerful tool for recognizing the association between the state variables and modes using the left and right eigenvectors [58]:

$$\begin{aligned} \mathbf{P} &= \begin{bmatrix} \mathbf{P_1} & \dots & \mathbf{P_n} \end{bmatrix} \\ \mathbf{P_i} &= \begin{bmatrix} p_{1i} \\ \vdots \\ p_{ni} \end{bmatrix} = \begin{bmatrix} \phi_{1i}\psi_{1i} \\ \vdots \\ \phi_{ni}\psi_{ni} \end{bmatrix} \end{aligned} \tag{3.92}$$

where the dimensionless element $p_{ki} = \phi_{ki}\psi_{ki}$ is called the participation factor that identifies the participation of the *k*th state variable in the *i*th mode, and vice versa, and the sum of all the participation factors associated with any state variable or mode is equal to one.

3.8 Summary

Chapter 3 presented the background knowledge and theory required for the modeling and control of the HVDC grids and provided the basis for the stability analysis and optimization methodology given in the following chapters.

The main components in modeling the HVDC grids are the MMC and HVDC cable. The voltage and energy-based representations of the MMC average arm model were revisited in this chapter. It was shown that the MMC energy-based model can be simplified by disregarding the second harmonic component of the circulating current while implementing the compensated modulation. The resultant representation is the MMC simplified zero-sequence model that is primarily applicable to large-scale power system stability studies and is utilized throughout this thesis. The HVDC cable model reintroduced in this chapter is the frequency-dependent model with cascaded pi-sections and parallel series RL-branches. This modeling technique is suitable for state-space representation and small-signal eigenvalue stability analysis.

The MMC control hierarchy that is employed in this thesis was presented in this chapter. The hierarchy is composed of high-, mid-, and low-level controls. The high-level control is almost independent of the converter topology and is mainly associated with controlling the converter terminal characteristics that interact with the rest of the grid. In contrast, the mid-level control, which has high interactions with high- and low-level controls, is specific to MMC topology and is concerned with the circulating current control. It should be noted that the low-level control, which includes switching and energy balance among the submodule capacitors, is assumed to be ideal and is not further considered in this thesis.

The small-signal eigenvalue stability analysis, reviewed in this chapter, can be applied to obtain an intuitive insight into the dynamic interactions and transients in multiterminal HVDC grids. In addition, the state-space representation and instability sources identification that can be acquired from the small-signal analysis are prerequisites in developing an optimal feedback controller for ensuring grid stability, which is presented in the following chapters.

The discussion in this chapter serves as an introduction to the HVDC grid theory and modeling presented in the following contributions by the author:

A. Elahidoost and E. Tedeschi, "Control optimization of the offshore HVDC grid based on modular multilevel converter for improving DC voltage stability," *in The Renewable Energy & Power Quality Journal (RE&PQJ)*, vol. 18, no. 273, 2020, pp. 207–212, doi: 10.24084/repqj18.273 [18].

A. Elahidoost, L. Furieri, M. Kamgarpour and E. Tedeschi, "Optimal linear controller for minimizing DC voltage oscillations in MMC-based offshore multiterminal HVDC grids," *in IEEE Access*, vol. 9, pp. 98731-98745, 2021, doi: 10.1109/ACCESS.2021.3096291 [19].

A. Elahidoost and E. Tedeschi, "Stability improvement of MMC-based hybrid AC/DC grids through the application of a decentralized optimal controller," *IET Gener. Transm. Distrib.* 00, 1– 19 (2022), doi: 10.1049/gtd2.12497 [20].

Chapter 4

Optimal linear feedback controller

4.1 Introduction

As mentioned in previous chapters, despite the progressive advancements and innovations in HVDC systems, the interconnection of the existing and future HVDC grids, which were originally designed without detailed analyses of the unforeseen grid expansion effects, can result in interoperability issues, including stability challenges and interactions in multiterminal hybrid AC/DC grids [9, 45, 72]. These dynamic interactions on either the AC- or DC-side of the multiterminal grid can cause detrimental oscillations that propagate throughout the network due to the droop control action of the HVDC converters. Consequently, this can lead to stability deterioration, faults, and subsequent blackouts, which can result in significant damages and costs [73, 74]. Furthermore, enhancing the DC voltage stability margins is crucial to ensure the network's proper functioning since the DC voltage oscillations can impact the power balance in multiterminal HVDC grids [75]. Over the past few years, stability problems with oscillations and harmonic interactions have been observed in several HVDC-dominated grids worldwide, such as harmonic interactions and high-frequency resonances identified in the BorWin1 wind farm [76, 77], subsynchronous oscillations reported over a hundred times in the Xinjiang wind farm [78], and oscillations observed in several MMC-based HVDC grids in China and Germany [79]. Specifically, oscillations in MMC-based HVDC systems can occur in the subsynchronous to medium and high-frequency ranges [79].

Control and stability challenges in multiterminal hybrid AC/DC grids have been

addressed by a number of recent studies [80, 81, 82, 83, 84]. However, in the proposed methodologies to overcome the challenges of the dynamic interactions in hybrid AC/DC grids, stability cannot be guaranteed under the worst-case perturbation scenario found under the grid control inputs and state variables' constraints. Furthermore, the primary objective of the TEP problems is usually the minimization of costs and losses, and stability challenges such as DC voltage stability are rarely taken into account in expansion decisions [85, 86, 87]. However, stability analysis results can lead to the reconfiguration of the grid topology or adjustment of control parameters to prevent possible contingencies [88, 89, 90, 91].

Based on the preceding discussion, it can be inferred that (1) an analytical and optimal control approach is required to enhance the stability of the interconnected grids and (2) a stability decision-support criterion has to be integrated into TEP problems. As a result, the primary objective of this chapter is to introduce a methodology that ensures the stability of MMC-based multiterminal hybrid AC/DC grids through:

- Introducing a stability (oscillation) index to be integrated into the TEP problems as an additional decision-support criterion, which can measure oscillations attributed to particular variables accountable for instability in the grid.

- Identifying the worst-case perturbation scenarios, which are crucial in grid planning stages, without the need for time-consuming simulations for different configurations. It should be noted that the worst-case condition refers to the scenario in which the stability index, i.e., oscillations associated with poorly damped variables, is maximized.

- Designing an analytical and optimal controller to improve stability in MMC-based HVDC/AC grids and surpass the performance of the traditional controllers under worst-case and other operational conditions. The optimal controller can be configured in a decentralized manner to enhance grid reliability without requiring communication between converter stations.

Finally, to evaluate the applicability of the proposed optimization methodology in TEP problems, the placement of a new HVDC link between two independent VSC-based point-to-point HVDC grids in the North Sea is assessed while using the actual wind data to consider the wind intermittency effect. The aim is to include the DC voltage stability maximization under the worst-case perturbation as an additional support criterion for the HVDC network expansion decision.

4.2 Optimal control problem

In the MMC-based multiterminal hybrid AC/DC grids, the optimal control methodology is utilized to identify the worst-case perturbation scenario while considering the constraints on the control inputs and state variable fluctuations. The methodology aims to minimize oscillations caused by poorly damped modes by acting on the system eigenvalues through an optimal linear feedback controller. To achieve this objective, a centralized optimal controller is proposed, which is inspired by the approach presented in [14, 15]. The approach involves converting a non-convex min-max optimization problem into semidefinite programming (SDP) using the Lyapunov stability and linear matrix inequality (LMI) theories. The aim was to evaluate the placement of HVDC links for AC grid reinforcement by minimizing the generator frequency deviations. The methodology is adapted to reduce the poorly damped modes' oscillations, such as DC voltage oscillations in MMC-HVDC networks, which aligns with the thesis's objective.

When using a centralized configuration, the optimization procedure allows for the arbitrary assignment of values to any entry of the optimal controller matrix. Additionally, the set of potential perturbations is subject to a single constraint. Subsequently, the centralized optimal controller is transformed into a decentralized configuration. In the decentralized configuration, the optimal controller matrix is block-diagonal to align with the grid sparsity pattern. As a result, communication between converter stations is not necessary, and only local state information is required. Furthermore, constraints on the control inputs and state variables are naturally decoupled, providing greater flexibility and realism in the design process.

4.3 Problem statement

The oscillation index, J_{osci}, is formulated as a min-max optimization problem aimed at minimizing the fluctuations induced by the poorly damped modes through the use of an optimal controller, $\mathbf{K}$, under the worst-case perturbation scenario:

$$J_{osci} = \min_{\mathbf{K}} \max_{\mathbf{x}(0)\in\mathbb{X}_{\mathbf{0}}} \int_0^\infty \mathbf{z}(t)^T \mathbf{z}(t)\, dt \tag{4.1}$$

$$s.t. \quad \dot{\mathbf{x}}(t) = \mathbf{A}\mathbf{x}(t) + \mathbf{B}\mathbf{u}(t) \tag{4.2}$$

$$\mathbf{z}(t) = \mathbf{C}\mathbf{x}(t) \tag{4.3}$$

$$\mathbf{u}(t) = \mathbf{K}\mathbf{x}(t) \tag{4.4}$$

where $\mathbf{x}$, $\mathbf{u}$, and $\mathbf{z}$ are defined as the grid state, control input, and output vectors, respectively.

In the case $\mathbf{K}$ is centralized, (4.1) is subject to:

$$\mathbf{x}(0) \in \mathbb{X}_0 = \{\mathbf{x} \in \mathbb{R}^n : \mathbf{x}^T \mathbf{E}_\mathbf{x} \mathbf{x} \leq 1\} \tag{4.5}$$

$$\mathbf{u}(t) \in \mathbb{U} \ = \{\mathbf{u} \in \mathbb{R}^m : \mathbf{u}^T \mathbf{E}_\mathbf{u} \mathbf{u} \leq 1\} \tag{4.6}$$

or in the case $\mathbf{K}$ is decentralized, (4.1) is subject to:

$$\mathbf{x}(0) \in \mathbb{X}_0 = \{\mathbf{x}_i \in \mathbb{R}^{n_i} \ : \forall i \in \mathbb{Z}_{[1,r]} \ \mathbf{x}_i^T \mathbf{E}_\mathbf{x}{}^i \mathbf{x}_i \leq 1\} \tag{4.7}$$

$$\mathbf{u}(t) \in \mathbb{U} \ = \{\mathbf{u}_j \in \mathbb{R}^{m_j} : \forall j \in \mathbb{Z}_{[1,q]} \ \mathbf{u}_j^T \mathbf{E}_\mathbf{u}{}^j \mathbf{u}_j \leq 1\} \tag{4.8}$$

The oscillations of the signals of interest, $\mathbf{z}$, which are state variables associated with the poorly damped modes, are intended to be minimized. The number of the grid state variables and control inputs are represented by n and m, respectively. The control inputs are the reference parameters of the grid converters' control loops, which are further explained in chapter 3. The grid state-space matrices are $\mathbf{A} \in \mathbb{R}^{n \times n}$, $\mathbf{B} \in \mathbb{R}^{n \times m}$, and $\mathbf{C} \in \mathbb{R}^{n \times n}$. The grid optimal linear feedback controller, $\mathbf{K} \in \mathbb{R}^{m \times n}$, is used to minimize the poorly damped mode oscillations under the worst-case perturbation scenario. Problem (4.1) is subject to constraints on $\mathbf{x}(0)$ and $\mathbf{u}(t)$. Typically, the constraints have the form (4.5)-(4.6), and the optimal controller matrix $\mathbf{K}$ is allowed to be centralized. The ellipsoidal constraints on the state variables and control inputs are defined by the symmetric positive definite matrices $\mathbf{E}_\mathbf{x} > 0$ and $\mathbf{E}_\mathbf{u} > 0$, respectively, with the entries specifying the degree of freedom for the state variables and control inputs variations. The initial state perturbations constraint (4.5) confines the square root of the sum of the squares of disturbances on the state variables, and the control inputs constraint (4.6) constrains the square root of the sum of the squares of control inputs. The decentralized optimal controller $\mathbf{K}$ is proposed to address the shortcomings of the centralized problem formulation. Additionally, the decentralized problem formulation enables the decoupling of the constraints on the initial state perturbations and control inputs for each converter station, as presented in (4.7)-(4.8), increasing the constraints' flexibility and physical sensibility. The number of the ellipsoidal constraints for the grid state variables and control inputs are represented by r and q, respectively, with $\sum_{i=1}^{r} n_i = n$, and $\sum_{j=1}^{q} m_j = m$.

4.4 Problem formulation

The following subsections will demonstrate that the proposed optimal control problem, which is non-convex in both its cost function and constraints, can be transformed into a convex SDP problem through the use of the linear matrix inequalities [92].

4.4.1 Centralized optimal linear feedback controller

The solution to the non-convex min-max optimization problem for finding the optimal controller, $\mathbf{K}$, in the centralized problem formulation involves solving (4.1)-(4.6). However, this task is challenging. It can be transformed into an SDP problem by leveraging Lyapunov stability interpretation and LMI theory, which has been demonstrated in previous studies such as [14, 15]. Yet, these studies have primarily focused on minimizing the generator frequency deviations in AC grids, whereas this thesis aims to minimize poorly damped mode oscillations such as DC voltage oscillations in HVDC networks. Fig. 4.1 illustrates the architecture of the optimal linear feedback controller with four converter stations in the centralized approach. The controller, $\mathbf{K}$, receives the state variables from the converter stations, computes the new reference control inputs, and transmits them back to the converters to achieve the optimization objective.

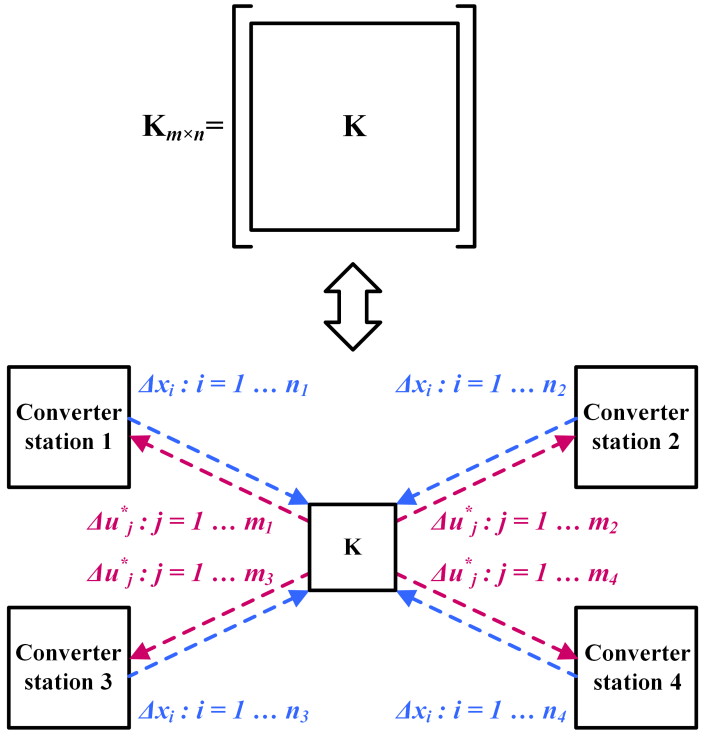

Figure 4.1: Centralized optimal linear feedback controller.

The optimal oscillation index under the worst-case perturbation scenario can be

approximated as follows such that $J_{osci} \leq \tilde{J}_{osci}$:

$$\frac{1}{\tilde{J}_{osci}} = \max_{s>0,\, \mathbf{Q}>0,\, \mathbf{Y}} s \tag{4.9}$$

$$s.t. \quad \begin{bmatrix} (\mathbf{AQ}+\mathbf{BY})+(\mathbf{AQ}+\mathbf{BY})^T & \mathbf{QC}^T \\ \mathbf{CQ} & -\mathbf{I} \end{bmatrix} \leq 0 \tag{4.10}$$

$$\begin{bmatrix} \mathbf{Q} & \mathbf{Y}^T \\ \mathbf{Y} & s{\mathbf{E_u}}^{-1} \end{bmatrix} \geq 0 \tag{4.11}$$

$$\mathbf{Q} - s{\mathbf{E_x}}^{-1} \geq 0 \tag{4.12}$$

where $s > 0$ is a scalar quantity whose inverse represents the upper bound of the optimal oscillations. It is evident that the value of the integral in (4.1) becomes $\mathbf{x}(0)^T\mathbf{P}\mathbf{x}(0)$ where $\mathbf{P} > 0$ is the solution of the Lyapunov equation. Accordingly, by defining $\mathbf{Q} = \mathbf{P}^{-1}$, the centralized optimal linear feedback controller can be recovered as $\mathbf{K} = \mathbf{Y}\mathbf{Q}^{-1}$. Namely, s, $\mathbf{Q}$, and $\mathbf{Y}$ are the solutions of the (4.9)-(4.12). Furthermore, the corresponding worst-case perturbation scenario $\mathbf{x_{0,worst}}$ can be retrieved as $\hat{\mathbf{E}}^{-T}\tilde{\mathbf{x}}$ where the Cholesky decomposition $\mathbf{E_x} = \hat{\mathbf{E}}\hat{\mathbf{E}}^T$, and $\hat{\mathbf{E}} = \mathbf{V}\mathbf{D}^{1/2}$. The columns of $\mathbf{V}$ contains the eigenvectors of $\mathbf{E_x}$, $\mathbf{D}$ is diagonal with the eigenvalues of $\mathbf{E_x}$, and $\tilde{\mathbf{x}}$ is the eigenvector of $\hat{\mathbf{E}}^{-1}\mathbf{Q}^{-1}\hat{\mathbf{E}}^{-T}$ associated with its largest eigenvalue.

The globally optimal cost $\tilde{J}_{osci}$ is therefore tightly approximated by maximizing (4.9) subject to (4.10)-(4.12). Among the three inequality constraints, the first constraint (4.10) enforces the Lyapunov stability criterion. The second constraint (4.11) and the third constraint (4.12) restrict the system control inputs and state variables within ellipsoidal constraints, which encode their physical limitations.

4.4.2 Decentralized optimal linear feedback controller

In contrast to the centralized optimal controller, the desired sparsity pattern that is block-diagonal can be achieved by the decentralized optimal linear feedback controller, as presented in (4.1)-(4.4), (4.7), and (4.8). Fig. 4.2 illustrates the architecture of the decentralized optimal linear feedback controller with four converter stations. Assuming a block-diagonal configuration of the optimal controller, $\mathbf{K}$, each block ($\mathbf{K1}$, $\mathbf{K2}$, $\mathbf{K3}$, and $\mathbf{K4}$) corresponds to a converter station, and all inter-converter entries are zero. Consequently, no data communication is necessary between converter stations, resulting in a more dependable solution. In the decentralized problem formulation, the constraints on the initial state variables' perturbations and control inputs for every converter station are decoupled, which is a physically more practical and sensible approach.

Formulation of the worst-case oscillation: Based on the Lyapunov stability theory, if $(\mathbf{A}+\mathbf{BK})$ is asymptotically stable, then the quadratic integral of (4.1) can

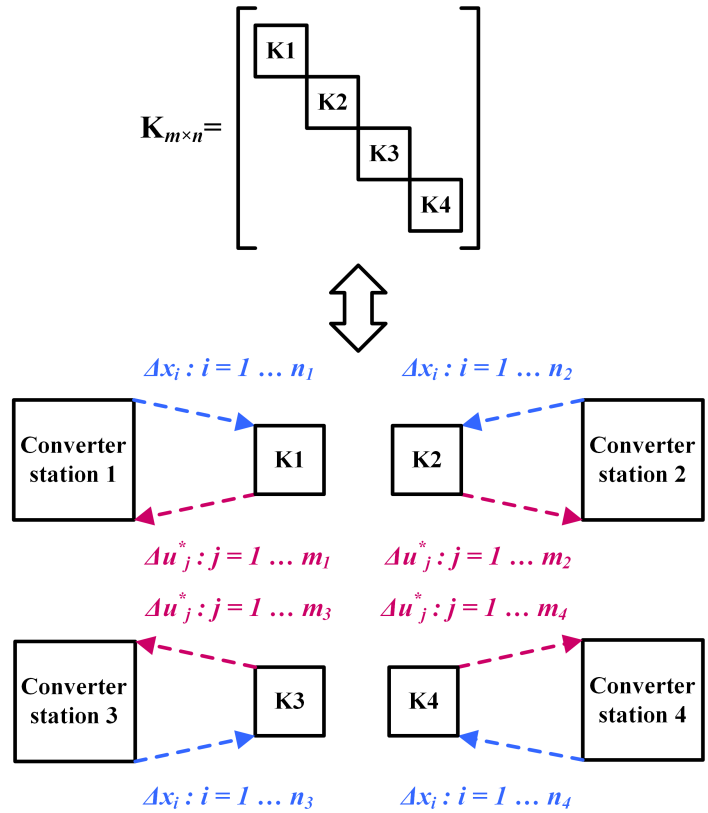

Figure 4.2: Decentralized optimal linear feedback controller.

be defined as:

$$\int_0^\infty \mathbf{x}(t)^T \mathbf{C}^T \mathbf{C} \mathbf{x}(t)\, dt = \mathbf{x}(0)^T \mathbf{P} \mathbf{x}(0) \tag{4.13}$$

where $\mathbf{P} > 0$ is the symmetric positive definite unique solution of $\mathbf{P}(\mathbf{A}+\mathbf{BK})+(\mathbf{A}+\mathbf{BK})^T\mathbf{P}+\mathbf{C}^T\mathbf{C} = 0$.

Since ${\mathbf{E}_\mathbf{x}}^i > 0$, $\forall i \in \mathbb{Z}_{[1,r]}$, then:

$${\mathbf{E}_\mathbf{x}}^i = \hat{\mathbf{E}}^i_\mathbf{x} \hat{\mathbf{E}}^{iT}_\mathbf{x}, \quad \hat{\mathbf{E}}^i_\mathbf{x} = {\mathbf{V}_\mathbf{x}}^i {\mathbf{D}_\mathbf{x}}^{i\frac{1}{2}} \tag{4.14}$$

where ${\mathbf{V}_\mathbf{x}}^i$ contains the eigenvectors of ${\mathbf{E}_\mathbf{x}}^i$ and ${\mathbf{D}_\mathbf{x}}^{i\frac{1}{2}}$ holds the square root of the ${\mathbf{E}_\mathbf{x}}^i$ eigenvalues on its diagonal. Vector $\tilde{\mathbf{x}}_i$ is specified such that $\mathbf{x}_i = (\hat{\mathbf{E}}^i_\mathbf{x})^{-T}\tilde{\mathbf{x}}_i$.

To achieve a desired block-diagonal sparsity pattern for the optimal controller $\mathbf{K}$ and to decouple the initial states into separate ellipsoids, it is necessary for the

matrix $\mathbf{P}$ to be rendered block-diagonal with dimensions $n_i \times n_i$ on its i-th block $\mathbf{P_i}$. Hence:

$$\begin{aligned}
&\max_{\mathbf{x}(0)\in\mathbb{X}_0} \mathbf{x}(0)^T\mathbf{P}\mathbf{x}(0) \\
&= \sum_{i=1}^{r} \max_{||\tilde{\mathbf{x}}_i||_2\leq 1,\, \forall i\in\mathbb{Z}_{[1,r]}} \tilde{\mathbf{x}}_i^T(\hat{\mathbf{E}}_{\mathbf{x}}^i)^{-1}\mathbf{P}_i(\hat{\mathbf{E}}_{\mathbf{x}}^i)^{-T}\tilde{\mathbf{x}}_i \\
&= \sum_{i=1}^{r} \lambda_{max}((\hat{\mathbf{E}}_{\mathbf{x}}^i)^{-1}\mathbf{P}_i(\hat{\mathbf{E}}_{\mathbf{x}}^i)^{-T})
\end{aligned} \tag{4.15}$$

Then, substituting (4.15) into (4.1) yields:

$$\begin{aligned}
&\min_{\mathbf{K}} \sum_{i=1}^{r} \lambda_{max}((\hat{\mathbf{E}}_{\mathbf{x}}^i)^{-1}\mathbf{P}_i(\hat{\mathbf{E}}_{\mathbf{x}}^i)^{-T}) \\
&s.t. \quad \mathbf{P}(\mathbf{A}+\mathbf{B}\mathbf{K})+(\mathbf{A}+\mathbf{B}\mathbf{K})^T\mathbf{P}+\mathbf{C}^T\mathbf{C} = 0
\end{aligned} \tag{4.16}$$

Next, $s_i > 0$, $\forall i \in \mathbb{Z}_{[1,r]}$ can be defined as follows:

$$\lambda_{max}((\hat{\mathbf{E}}_{\mathbf{x}}^i)^{-1}\mathbf{P}_i(\hat{\mathbf{E}}_{\mathbf{x}}^i)^{-T}) \leq \frac{1}{s_i} \tag{4.17}$$

Equation (4.17) is equivalent to:

$$\mathbf{Q}_i - s_i(\mathbf{E}_{\mathbf{x}}{}^i)^{-1} \geq 0 \tag{4.18}$$

where $\mathbf{Q}_i \geq 0$, $\mathbf{Q}_i = (\mathbf{P}_i)^{-1}$, $\forall i \in \mathbb{Z}_{[1,r]}$, and $\mathbf{Q}$ is defined to be block-diagonal such that $\mathbf{Q} = \text{blkdiag}(\mathbf{Q}_i)$.

By utilizing the Schur complement and introducing the new variable $\mathbf{Y} = \mathbf{K}\mathbf{Q}$, (4.16) can be expressed in the following form:

$$\begin{aligned}
&\min_{s_i,\, \mathbf{Q}_i\geq 0,\, \mathbf{Y}} \sum_{i=1}^{r} \frac{1}{s_i} \\
&s.t. \qquad \mathbf{Q}_i - s_i(\mathbf{E}_{\mathbf{x}}{}^i)^{-1} \geq 0,\ \forall i \in \mathbb{Z}_{[1,r]} \\
&\qquad \begin{bmatrix} (\mathbf{A}\mathbf{Q}+\mathbf{B}\mathbf{Y})+(\mathbf{A}\mathbf{Q}+\mathbf{B}\mathbf{Y})^T & \mathbf{Q}\mathbf{C}^T \\ \mathbf{C}\mathbf{Q} & -\mathbf{I} \end{bmatrix} \leq 0
\end{aligned} \tag{4.19}$$

Robustness to initial states' perturbations: Considering (4.4), (4.7), and (4.8), the control inputs must satisfy $\mathbf{u}_j^T(t)\mathbf{E}_{\mathbf{u}}{}^j\mathbf{u}_j(t) \leq 1$, $\forall j \in \mathbb{Z}_{[1,q]}$ at any time instant $t \in \mathbb{R}_0^+$, that $\mathbf{u}_j(t) = \mathbf{K}_j\mathbf{x}(t)$, and $\mathbf{K} = \text{blkcol}(\mathbf{K}_j)$. In other words, $\mathbf{x}(t)^T\mathbf{K}_j^T\mathbf{E}_{\mathbf{u}}{}^j\mathbf{K}_j\mathbf{x}(t) \leq 1$, $\forall j \in \mathbb{Z}_{[1,q]}$ should hold for any time instant $t \in \mathbb{R}_0^+$.

Since $\mathbf{P}$ can also be interpreted as level sets for the state variables' trajectories, if it satisfies $\mathbf{x}(t_1)^T\mathbf{P}\mathbf{x}(t_1) \leq k$ for some $k > 0$ at time instant $t_1 \in \mathbb{R}_0^+$, it will also hold for all time instants $t > t_1$. Therefore:

$$\mathbf{x}(t)^T\mathbf{P}\mathbf{x}(t) \leq \max_{\mathbf{x}(0)\in\mathbb{X}_0} \mathbf{x}(0)^T\mathbf{P}\mathbf{x}(0) \leq \sum_{i=1}^{r} \frac{1}{s_i} \tag{4.20}$$

where (4.20) can alternatively be expressed as $\mathbf{x}(t)^T \frac{\mathbf{P}}{\sum_{i=1}^{r} \frac{1}{s_i}} \mathbf{x}(t) \leq 1$.

Therefore, the constraints on the control inputs can be formulated as follows:

$$\mathbf{K}_j^T {\mathbf{E}_\mathbf{u}}^j \mathbf{K}_j \leq \frac{\mathbf{P}}{\sum_{i=1}^{r} \frac{1}{s_i}}, \forall j \in \mathbb{Z}_{[1,q]} \tag{4.21}$$

where (4.21) is equivalent to $\mathbf{Q} - \mathbf{Y}_j^T {\mathbf{E}_\mathbf{u}}^j \sum_{i=1}^{r} \frac{1}{s_i} \mathbf{Y}_j \geq 0$.

Therefore, by using the Schur complement, the former can be formulated as:

$$\begin{bmatrix} \mathbf{Q} & \mathbf{Y}_j^T \\ \mathbf{Y}_j & ({\mathbf{E}_\mathbf{u}}^j)^{-1}(\sum_{i=1}^{r} \frac{1}{s_i})^{-1} \end{bmatrix} \geq 0, \forall j \in \mathbb{Z}_{[1,q]} \tag{4.22}$$

It is worth noting that if $r = 1$, then (4.22) is an SDP constraint, and the problem of (4.19), and (4.22) entails a convex formulation by maximizing s instead of minimizing $\frac{1}{s}$. However, when $r > 1$, additional elaboration is necessary to achieve a convex problem formulation.

Convex problem formulation: The harmonic mean of $s_i > 0, \forall i \in \mathbb{Z}_{[1,r]}$ is formulated as:

$$h(s) = \frac{r}{\sum_{i=1}^{r} \frac{1}{s_i}} \tag{4.23}$$

Then, a new decision variable w is introduced, subject to the constraint $w \leq h(s)$, which modifies (4.23) to:

$$\sum_{i=1}^{r} \frac{w^2}{s_i} \leq rw \tag{4.24}$$

Next, to represent (4.24) in a different form, a set of decision variables $y_i, \forall i \in \mathbb{Z}_{[1,r]}$ is introduced, resulting in:

$$w^2 \leq s_i y_i, \quad \sum_{i=1}^{r} y_i = rw, \quad \forall i \in \mathbb{Z}_{[1,r]} \tag{4.25}$$

Therefore, (4.25) can be expressed as the second-order cone programming constraint:

$$\left\| \begin{matrix} 2w \\ s_i - y_i \end{matrix} \right\|_2 \leq s_i + y_i, \quad \forall i \in \mathbb{Z}_{[1,r]} \tag{4.26}$$

Thus, a feasible SDP formulation of the decentralized optimal control problem can be obtained by:

$$\frac{1}{\tilde{J}_{osci}} = \max_{s_i>0,\, \mathbf{Q}_i>0,\, \mathbf{Y},\, w,\, y_i} w \tag{4.27}$$

$$s.t. \quad \begin{bmatrix} (\mathbf{AQ}+\mathbf{BY})+(\mathbf{AQ}+\mathbf{BY})^T & \mathbf{QC}^T \\ \mathbf{CQ} & -\mathbf{I} \end{bmatrix} \leq 0 \tag{4.28}$$

$$\begin{bmatrix} \mathbf{Q} & \mathbf{Y}_j^T \\ \mathbf{Y}_j & \frac{w}{r}(\mathbf{E_u}^j)^{-1} \end{bmatrix} \geq 0, \quad \forall j \in \mathbb{Z}_{[1,q]} \tag{4.29}$$

$$\mathbf{Q}_i - s_i(\mathbf{E_x}^i)^{-1} \geq 0, \qquad \forall i \in \mathbb{Z}_{[1,r]} \tag{4.30}$$

$$\left\| \begin{matrix} 2w \\ s_i - y_i \end{matrix} \right\|_2 \leq s_i + y_i, \qquad \forall i \in \mathbb{Z}_{[1,r]} \tag{4.31}$$

$$\sum_{i=1}^{r} y_i = rw, \quad \mathbf{Q} = \text{blkdiag}(\mathbf{Q}_i) \tag{4.32}$$

$$\mathbf{Y} = \text{blkcol}(\mathbf{Y}_i), \quad \mathbf{Y} \text{ is decentralized.} \tag{4.33}$$

Equations (4.29) and (4.30) represent the distinct ellipsoidal inequality constraints on the control inputs and state variables, respectively. The decentralized formulation allows for different inequality constraints to be established for each converter station, taking into account their maximum permissible voltages and currents.

4.4.3 Optimization methodology interpretation

The optimization methodology with its inputs and outputs is illustrated in Fig. 4.3.

The optimization procedure takes matrices $\mathbf{A}_{n\times n}$, $\mathbf{B}_{n\times m}$, and $\mathbf{C}_{n\times n}$ as inputs. The linearization of the grid state-space model around its operating point yields matrices $\mathbf{A}_{n\times n}$ and $\mathbf{B}_{n\times m}$. Additionally, the small-signal eigenvalue stability analysis enables the determination of the diagonal matrix $\mathbf{C}_{n\times n}$, which represents the state variables associated with the poorly damped modes.

The optimization objective of the presented methodology is to minimize the oscillations caused by the poorly damped modes through the centralized/decentralized optimal linear feedback controller under the worst-case perturbation scenario, as given in (4.1). This worst-case scenario, $\mathbf{\Delta x_{0,worst}}$, is obtained by imposing coupled/decoupled ellipsoidal constraints on the state variables and control inputs. The ellipsoidal constraints are defined by the symmetric positive definite matrices $\mathbf{E_x}^i$ and $\mathbf{E_u}^j$, which can be tuned to set the limits. The selection of these matrices significantly influences the outputs of the optimization methodology and should be sensibly chosen. In the case of the decentralized optimization, the desired structure of the optimal controller (illustrated in Fig. 4.2) can be achieved by setting the

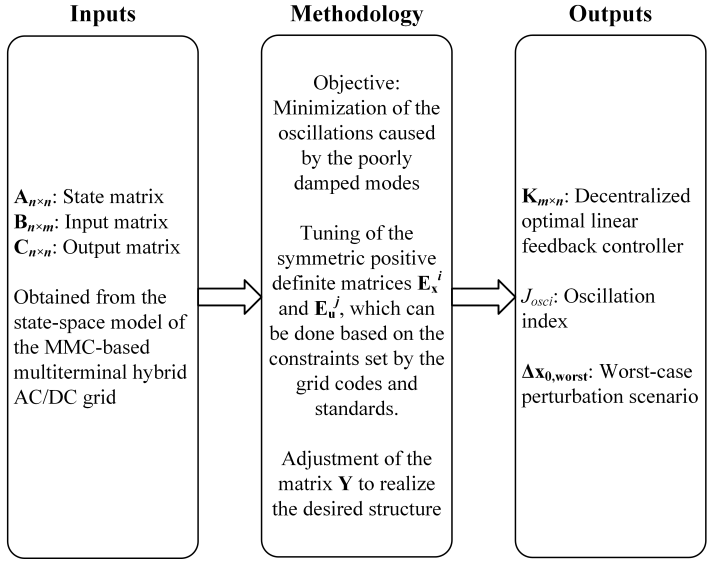

Figure 4.3: The optimization methodology with its inputs and outputs.

relevant entries of the matrix $\mathbf{Y}$ to zero.

The outputs of the optimization procedure include the optimal controller, $\mathbf{K}_{m\times n}$, the oscillation index, J_{osci}, and the worst-case perturbation scenario, $\mathbf{\Delta x_{0,worst}}$. The oscillation index is the objective function minimized by the optimization process, and it represents the amount of oscillation caused by the poorly damped modes. This index can also serve as a stability decision-support criterion in TEP problems.

4.5 Optimizing HVDC grid expansion decision considering DC voltage stability

As previously mentioned, the continuous expansion in the number of offshore wind farms and the requirement to transfer significant amounts of intermittent wind energy to onshore load centres have resulted in the deployment of point-to-point HVDC grids in the North Sea. It is projected that offshore wind resources will contribute to over one-fifth of Europe's total wind capacity by 2030 [93]. This development anticipates the establishment of multiterminal HVDC grids, which result from the gradual connection of pre-existing and independently designed HVDC links. The design, control, and stability of such a system pose unprecedented challenges and opportunities.

When deploying highly interconnected offshore grids, the expansion planning stage is crucial due to its technical and economic implications. Common expansion planning approaches often neglect the grid's stability and control, relying solely on techno-economical optimization. However, HVDC links can play a key role in ensuring stability and mitigating issues such as congestion and power imbalances [94]. Therefore, their contribution to grid stability and control must be appropriately accounted for during the expansion planning stage [95]. In offshore environments, guaranteeing grid stability is of utmost importance due to the high operation and maintenance costs. In particular, DC voltage stability, which is sensitive to power imbalances caused by intermittent wind power injection and fault conditions on the connected AC terminals, should be the primary focus when operating multiterminal HVDC systems [96]. DC voltage stability can be jeopardized by resonances triggered under specific modes of operation and due to the non-passive behavior of the VSCs that can be considered as a source of instability [73, 97]. Hence, maintaining DC voltage within a predefined range at all terminals and under all operating scenarios is necessary (during steady-state and under dynamics) [75]. Furthermore, wind energy intermittency should not be disregarded in grid expansion problems as it can significantly affect operational conditions.

In the subsequent sections, a methodology is presented for examining the optimal placement of a new HVDC link between two independent VSC-based point-to-point HVDC grids, resulting in minimal DC voltage oscillations under the worst-case perturbation scenario. Specifically, the oscillation index, formulated as a decentralized problem, is employed to identify which HVDC link among four scenarios should be installed to minimize the DC voltage oscillations under the worst-case perturbation scenario. In addition, a decentralized optimal linear feedback controller is deployed to attain such minimization while satisfying decoupled control inputs and state variables constraints. The impact of wind intermittency based on actual wind data is also taken into account, demonstrating that stability considerations based on the nominal operating conditions are insufficient when planning grid expansion.

4.5.1 Wind energy data analysis

In this section, the effect of wind intermittency on power extraction from offshore wind farms is analyzed using actual wind datasets. Two locations in the North Sea are selected, and wind data time series were extracted using the Reanalysis dataset. The dataset provides the average wind speed with a spatial resolution of 2.5 degrees and a temporal resolution of 6 hours from 2001-2005 [98]. The offshore sites chosen for analysis are Johan-Sverdrup, Norway, and BorWin1, Germany. To obtain hourly time series at the selected points, linear interpolation has been applied. The wind speed time series correspond to the height of 45 m above the sea

surface, and since wind turbines' hub height is typically higher (around 100 m), adjustment factors based on [99] are used to calculate the wind power time series.

Fig. 4.4 illustrates the histogram of the hourly wind speed at the height of 45 m for both Johan-Sverdrup and BorWin1 locations over five years. The average wind speed for Johan-Sverdrup is approximately 8.67 m/s, and for BorWin1, it is around 8.26 m/s. The minimum and maximum wind speed values for Johan-Sverdrup are 0.63 m/s and 29.47 m/s, respectively, while for BorWin1, they are 0.78 m/s and 28.27 m/s, respectively. The histogram shows that the wind data can be fitted well into the Weibull probability distribution function. The normalized mean wind power curves, presented in Fig. 4.5, represent the average power curves for multiple wind turbines in the regions, obtained by fitting the power-speed dataset into a polynomial curve. Wind power time series are computed as a function of normalized mean wind power curves, with the product of wind speed time series and adjustment factors used as inputs:

$$p = f(av) \tag{4.34}$$

where f denotes the normalized mean wind power curve, a represents the adjustment factor, and v is the wind speed. Adjustment factors compensate for discrepancies between the actual and computed wind energy and are obtained based on [98]. The normalized wind power histograms for the two offshore sites are presented in Fig. 4.6. Notably, for both locations, the probability of wind farms producing 10% of the nominal power is the highest, followed by 90% of the nominal power production as the second-highest probability.

Assuming that there is a requirement to connect the BorWin1 wind farm to a newly constructed wind farm at the Johan-Sverdrup site through an offshore HVDC cable, the total wind power production in the resulting HVDC network is quantified by evaluating the concurrent occurrence of the normalized power in four ranges (0-0.25 pu, 0.25-0.5 pu, 0.5-0.75 pu, and 0.75-1 pu) at the two farms. Table 4.1 displays the results of this analysis. The intersection of the normalized power range of 0-0.25 pu at both locations indicates a 22% probability of both wind farms generating power within the 0-0.25 pu range simultaneously.

4.5.2 VSC-based offshore multiterminal HVDC grid modeling

The case study under consideration is a VSC-based offshore four-terminal HVDC grid with the configuration and parameters reported in [100], as shown in Fig. 4.7. Cable 1-2 represents the HVDC link from Johan-Sverdrup to the onshore grid in Norway, which is 200 kilometers long, while cable 3-4 represents a point-to-point HVDC link between BorWin1 and Germany, also 200 kilometers in length. It is assumed that there is a plan to interconnect the two networks to enhance grid

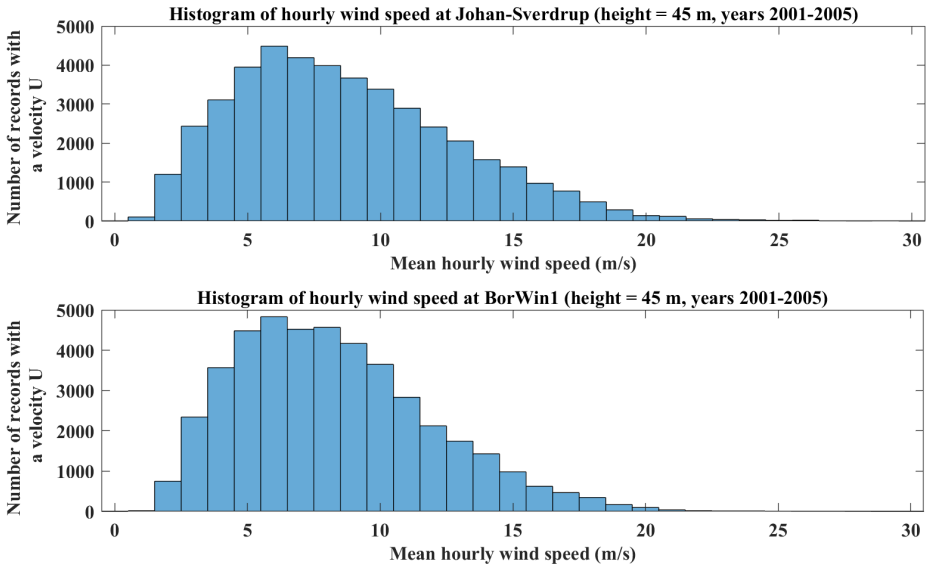

Figure 4.4: Histograms of hourly wind speed at Johan-Sverdrup and BorWin1 (height = 45 m, years 2001-2005).

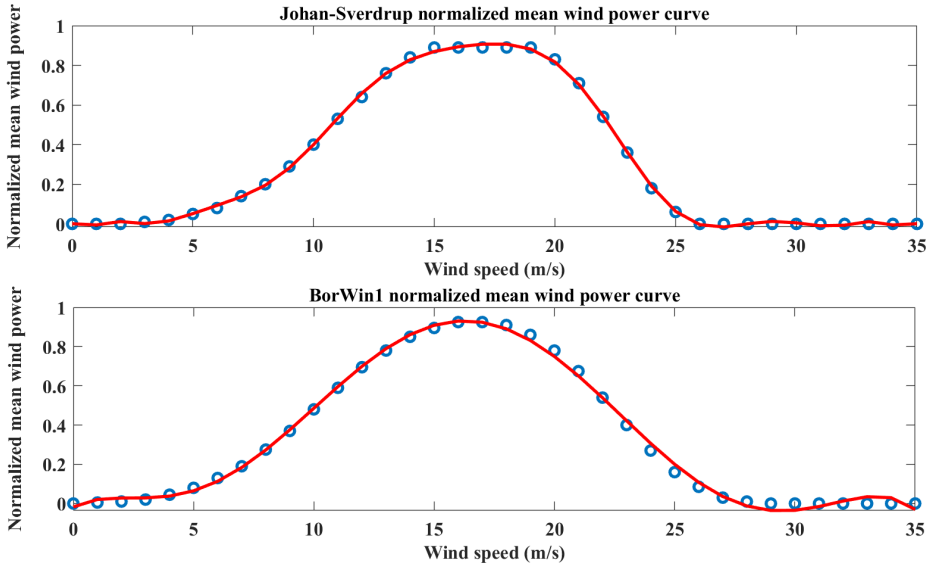

Figure 4.5: Johan-Sverdrup and BorWin1 normalized mean wind power curves.

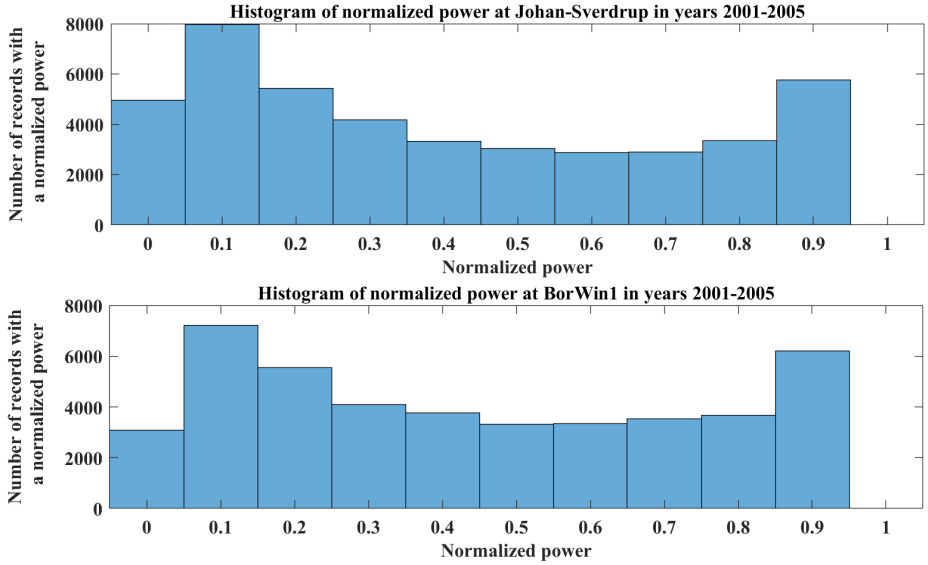

Figure 4.6: Histograms of normalized power at Johan-Sverdrup and BorWin1 in years 2001-2005.

Table 4.1: Probability of simultaneous occurrence of normalized power at Johan-Sverdrup and BorWin1 locations (Base power: 1200 MVA).

Normalized power ranges (pu)		**BorWin1**			
		0 - 0.25	**0.25 - 0.5**	**0.5 - 0.75**	**0.75 - 1**
Johan-Sverdrup	**0 - 0.25**	0.22	0.09	0.06	0.04
	0.25 - 0.5	0.07	0.05	0.04	0.04
	0.5 - 0.75	0.04	0.04	0.04	0.05
	0.75 - 1	0.03	0.04	0.05	0.09

availability. The main challenge in this scenario is to select the appropriate line that will optimize grid performance by minimizing the DC voltage oscillations under dynamics and transients while taking into account the productivity of the weather-dependent wind farms. It is important to note that environmental and regulatory constraints, such as water depth restrictions or Exclusive Economic Zones (EEZ), are not considered in the selection of the HVDC link.

This first study assumes that the four offshore and onshore converter stations are type 2-Level Voltage Source Converters (2-L VSC), and they are modeled in a synchronously rotating *dq*-reference frame. Fig. 4.8 depicts a simplified archi-

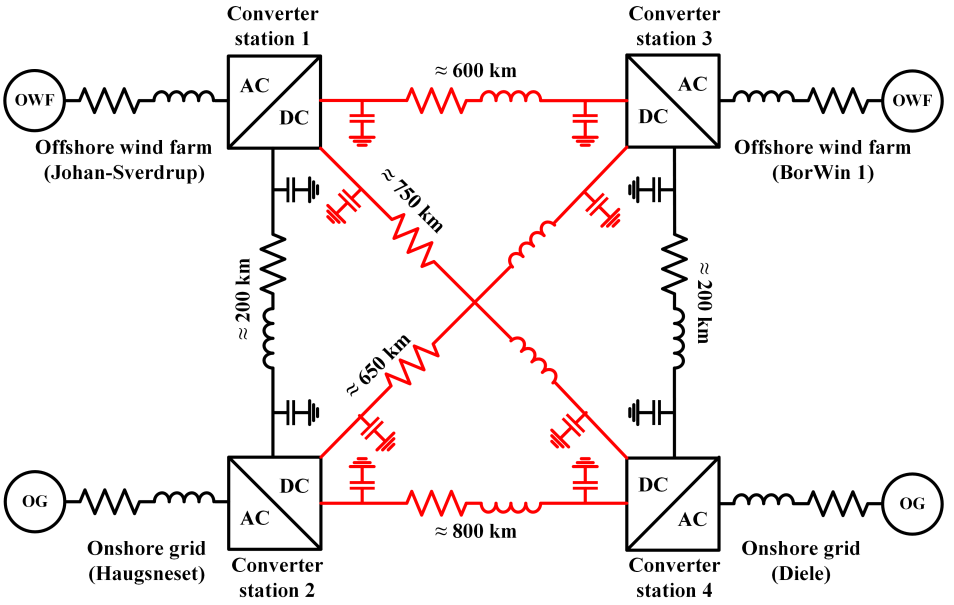

Figure 4.7: VSC-based offshore four-terminal HVDC grid: existing links (black lines) and possible expansion links (red lines).

tecture of the 2-L VSC with its corresponding control system. The PI controller is responsible for controlling the AC-side current, while the decentralized optimal controller controls the DC-side voltage. To apply the decentralized optimization methodology, the entire HVDC grid, which includes the converters with current controllers and cables, needs to be represented by the state-space equations (4.2) and (4.3), and then linearized around an equilibrium point.

The state vector, denoted as $\mathbf{x}$, comprises a total of 23 elements, including the dq-components of the AC-side currents, $i_{ac,dq}$, the integral states of the inner-loop dq-components AC-side current controller, ξ_{iacdq}, the DC-side voltages, v_{dc}, as well as the DC-side cable currents, i_{dc}. Specifically, the state vector for the configuration with the link 1-3, which connects the two point-to-point HVDC grids, can be represented as follows:

$$\begin{aligned}\mathbf{x_{1-3}} = [&i_{ac,d1}\ i_{ac,q1}\ \xi_{iacd1}\ \xi_{iacq1}\ v_{dc1}\ i_{dc12}\ i_{ac,d2}\ i_{ac,q2}\ \xi_{iacd2}\ \xi_{iacq2}\ v_{dc2}\ i_{dc13}\\ &i_{ac,d3}\ i_{ac,q3}\ \xi_{iacd3}\ \xi_{iacq3}\ v_{dc3}\ i_{dc34}\ i_{ac,d4}\ i_{ac,q4}\ \xi_{iacd4}\ \xi_{iacq4}\ v_{dc4}]^T\end{aligned} \tag{4.35}$$

where the dependence of x_{1-3} on time is not explicitly shown in the notation for simplicity.

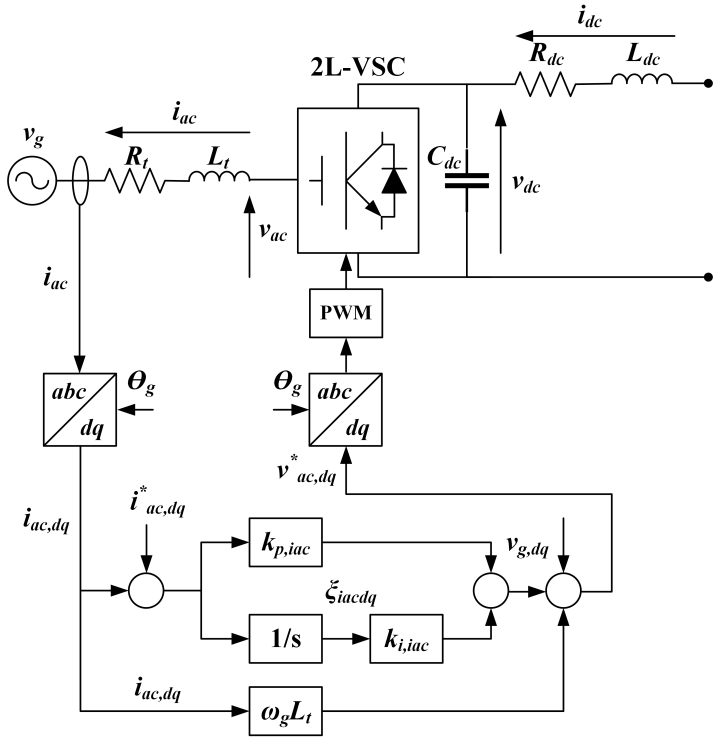

Figure 4.8: Simplified architecture of the 2L-VSC with the corresponding control.

The control input vector, $\mathbf{u}$, consists of the dq-components of the converters' AC-side reference currents, i.e.:

$$\mathbf{u} = [i^*_{ac,d1}\ i^*_{ac,q1}\ i^*_{ac,d2}\ i^*_{ac,q2}\ i^*_{ac,d3}\ i^*_{ac,q3}\ i^*_{ac,d4}\ i^*_{ac,q4}]^T \tag{4.36}$$

The output vector, $\mathbf{z}$, which is a subset of the desired state variables, includes only the converters' DC-side voltages where the goal is to minimize their variations:

$$\mathbf{z} = [v_{dc1}\ v_{dc2}\ v_{dc3}\ v_{dc4}]^T \tag{4.37}$$

The optimization problem can be solved using the linearized model around a specific equilibrium point to determine the optimal HVDC link ($1-3$, $1-4$, $2-3$, or $2-4$) with minimum DC voltage oscillations under the worst-case perturbation scenario. The cost function of this problem, which represents a "DC voltage oscillation index," can be expressed as the integral of the square of the $\mathbf{z}$ over time until steady-state (refer to (4.1)). The control input constraints must be satisfied to realize the initial state perturbations, and these constraints are modeled as decoupled ellipsoidal constraints on $i^*_{ac,d}$ and $i^*_{ac,q}$ for each converter station. The

decoupled ellipsoidal constraints reflect the limitation on the allowed AC-side current variations on the d- and q-axes of each converter and consider that the current capability of each converter does not affect that of the other converters at other terminals. Due to the diverse nature of the scalar state variables in (4.35), the initial state perturbations are modeled as separate ellipsoidal sets for different sets of the state variables. For example, it is assumed that $i_{ac,d}$ and $i_{ac,q}$ belong to different two-dimensional ellipsoids for each converter station, while v_{dc} belongs to one-dimensional ellipsoidal sets for each converter station. This yields a more realistic result than the coupled ellipsoidal constraints in the centralized problem formulation mentioned in section 4.4.1. A total of 15 decoupled ellipsoidal sets of perturbations for different initial state variables are defined.

4.6 Simulation results

A study has been conducted to examine how wind variability affects the HVDC grid's operating point and its consequent impact on the optimization procedure. The nonlinear equations of (4.2) and (4.3) are linearized around different operating conditions resulting from each wind scenario. Therefore, the $\mathbf{A}$ and $\mathbf{B}$ matrices' elements are contingent on the wind scenario. The calculation of the DC voltage oscillation index, J_{osci}, is performed for various operating points that correlate with different wind speeds and the corresponding wind power extractions.

Implementation of the decentralized optimal problem formulation given in equations (4.27)-(4.33) can be easily achieved by utilizing the YALMIP toolbox [101] of Matlab, along with the MOSEK solver [102]. Once the optimal solution ($\mathbf{Q}$, $\mathbf{Y}$, s, w, y) is obtained, the worst initial perturbation, $\mathbf{\Delta x_{0,worst}}$, the oscillation index, $\tilde{J}_{osci}$, and the corresponding decentralized optimal controller, $\mathbf{K}$, can be retrieved. The matrix $\mathbf{P}$ is calculated as the inverse of $\mathbf{Q}$. For each $j \in \mathbb{Z}[1, q]$, $\mathbf{\Delta x_{0,worst}}$ is calculated as the eigenvector corresponding to the maximum eigenvalue of $(\hat{\mathbf{E}}_{\mathbf{x}}^{i})^{-1}\mathbf{P}_i(\hat{\mathbf{E}}_{\mathbf{x}}^{i})^{-T}$. Then, $\mathbf{x}(0)_{worst}$ is set to $\mathbf{\Delta x_{0,worst}}$, $\tilde{J}_{osci}$ is computed as $\mathbf{x}(0)_{worst}^{T}\mathbf{P}\mathbf{x}(0)_{worst}$, and $\mathbf{Y}$ is set to $\mathbf{KQ}$. Alternatively, the oscillation index, $\tilde{J}_{osci}$, can be determined through simulation by applying the decentralized optimal controller, $\mathbf{K}$, and integrating the trajectory of $\mathbf{z}(t) = \mathbf{C}\mathbf{x}(t)$ over time until steady-state is achieved.

Considering (4.35), (4.36), and (4.37), the input matrices of the optimization procedure have the following dimensions: $\mathbf{A}_{23\times23}$, $\mathbf{B}_{23\times8}$, and $\mathbf{C}_{23\times23}$. The matrices $\mathbf{A}$ and $\mathbf{B}$ are obtained by linearizing the grid state-space model around its operating point, while the diagonal matrix $\mathbf{C}$ corresponds to the DC-side voltage state variables.

The diagonal matrices ${\mathbf{E}_{\mathbf{u}}}^{j}$, where $j \in \mathbb{Z}_{[1,q]}$ $(q = 4)$, are selected to enforce the

boundedness of the dq-component AC-side reference currents at each terminal as prescribed in (4.8):

$$\left((\Delta i^*_{ac,d})^2 + (\Delta i^*_{ac,q})^2\right)^{1/2} \leq 0.5 \text{ pu} \tag{4.38}$$

To enforce constraints (4.7) on the maximum allowable deviations of the initial state variables (4.39)-(4.42), diagonal matrices $\mathbf{E_x}^i$ were employed, where $i \in \mathbb{Z}_{[1,r]}$ and $r = 15$. Additionally, the boundaries for the AC-side currents are obtained from [103], while the limitations on the DC-side currents and voltages are based on the physical properties of the HVDC cable. For further information on the optimization matrices, please refer to Appendix B.

$$\left((\Delta i_{ac,d})^2 + (\Delta i_{ac,q})^2\right)^{1/2} \leq 0.1 \text{ pu} \tag{4.39}$$

$$|\Delta v_{dc}| \leq 0.1 \text{ pu} \tag{4.40}$$

$$\left((\Delta \xi_{iacd})^2 + (\Delta \xi_{iacq})^2\right)^{1/2} \leq 0.01 \text{ pu} \tag{4.41}$$

$$|\Delta i_{dc}| \leq 0.1 \text{ pu} \tag{4.42}$$

Table 4.2 presents simulation results for various scenarios. The wind farm operating points are determined as the average of each normalized power range listed in Table 4.1, resulting in four values that are applied to offshore converter stations 1 and 3, leading to 16 unique scenarios with varying linearization trajectories for equations (4.2) and (4.3). The converter station 2 is kept at a constant operating condition of 0.75 per unit, corresponding to a passive load, and the converter station 4 represents the slack bus, ensuring the grid power balance. The oscillation index, which represents the DC voltage oscillations under the worst-case initial conditions, varies between scenarios, as seen in Table 4.1. The AC-side reference current is represented by $i^*_{ac,d1}$ for Johan-Sverdrup and $i^*_{ac,d3}$ for BorWin1. Assuming the d-component AC-side reference voltages at all four terminals are one per unit (base voltage: 400 kV), the per unit average power values can be replaced with per unit current values. The oscillation indices are calculated for the 16 possible scenarios based on the four different grid topologies resulting from the connection of the two point-to-point HVDC networks through the four HVDC links ($1-3$, $1-4$, $2-3$, or $2-4$). The minimum DC voltage oscillation index in each scenario is highlighted in blue. Adding the HVDC link 1-4 results in the optimal DC voltage oscillation index in seven scenarios, while adding HVDC links 1-3 and 2-3 leads to the optimal solution in three and six cases, respectively. The addition of the HVDC link 2-4 does not result in a minimum DC voltage oscillation in any scenario.

The optimal DC voltage oscillation index is obtained in the radial network, which is formed by connecting the two point-to-point HVDC grids through the link 2-3 when $i^*_{ac,d1}$ and $i^*_{ac,d3}$ are generating -0.875 per unit power. This condition is considered as the nominal operating condition since it is the closest to the nominal power capacity of both wind farms. This would be the only scenario taken into consideration if only nameplate information (and no wind time series) was available for the wind farms. However, to account for the probability of each operating condition, the average DC voltage oscillation index is calculated as the sum of the products between the DC voltage oscillation indices and the corresponding event probability given in Table 4.1. Therefore, the link with the lowest average DC voltage oscillation index is the optimal HVDC link expansion option that ensures the best stability performance at the worst-case initial condition. As seen in Table 4.3, the HVDC link between substations 1 and 3 gives the lowest average DC voltage oscillation index and, hence, the optimal solution from the stabilization standpoint. However, if the assessment of the oscillation index was only based on the nominal operating condition and did not consider the intermittency of the wind speed, it could have led to selecting the link 2-3 as the new HVDC link, which would not be the optimal solution from the stability standpoint.

Table 4.2: DC voltage oscillation indices of the four-terminal HVDC grid under different scenarios (different added HVDC links and different *d*-component AC-side reference currents).

Added HVDC link	**Added HVDC link's length (km)**	***d*-component AC-side reference current in per-unit**		**DC voltage oscillation index**	***d*-component AC-side reference current in per-unit**		**DC voltage oscillation index**	***d*-component AC-side reference current in per-unit**		**DC voltage oscillation index**	***d*-component AC-side reference current in per-unit**		**DC voltage oscillation index**	***i*ac,d1*: Johan-Sverdrup reference**
1-3	**600**	*i*ac,d1*	-0.125	3.73	*i*ac,d1*	-0.125	4.10	*i*ac,d1*	-0.125	3.98	*i*ac,d1*	-0.125	3.71	
1-4	**750**	*i*ac,d2*	0.75	4.21	*i*ac,d2*	0.75	4.16	*i*ac,d2*	0.75	3.63	*i*ac,d2*	0.75	2.93	**-0.125**
2-3	**650**	*i*ac,d3*	-0.125	5.08	*i*ac,d3*	-0.375	4.84	*i*ac,d3*	-0.625	5.09	*i*ac,d3*	-0.875	3.50	
2-4	**800**	*i*ac,d4*	-0.5	5.59	*i*ac,d4*	-0.25	5.09	*i*ac,d4*	0	5.25	*i*ac,d4*	0.25	3.89	
1-3	**600**	*i*ac,d1*	-0.375	3.87	*i*ac,d1*	-0.375	4.19	*i*ac,d1*	-0.375	3.89	*i*ac,d1*	-0.375	3.80	
1-4	**750**	*i*ac,d2*	0.75	5.23	*i*ac,d2*	0.75	3.80	*i*ac,d2*	0.75	3.30	*i*ac,d2*	0.75	3.95	**-0.375**
2-3	**650**	*i*ac,d3*	-0.125	4.83	*i*ac,d3*	-0.375	5.04	*i*ac,d3*	-0.625	3.64	*i*ac,d3*	-0.875	3.78	
2-4	**800**	*i*ac,d4*	-0.25	5.34	*i*ac,d4*	0	5.28	*i*ac,d4*	0.25	3.79	*i*ac,d4*	0.5	3.91	
1-3	**600**	*i*ac,d1*	-0.625	4.01	*i*ac,d1*	-0.625	4.10	*i*ac,d1*	-0.625	3.85	*i*ac,d1*	-0.625	3.92	
1-4	**750**	*i*ac,d2*	0.75	3.86	*i*ac,d2*	0.75	3.70	*i*ac,d2*	0.75	3.80	*i*ac,d2*	0.75	3.52	**-0.625**
2-3	**650**	*i*ac,d3*	-0.125	5.00	*i*ac,d3*	-0.375	3.63	*i*ac,d3*	-0.625	3.76	*i*ac,d3*	-0.875	3.49	
2-4	**800**	*i*ac,d4*	0	5.33	*i*ac,d4*	0.25	3.80	*i*ac,d4*	0.5	3.87	*i*ac,d4*	0.75	4.00	
1-3	**600**	*i*ac,d1*	-0.875	3.57	*i*ac,d1*	-0.875	3.85	*i*ac,d1*	-0.875	3.92	*i*ac,d1*	-0.875	3.82	
1-4	**750**	*i*ac,d2*	0.75	3.29	*i*ac,d2*	0.75	3.51	*i*ac,d2*	0.75	3.84	*i*ac,d2*	0.75	4.25	**-0.875**
2-3	**650**	*i*ac,d3*	-0.125	3.52	*i*ac,d3*	-0.375	3.69	*i*ac,d3*	-0.625	3.59	*i*ac,d3*	-0.875	3.69	
2-4	**800**	*i*ac,d4*	0.25	3.93	*i*ac,d4*	0.5	3.94	*i*ac,d4*	0.75	4.01	*i*ac,d4*	1	3.99	
***i*ac,d3*: BorWin1 reference**		**-0.125**			**-0.375**			**-0.625**			**-0.875**			

Table 4.3: DC voltage oscillation index at nominal condition versus average DC voltage oscillation index.

Added HVDC link	Added HVDC link's length (km)	DC voltage oscillation index at nominal condition	Average DC voltage oscillation index
1-3	**600**	3.82	3.88
1-4	**750**	4.25	3.96
2-3	**650**	3.69	4.37
2-4	**800**	3.99	4.71

As an illustration, the expansion problem can be evaluated by considering two equally important criteria: a) minimizing the average ohmic cable losses; and b) minimizing the average DC voltage oscillation index. The average ohmic cable losses are obtained by following the same procedure as the average DC voltage oscillation index, i.e., taking into account the probability of the occurrence of each operating scenario. Based on these criteria, the optimal HVDC link expansion option achieves the lowest values for both criteria. In this particular case, link 1-3 is identified as the best choice, which is also the closest point to the origin in Fig. 4.9. However, different expansion planning priorities may lead to different preferred configurations, depending on the weights assigned to each criterion.

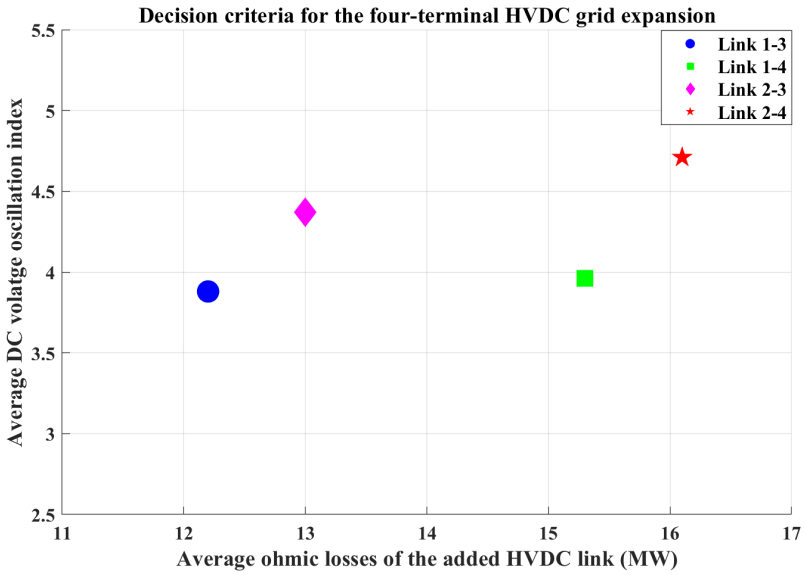

Figure 4.9: Comparison of the considered expansion options.

4.7 Summary and conclusion

An optimal analytical methodology was put forward in this chapter that enables the minimization of the oscillations that stem from poorly damped modes in the worst initial perturbation scenario, while simultaneously enforcing the constraints on the control inputs and state variables. A stability index was introduced as a decision-support criterion in TEP problems, which is capable of measuring the oscillations of the potential instability sources subject to the worst-case perturbation scenario. By utilizing this method, the identification of the worst initial perturbation scenario can be accomplished without resorting to time-consuming dynamic simulations of the HVDC grid configurations, thereby potentially benefiting grid expansion planning.

Based on the Lyapunov stability and linear matrix inequality (LMI) theories, the proposed optimal controller was derived from a non-convex min-max optimization problem that is converted into semidefinite programming (SDP). In the decentralized problem formulation, the grid sparsity pattern is matched by making the optimal controller matrix block-diagonal. As a result, communication between converter stations is unnecessary, and only local state information is needed. Additionally, constraints on the control inputs and state variables can be easily decoupled, providing greater flexibility and feasibility in the design.

The proposed approach's effectiveness was assessed in minimizing the DC voltage oscillations in a four-terminal HVDC grid, with a focus on wind intermittency's impact on power production from connected wind farms. A case study was conducted on the placement of a new HVDC link between two independent point-to-point HVDC grids located in the North Sea. The main objective was to determine the link that ensures the minimum DC voltage oscillations under the worst-case initial perturbation, with the decentralized optimal controller providing the required performance. In this expansion decision, different links' contributions to grid stabilization were considered, which depend on the wind variability-induced specific operating conditions. The analysis revealed that taking this variability into account leads to a different expansion decision than relying on the assumption of the constant power production by wind farms. Furthermore, the active power loss on HVDC cables was considered as an additional criterion to guide the expansion decision, and the study demonstrated that both criteria identify the same link as the optimal expansion alternative in this case.

The discussion in this chapter is partially supported by the following contributions by the author:

A. Elahidoost, L. Furieri, E. Tedeschi and M. Kamgarpour, "Optimizing HVDC

grid expansion and control for enhancing DC stability," *2018 Power Systems Computation Conference (PSCC)*, 2018, pp. 1-7, doi: 10.23919/ PSCC.2018.8442753 [16].

A. Elahidoost, L. Furieri, E. Tedeschi and M. Kamgarpour, "Reducing HVDC network oscillations considering wind intermittency through optimized grid expansion decision," *2018 IEEE Energy Conversion Congress and Exposition (ECCE)*, 2018, pp. 2683-2690, doi: 10.1109/ECCE.2018.8557546 [17].

A. Elahidoost, L. Furieri, M. Kamgarpour and E. Tedeschi, "Optimal linear controller for minimizing DC voltage oscillations in MMC-based offshore multiterminal HVDC grids," *in IEEE Access*, vol. 9, pp. 98731-98745, 2021, doi: 10.1109/ ACCESS.2021.3096291 [19].

A. Elahidoost and E. Tedeschi, "Stability improvement of MMC-based hybrid AC/DC grids through the application of a decentralized optimal controller," *IET Gener. Transm. Distrib.* 00, 1– 19 (2022), doi: 10.1049/gtd2.12497 [20].

Chapter 5

Centralized and decentralized optimal controllers in MMC-based HVDC grids

5.1 Introduction

The minimization of the DC voltage oscillations for HVDC link placement in multiterminal grids was studied in the preceding chapter, with an initial attempt to focus on the potential use of the oscillation index as a decision-support criterion in TEP problems. However, only HVDC networks based on the 2-level VSCs were analyzed, and the internal dynamics of the MMCs resulting from the circulating currents were ignored, as neither control nor modulation suppressed these currents. Additionally, the performance of both centralized and decentralized optimal controllers was not assessed via small-signal eigenvalue stability analysis or time-domain simulations.

This chapter aims to investigate thoroughly how the centralized and decentralized optimal linear feedback controllers can minimize the DC voltage oscillations under the worst-case perturbation scenario in MMC-based multiterminal HVDC grids. The optimal controller improves the DC voltage stability margins and prevents potential critical interactions among different converter stations resulting from interconnecting point-to-point HVDC grids. To achieve this goal, the chapter tackles the challenges arising from the internal dynamics of the MMCs caused by the circulating currents and their potential impact on DC voltage oscillations in multiterminal configurations. In addition, since most existing research on multiterminal HVDC grid control has used a droop control strategy [104, 105, 106, 107, 108], the

chapter examines the effect of droop gains' variation on the DC voltage stability margins of an MMC-based four-terminal HVDC grid. Lastly, the chapter evaluates and compares the performance of the decentralized optimal controller to the centralized optimal controller using eigenvalue stability analysis and time-domain simulations.

5.2 State-space model of the MMC-based HVDC grid

The HVDC grid test system proposed in [100] is utilized to construct the MMC-based offshore four-terminal HVDC grid illustrated in Fig. 5.1, and its model parameters are listed in Table 5.1. The HVDC test grid is almost the same as the one introduced in Chapter 4 and is revisited here for convenience. The interconnection of two independent point-to-point HVDC links between offshore wind farms and onshore power grids (MMC1 to MMC3 and MMC2 to MMC4) is considered to simulate a real case with actual wind speed time series and distances between locations. The North Sea's BorWin1 wind farm and Johan-Sverdrup oil and gas platform are selected as the two offshore locations. While BorWin1 is already connected to the HVDC grid, Johan-Sverdrup is currently an HVDC-connected oil and gas platform, but Utsira High, where it is located, has been identified as a possible offshore wind site in Norway [109]. The stabilizing effects of the four potential expansion routes (indicated by dashed red lines in Fig. 5.1) on the multiterminal HVDC grid are evaluated to select the optimal route.

Table 5.1: MMC-based offshore four-terminal HVDC grid parameters.

Symbol	Value	Symbol	Value
S_b	900 MVA	$k_{p,iac}$	2.57
V_b^{ac}	320 kV	$k_{i,iac}$	57.61
V_b^{dc}	640 kV	$k_{p,ic0}$	0.83
R_t	1.77 Ω	$k_{i,ic0}$	8.64
L_t	56.3 mH	$k_{p,pac}$	0.0033
R_a	0.89 Ω	$k_{i,pac}$	222.18
L_a	84.8 mH	$k_{p,qac}$	0.0033
R_{ac}	$R_t + R_a/2$	$k_{i,qac}$	222.18
L_{ac}	$L_t + L_a/2$	$k_{p,w\Sigma 0}$	0.54
C_a	0.29 μF	$k_{i,w\Sigma 0}$	9.1
C_{eq}	10 μF	ρ	0.1
C_{dc}	0.16 μF/km	f_n	50 Hz
R_{dc1}	2.65 Ω/km	L_{dc1}	6.016×10^{-1} mH/km
R_{dc2}	1.218×10^{-1} Ω/km	L_{dc2}	3.02×10^{-1} mH/km
R_{dc3}	1.6×10^{-2} Ω/km	L_{dc3}	2.8 mH/km

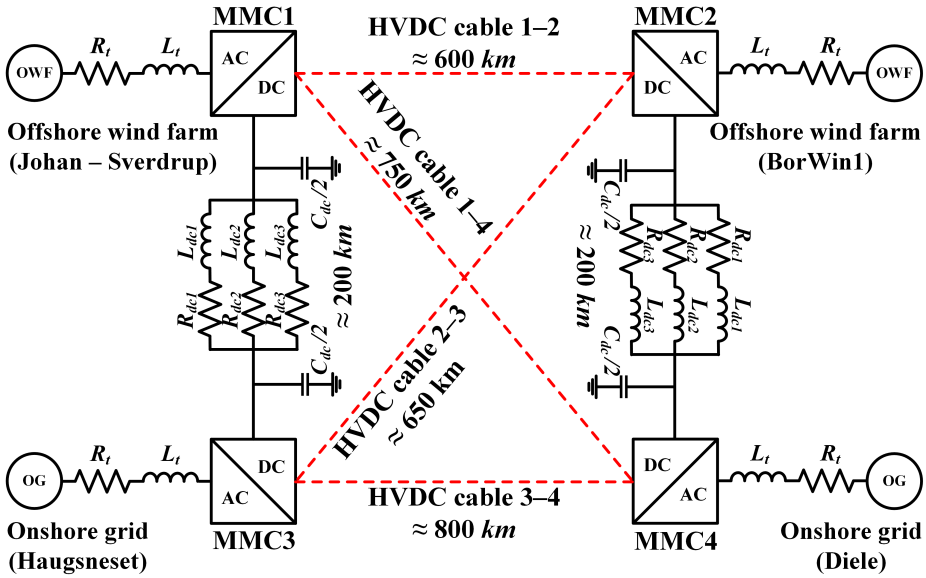

Figure 5.1: MMC-based offshore four-terminal HVDC grid: Dashed red lines are the potential HVDC link expansion routes.

The SSTI state-space model of the test grid is obtained and validated in the following subsections, which is necessary for the small-signal eigenvalue stability analysis. This analysis has two main objectives. First, it aims to derive the matrices $\mathbf{A} \in \mathbb{R}^{n \times n}$, $\mathbf{B} \in \mathbb{R}^{n \times m}$, and $\mathbf{C} \in \mathbb{R}^{n \times n}$ required for the optimal control formulation defined in Chapter 4, aiming to minimize the DC voltage oscillations of the MMC-based four-terminal HVDC grid under the worst-case perturbation scenario. The second objective is to gain a better understanding of the grid dynamics and stability margins, which are dependent on the modeling and control parameters. The eigenvalue analysis results, along with time-domain simulations, are then used to validate the performance of the optimal linear feedback controller.

5.2.1 State-space representation of the MMC

The simplified zero-sequence model, which is derived from the energy-based representation of the converter with compensated modulation (CM) as discussed in Chapter 3, is used to develop the state-space model of the MMC. The MMC configuration and applied control strategy are illustrated in Fig. 3.1, 3.3, and 3.5, and the SSTI equations are provided in (3.45)-(3.47), and (3.51). It is worth noting that the converters at the offshore wind farms are operated in the power mode with a zero droop gain, while in multiterminal configurations, the onshore grid MMCs

participate in DC-side voltage control via the DC-droop mode control. Thus, the $\mathbf{x}_{mmc}$, $\mathbf{u}_{mmc}$, and $\mathbf{z}_{mmc}$ vectors for the state-space representation of every MMC station can be expressed as follows:

$$\mathbf{x}_{mmc} = [i_{ac,d}\ i_{ac,q}\ \xi_{iacd}\ \xi_{iacq}\ i_{c0}\ \xi_{ic0}\ v_{dc}\ \xi_{pac}\ \xi_{qac}\ w_{\Sigma 0}\ \xi_{w\Sigma 0}]^T \tag{5.1}$$

$$\mathbf{u}_{mmc} = [v_{dc}^*\ p_{ac}^*\ q_{ac}^*\ w_{\Sigma 0}^*]^T \tag{5.2}$$

$$\mathbf{z}_{mmc} = [v_{dc}]^T \tag{5.3}$$

The reference DC-side voltage, denoted as v_{dc}^*, is used as a control input of the vector $\mathbf{u}$ in MMCs employing the DC-droop mode control. Therefore, the total number of the state variables for the MMC is $n_{mmc} = 11$, while the number of control inputs varies depending on the type of the MMC control used. For MMC operating in the DC-droop mode control, the number of the control inputs is $m_{mmc} = 4$, whereas for other MMCs in the power mode control, it is $m_{mmc} = 3$.

5.2.2 State-space representation of the HVDC cable

In Chapter 3, the modeling of the HVDC cable is discussed, which is based on the frequency-dependent cascaded pi-sections with parallel series RL-branches as illustrated in Fig. 5.1. The damping characteristics of the HVDC cable in the frequency domain are accurately captured by this model. Furthermore, it is suitable for state-space representation and small-signal eigenvalue stability analysis. Equation (3.50) presents the SSTI HVDC cable equations with one pi-section and three parallel series branches. The impact of the equivalent HVDC cable shunt capacitance, C_{dc}, is accounted for in (3.51). Consequently, each HVDC cable incorporates three DC-side current state variables ($n_{cable} = 3$) as follows:

$$\mathbf{x}_{cable} = [i_{dc1}\ i_{dc2}\ i_{dc3}]^T \tag{5.4}$$

5.2.3 State-space model of the test grid

A general form of the state-space model for the MMC-based four-terminal HVDC grid, with the expansion link $1-4$ as an example (refer to Fig. 5.1), can be expressed based on (3.70) with the overall $\mathbf{x}$, $\mathbf{u}$, and $\mathbf{z}$ vectors:

$$\mathbf{x} = [\mathbf{x}_{mmc1}^T\ \mathbf{x}_{cable1-3}^T\ \mathbf{x}_{mmc3}^T\ \mathbf{x}_{cable1-4}^T\ \mathbf{x}_{mmc4}^T\ \mathbf{x}_{cable2-4}^T\ \mathbf{x}_{mmc2}^T]^T \tag{5.5}$$

$$\mathbf{u} = [\mathbf{u}_{mmc1}^T\ \mathbf{u}_{mmc3}^T\ \mathbf{u}_{mmc4}^T\ \mathbf{u}_{mmc2}^T]^T \tag{5.6}$$

$$\mathbf{z} = [\mathbf{z}_{mmc1}^T\ \mathbf{z}_{mmc3}^T\ \mathbf{z}_{mmc4}^T\ \mathbf{z}_{mmc2}^T]^T \tag{5.7}$$

where the converter stations' numbers, as depicted in Fig. 5.1, are referred to by the indices 1, 2, 3, and 4. Subsequently, the total number of grid state variables and control inputs are $n = 53$ and $m = 14$, respectively.

To validate the accuracy of the resulting SSTI state-space (SS) model, time-domain simulation is required. To accomplish this, a MATLAB/Simulink circuit-based (CB) model of the HVDC grid is created using the Simscape toolbox. In the CB model, the MMC is simulated using the average arm model (AAM), where each converter arm is represented by a controlled voltage source with an equivalent arm capacitance [48, 54]. The AAM modeling technique is a well-established and reliable method that considers all the converter's non-linearities and internal dynamics, while ignoring the submodule (SM) capacitor voltage balancing algorithm and switching operation. To excite the grid dynamically, a 10% step increase is introduced to v_{dc4} at $t = 0.5\ s$, followed by a 50% step reduction to p_{ac1} at $t = 1\ s$. Fig. 5.2 illustrates the simulation results, which demonstrate the dynamic response of the CB and SS models in all four converter stations for v_{dc} and p_{ac} waveforms. The figure clearly shows that the two models match quite well, thereby confirming that the SSTI state-space model can accurately capture the grid dynamics during transients.

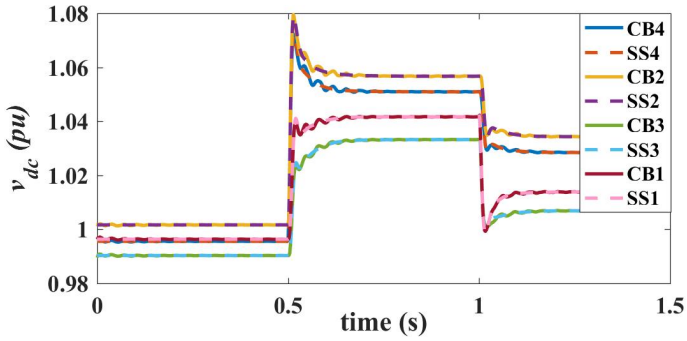

(a) DC-side voltages.

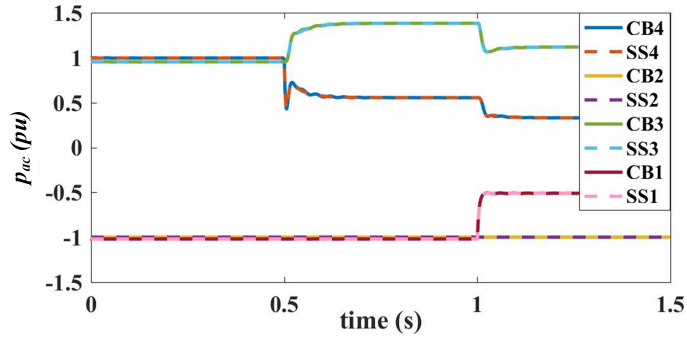

(b) AC-side active powers.

Figure 5.2: Time-domain verification of the SSTI state-space (SS) model and circuit-based (CB) model of the MMC-based four-terminal HVDC grid with the expansion link 1-4.

5.2.4 Small-signal eigenvalue stability analysis of the test grid

The small-signal dynamic model can be derived from the SSTI state-space model of the test grid that has been developed. This involves obtaining the steady-state operating point by solving the equilibrium $\dot{\mathbf{x}} = 0$ under the grid's nominal working conditions, where the wind farms are running at their full power capacity. The resulting operating point is labeled as $\mathbf{x}_0$ [58], and the linearization of equation (3.70) is performed around this point. The linearized small-signal model produces matrices $\mathbf{A} \in \mathbb{R}^{n \times n}$ and $\mathbf{B} \in \mathbb{R}^{n \times m}$, which can be incorporated into the optimal control problem formulation. Furthermore, the matrix $\mathbf{C} \in \mathbb{R}^{n \times n}$ is diagonal and its entries correspond to the $\mathbf{z}$ vector (5.7).

The small-signal eigenvalue stability analysis is conducted to investigate the dynamic properties and stability margins of the system and verify the performance of the optimal controller. Subsequently, Table 5.2 presents the most dominant grid eigenvalues or modes that are closest to the right half-plane, along with their respective damping ratios, oscillatory frequencies, and primary participating states whose values are greater than 5%, listed in descending order of magnitude. Participating states are defined as the state variables that contribute to their corresponding modes. As shown in the table, the grid's most dominant oscillatory modes, which are specific to MMCs, involve the zero-sequence energy sums and their related integral states, as well as the integral states of the zero-sequence circulating current. This suggests that analyses based on 2-level VSC [16, 17, 104, 105] should be re-evaluated as they cannot capture the most relevant MMC dynamics. The stability of the associated state variables is ensured by appropriately tuning the converters' control parameters. The oscillatory modes of interest are the $\lambda_{17,18}$ and $\lambda_{14,15}$ because they are closest to the right half-plane with the highest participation from the $v_{dc1,2,3,4}$ and $\xi_{pac3,4}$, which directly affect the $v_{dc1,2,3,4}$ oscillations. The states $v_{dc1,2,3,4}$ and $\xi_{pac3,4}$ are related through the converters' droop gain. Fig. 5.3 demonstrates the grid's eigenvalue trajectory for MMC3 and MMC4 droop gain variation from 0.01 to 0.2, where the droop gain increase has improved the stability margin of $\lambda_{14,15}$ while $\lambda_{17,18}$ has moved further towards the right half-plane, getting closer to instability. However, the imaginary parts of both $\lambda_{14,15}$ and $\lambda_{17,18}$ are reduced, indicating a lower oscillation frequency. Hence, it is evident that the droop gain can play a critical role in DC-side voltage stability. Due to the trade-off between $\lambda_{14,15}$ and $\lambda_{17,18}$ when the droop gain increases, it is essential to use an optimization strategy to readjust the droop optimally.

Hence, to efficiently retune the droop gains by relocating the $\lambda_{14,15}$ and $\lambda_{17,18}$ eigenvalues for enhancing the DC voltage stability margins under the worst-case perturbation scenario, the optimal linear feedback controller is employed in the four-terminal HVDC grid.

Table 5.2: The most dominant eigenvalues and their primary participating states of the MMC-based four-terminal HVDC grid with the expansion Link 1-4.

No.	Eigenvalue	Damping ratio	Oscillation frequency	Main participating states
$\lambda_{31,32,33}$	–9.2	1	–	$\xi_{ic01,2,3,4}$, $\xi_{w\Sigma01,2,3,4}$, $w_{\Sigma01,2,3,4}$
λ_{30}	–11.7	1	–	$\xi_{ic03,4}$
$\lambda_{21,22}$	$-15.1 \pm j\ 20.4$	0.59	3.2 HZ	$w_{\Sigma03,4}$, $\xi_{w\Sigma03,4}$, $i_{dc3,14}$, $\xi_{ic03,4}$, $w_{\Sigma02}$, $\xi_{w\Sigma02}$
$\lambda_{23,24}$	$-16.2 \pm j\ 23.7$	0.56	3.8 HZ	$w_{\Sigma02}$, $\xi_{w\Sigma02}$, ξ_{ic02}, $w_{\Sigma01,4}$, $\xi_{w\Sigma01,4}$, $\xi_{ic01,4}$
$\lambda_{25,26}$	$-16.2 \pm j\ 23.8$	0.56	3.8 HZ	$w_{\Sigma01}$, $\xi_{w\Sigma01}$, ξ_{ic01}, $w_{\Sigma02,3}$, $\xi_{w\Sigma02,3}$, $\xi_{ic02,3}$
$\lambda_{27,28}$	$-21.8 \pm j\ 15.1$	0.82	2.4 HZ	$w_{\Sigma03,4}$, $\xi_{w\Sigma03,4}$, $\xi_{ic03,4}$, $w_{\Sigma01,2}$, $\xi_{w\Sigma01,2}$, $\xi_{ic01,2}$
$\lambda_{42,43,44,45,48,51,52,53}$	–22.4	1	–	$\xi_{iacd1,2,3,4}$, $\xi_{iacq1,2,3,4}$
λ_{29}	–31.9	1	–	$i_{dc3,14}$, $i_{dc3,13}$, $\xi_{ic03,4}$, $\xi_{w\Sigma03,4}$, $w_{\Sigma03,4}$
λ_{20}	–45.7	1	–	$i_{dc3,24}$, $i_{dc2,24}$, $w_{\Sigma02}$, $\xi_{w\Sigma02}$
λ_{19}	–47.8	1	–	$i_{dc3,13}$, $i_{dc3,14}$, v_{dc1}, $i_{dc2,13}$, $w_{\Sigma01}$, $\xi_{w\Sigma01}$
$\lambda_{17,18}$	$-116.6 \pm j\ 161.3$	0.59	25.7 HZ	$v_{dc1,2,3,4}$, $\xi_{pac3,4}$
$\lambda_{14,15}$	$-158 \pm j\ 307$	0.46	48.9 HZ	$i_{dc2,14}$, $v_{dc1,2,3,4}$, $\xi_{pac3,4}$
$\lambda_{1,2}$	$-224.1 \pm j\ 1046.7$	0.21	166.7 HZ	v_{dc3}, $i_{dc2,13}$, v_{dc1}, ξ_{pac3}
$\lambda_{3,4}$	$-227.4 \pm j\ 967.4$	0.23	154.0 HZ	$i_{dc2,24}$, $v_{dc2,4}$
$\lambda_{34,35,40,41,49,50}$	–233.7	1	–	$\xi_{pac1,2,3,4}$, $\xi_{qac1,2,3,4}$
λ_{16}	–321.2	1	–	$i_{dc2,14}$, $\xi_{pac3,4}$, $i_{dc2,13}$

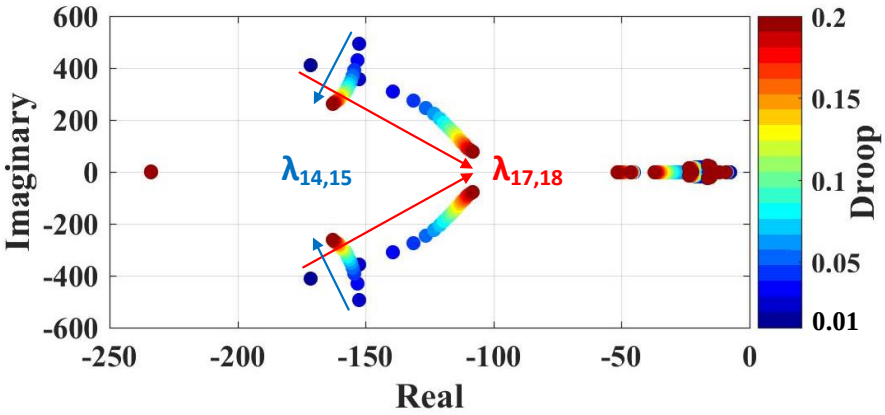

Figure 5.3: Eigenvalue trajectory for droop variation from 0.01 to 0.2.

5.3 Simulation results

The YALMIP toolbox [101] of MATLAB in combination with the MOSEK solver [102] is used to solve the centralized and decentralized optimization problem formulations, (4.9)-(4.12), and (4.27)-(4.33). Time-domain simulations in MATLAB/ Simulink are then conducted under different case studies to compare the performance of the centralized and decentralized optimal linear feedback controllers in minimizing the DC voltage oscillations under the worst-case perturbation scenario. The controllers' ability to modify the droop gain and replace the droop control function is evaluated, and it is demonstrated that both approaches can improve the grid DC voltage stability margins.

5.3.1 Optimal controller performance

Under consideration is the MMC-based offshore four-terminal HVDC grid with the expansion link 1-4, as illustrated in Fig. 5.1, under nominal operating conditions. The state-space matrices $\mathbf{A} \in \mathbb{R}^{n \times n}$, $\mathbf{B} \in \mathbb{R}^{n \times m}$, and $\mathbf{C} \in \mathbb{R}^{n \times n}$ are obtained based on the derivations outlined in Chapter 4. By running the optimal control problem, one can attain the optimal linear feedback controller, $\mathbf{K}$, the worst initial perturbation scenario $\mathbf{x}_{0,worst}$, and the DC voltage oscillation index J_{osci}. The optimal controller, $\mathbf{K}$, can be implemented in time-domain simulations to minimize the DC voltage oscillation index under the worst initial perturbation scenario, as shown in Fig. 5.4.

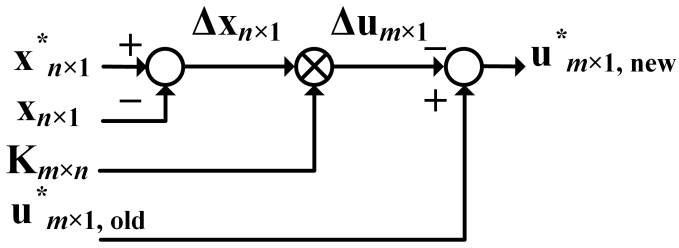

Figure 5.4: Centralized/decentralized optimal linear feedback controller implementation.

Case study I: Optimal controller in the presence of the droop control

At $t = 7\,s$, the MMC4 reference DC-side voltage undergoes a 35% step increase. This specific scenario is selected as it closely resembles the worst initial perturbation scenario $\mathbf{x}_{0,worst}$. The matrices $\mathbf{E_u}$ and $\mathbf{E_x}$, are constructed with equal weight assigned to all control inputs and state variables, except for the integral states, which are granted a lesser degree of freedom. The grid waveforms for different scenarios are illustrated in Fig. 5.5. The network DC-side voltages are observed to increase by approximately 20% due to the droop control action ($\rho = 0.1$) following the 35% step increase of the v^*_{dc4}, as depicted in Fig. 5.5(a). Subsequently, the v_{dc} waveforms exhibit increasing amplitude oscillations until the system becomes unstable, as illustrated in Fig. 5.5.

Fig. 5.6 illustrates the efficiency of the centralized optimal linear feedback controller in stabilizing the system under the aforementioned disturbance. The implementation of the centralized optimal controller leads to the movement of the system eigenvalues associated with v_{dc} oscillations ($\lambda_{1,2,3,4,14,15,17,18}$) further away from the right half-plane (–185.9 $\pm\, j$ 246.4, –208.3 $\pm\, j$ 326, –264 $\pm\, j$ 970.9, and –267.3 $\pm\, j$ 1046.1), resulting in an improvement in their corresponding damping ratios (0.6, 0.54, 0.26, and 0.25, respectively). Additionally, the worst-case scenario $\mathbf{x}_{0,worst}$ was found to have all entries as zero, except for the grid DC-side voltages ($v_{dc,1,2,3,4} = 0.6, 0.1, 0.2, 0.8$). The centralized optimal linear feedback controller is a 14×53 matrix, with the highest value entries located between a control input from one converter and a state variable in another converter. These entries in the centralized optimal linear feedback controller correspond to $\xi_{pac1,2,3,4}$ and $v^*_{dc3,4}$, $\xi_{pac1,2,3,4}$ and $w^*_{\Sigma 01,2,3,4}$, and $\xi_{pac1,2}$ and $p^*_{ac1,2}$, which is consistent with the results obtained from the small-signal eigenvalue stability analysis presented in Table 5.2. Indeed, the modification of the droop gains by the centralized optimal controller is aimed at reducing the v_{dc} oscillations under the worst-case perturbation scenario.

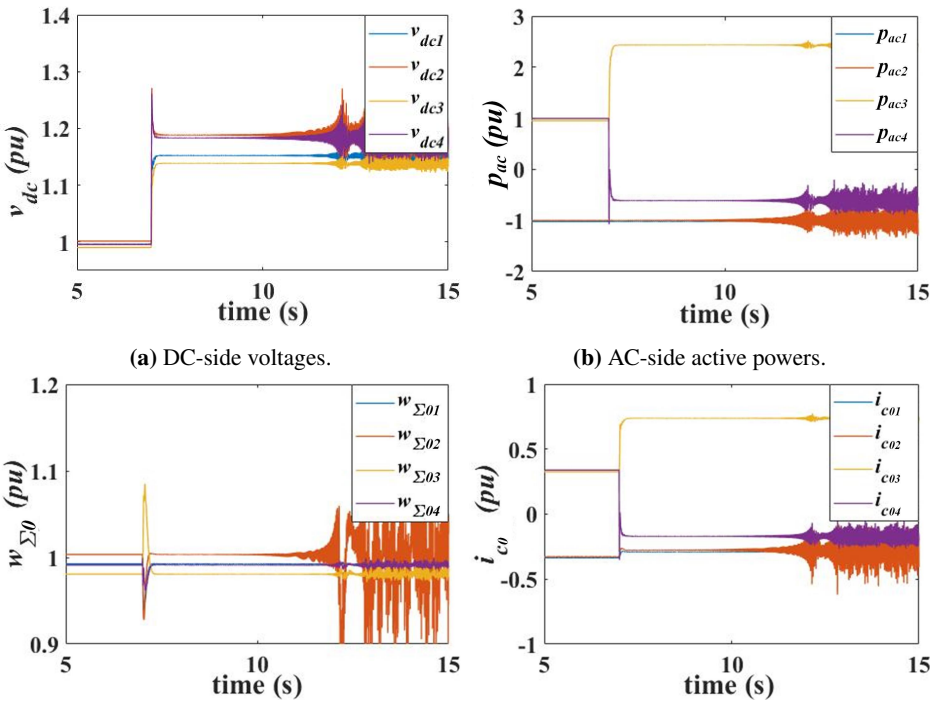

(a) DC-side voltages.

(b) AC-side active powers.

(c) Zero-sequence energy sums.

(d) Zero-sequence circulating currents.

Figure 5.5: MMCs' waveforms after applying a 35% step increase to the MMC4 DC-side voltage at $t = 7\ s$: without optimal linear feedback controller.

Fig. 5.7 presents the results of the decentralized optimal linear feedback controller's performance when subjected to a 35% step increase in the v^*_{dc4} variable. To restrict the control inputs within separate ellipsoidal constraints, the $\mathbf{E_u}^j$ matrices are defined as follows:

$$|\Delta v^*_{dc}| \leq 1 \text{ pu} \tag{5.8}$$

$$\left(\Delta(p^*_{ac})^2 + \Delta(q^*_{ac})^2\right)^{1/2} \leq 1 \text{ pu} \tag{5.9}$$

$$|\Delta w^*_{\Sigma 0}| \leq 1 \text{ pu} \tag{5.10}$$

The $\mathbf{E_x}^i$ matrices, on the other hand, are assigned values to ensure that the state variables remain within a reasonable range and can be adjusted according to the desired offshore HVDC grid codes and standards. A 0.15 pu limit is adopted from the Commission Regulation (EU) 2016/1447 network code [110] on the required AC-side voltage ranges to maintain the HVDC converter's connection to the network at the connection point. The limits for the DC-side voltages and other state

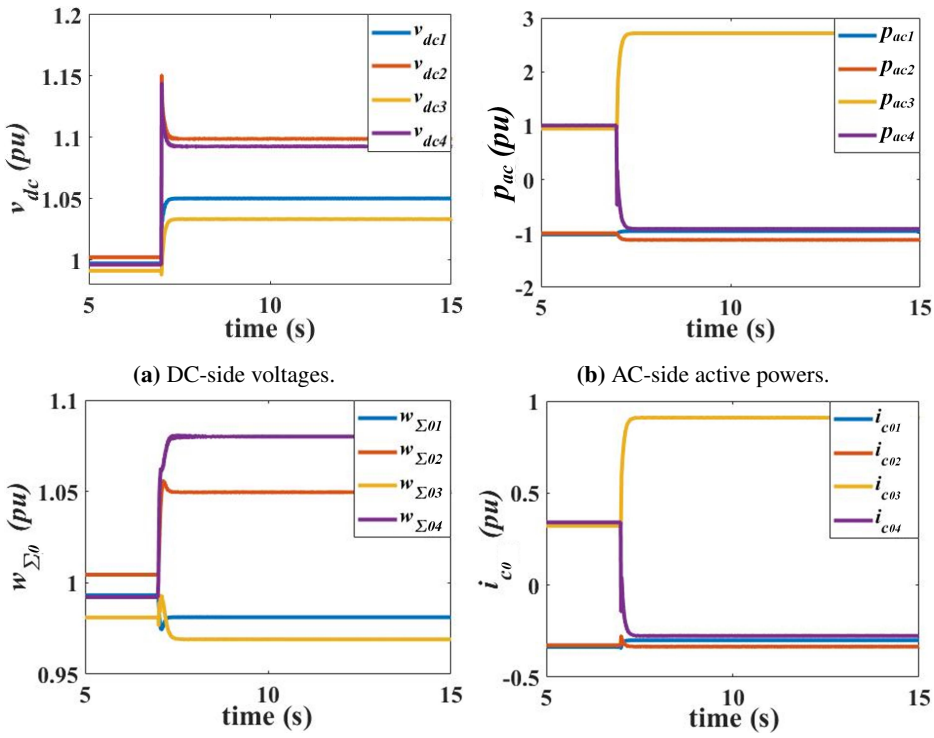

(a) DC-side voltages.

(b) AC-side active powers.

(c) Zero-sequence energy sums.

(d) Zero-sequence circulating currents.

Figure 5.6: MMCs' waveforms after applying a 35% step increase to the MMC4 DC-side voltage at $t = 7\ s$: with centralized optimal linear feedback controller and droop.

variables are also set to 0.15 pu, with the exception of the integral parameters of the state variables and $w_{\Sigma 0}$, which is proportional to the sum of the arm capacitor voltages squared:

$$|\Delta i_{ac}| = \left(\Delta i_{ac,d}^2 + \Delta i_{ac,q}^2\right)^{1/2} \leq 0.15 \text{ pu} \tag{5.11}$$

$$|\Delta \xi_{iac}| = \left(\Delta \xi_{iacd}^2 + \Delta \xi_{iacq}^2\right)^{1/2} \leq \varepsilon \tag{5.12}$$

$$|\Delta i_{c0}| \leq 0.15 \text{ pu} \tag{5.13}$$

$$|\Delta \xi_{ic0}| \leq \varepsilon \tag{5.14}$$

$$|\Delta v_{dc}| \leq 0.15 \text{ pu} \tag{5.15}$$

$$\left(\Delta \xi_{pac}^2 + \Delta \xi_{qac}^2\right)^{1/2} \leq \varepsilon \tag{5.16}$$

$$|\Delta w_{\Sigma 0}| \leq 0.5 \text{ pu} \tag{5.17}$$

$$|\Delta\xi_{w\Sigma 0}| \leq \varepsilon \quad \varepsilon = 10^{-5} \tag{5.18}$$

$$\sqrt{\Delta i_{dc1}^2 + \Delta i_{dc2}^2 + \Delta i_{dc3}^2} \leq 0.15 \text{ pu} \tag{5.19}$$

The decentralized optimal linear feedback controller's matrix, responsible for minimizing DC voltage oscillations, exhibits dominant entries that correspond to specific pairs: $v^*_{dc3,4}$ and $\xi_{iacd3,4}$, $v^*_{dc3,4}$ and $\xi_{pac3,4}$, $p^*_{ac1,2,3,4}$ and $\xi_{iacd1,2,3,4}$, $p^*_{ac1,2,3,4}$ and $\xi_{pac1,2,3,3,4}$, and $w^*_{\Sigma 01,2,3,4}$ and $\xi_{pac1,2,3,3,4}$. This result aligns with the decentralized optimal controller matrix's block-diagonal configuration, where the inter-converter entries are zero. Hence, the v_{dc} related eigenvalues are pushed further away from the right half-plane (–238 $\pm$ j 237, –297 $\pm$ j 987, and –298 $\pm$ j 972), leading to a damping ratio of 0.71, 0.29, and 0.29, respectively. Moreover, the worst initial perturbation scenario under the decentralized optimal controller implementation is obtained at the boundary of the state variables' limit thanks to the state variables' decoupled confinement in separate ellipsoids.

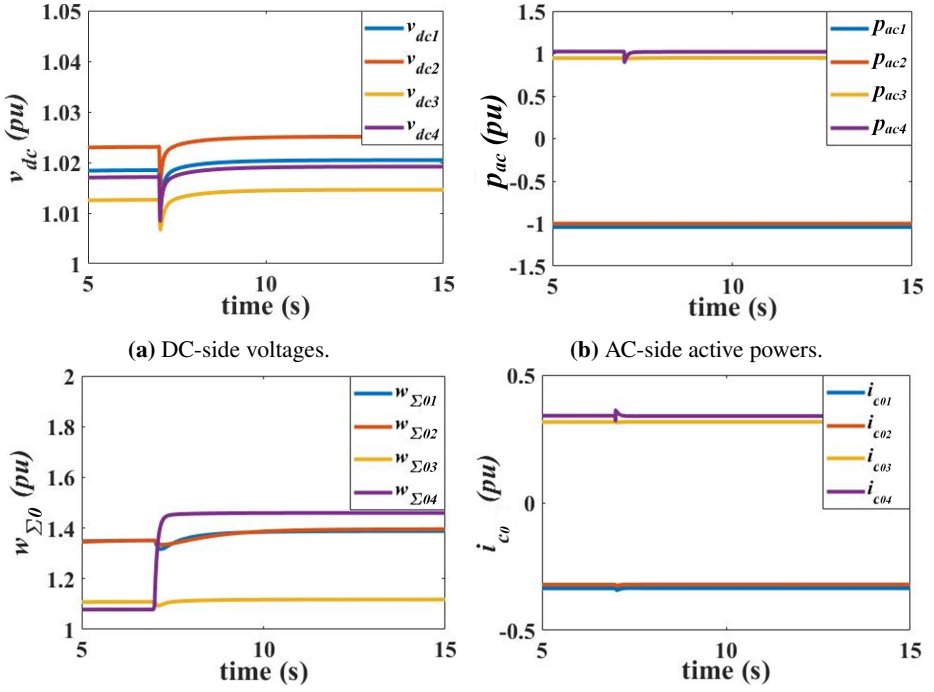

(a) DC-side voltages.

(b) AC-side active powers.

(c) Zero-sequence energy sums.

(d) Zero-sequence circulating currents.

Figure 5.7: MMCs' waveforms after applying a 35% step increase to the MMC4 DC-side voltage at $t = 7$ s: with decentralized optimal linear feedback controller and droop.

Fig. 5.5, 5.6, and 5.7 demonstrate that the centralized optimal controller has stabilized the system by slightly reducing the grid DC-side voltages and increasing

some grid AC-side active powers. This adjustment has caused changes in the converters' zero-sequence energy sum to keep the grid power balanced. On the other hand, the decentralized optimal controller has kept the grid DC-side voltages and AC-side active powers almost constant. Instead, it has varied the converters' zero-sequence energy sum and directed the changes to the arm capacitors to satisfy the grid control inputs' and state variables' limitations. It is important to note that this work does not cover grid power-sharing, which can be managed using secondary grid control.

Case study II: Optimal controller in the absence of the droop control

The droop gain of the grid onshore converters MMC3 and MMC4 is set to zero, so the system becomes unstable with an eigenvalue on the right half-plane ($\lambda = +0.34$). To investigate the optimal controller's ability to handle the droop control task and balance the grid power, a 15% step reduction is applied to p^*_{ac4} at $t = 17\,s$. This scenario is used to estimate the found worst-case perturbation under the centralized optimal controller implementation. The simulation results are shown in Fig. 5.8 and 5.9. Both the centralized and decentralized optimal controllers are able to substitute the droop control function under the steady-state condition and after the system's dynamics and move the system eigenvalues away from the right half-plane. The optimal controller matrix dominant entries in both the centralized and decentralized optimal controllers are associated with the $\xi_{pac1,2,3,4}$ (integral state of the AC-side active powers) and $w^*_{\Sigma 0,1,2,3,4}$ (reference zero-sequence energy sums), and $\xi_{pac1,2,3,4}$ (integral state of the AC-side active powers) and $p^*_{ac1,2,3,4}$ (reference AC-side active powers) pairs, with all the inter-converter entries equal to zero in the decentralized one.

The two methods differed in the role of the converters' zero-sequence energy sum in the decentralized optimal controller. The decentralized optimal controller kept the grid DC-side voltages and AC-side active powers relatively unchanged after the worst initial perturbation scenario by varying the zero-sequence energy sum within the constraints and diverting the variations to the MMC arm capacitors. The relation between the MMC4 zero-sequence energy sum (shown in Fig. 5.9(c)) and the sum of the upper arm capacitor voltages is depicted in Fig. 5.10 as an example. It is assumed that the converter arm capacitors have sufficient capacity to accept such overvoltage under the worst-case perturbation scenario, which could be achieved by either increasing the number of MMC submodules or increasing the voltage rating of the submodule capacitors.

In conclusion, sufficient DC voltage stability margins can be ensured by both the centralized and decentralized optimal linear feedback controllers, as demonstrated by the relocation of the $\lambda_{14,15}$ and $\lambda_{17,18}$ eigenvalues under the worst initial per-

turbation scenario in the absence of the droop controller. It is noteworthy that such stability could not be guaranteed by the droop controller alone. Notably, the addition of the optimal controller in the droop control gain's presence can exploit their synergy and reduce the DC voltage oscillations with larger stability margins. Furthermore, the optimal controller's capability to operate alongside the droop controller may enable its selective activation, i.e., only during worst-case conditions.

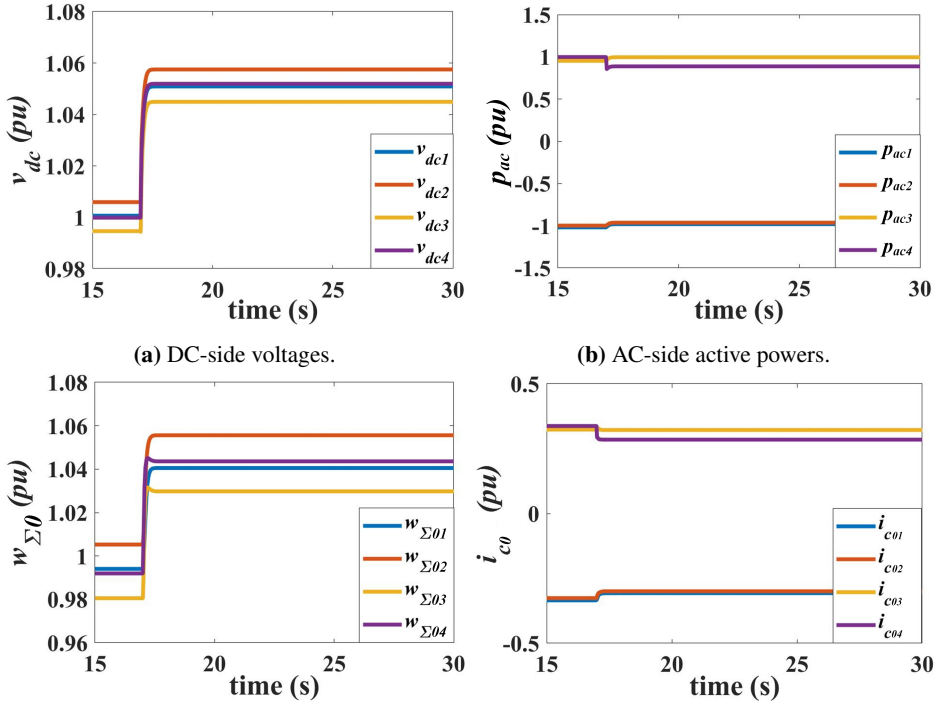

(a) DC-side voltages.

(b) AC-side active powers.

(c) Zero-sequence energy sums.

(d) Zero-sequence circulating currents.

Figure 5.8: MMCs' waveforms after applying a 15% step reduction to the MMC4 AC-side active power at $t = 17$: with centralized optimal linear feedback controller without droop

5.4 Summary and conclusion

This chapter discussed the reduction of the DC voltage oscillations in an offshore four-terminal HVDC grid under the worst-case perturbation scenario using the centralized and decentralized optimal linear feedback controllers. The grid consists of MMCs, and it is observed that the MMC's distinct eigenvalues associated with the zero-sequence circulating current and zero-sequence energy sum

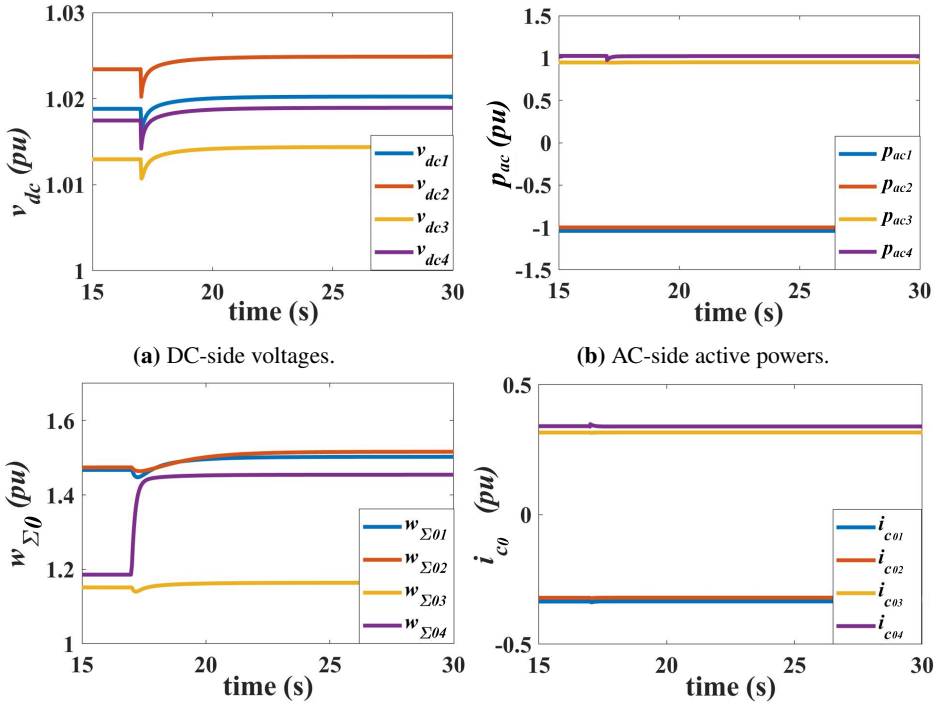

(a) DC-side voltages.

(b) AC-side active powers.

(c) Zero-sequence energy sums.

(d) Zero-sequence circulating currents.

Figure 5.9: MMCs' waveforms after applying a 15% step reduction to the MMC4 AC-side active power at $t = 17$: with decentralized optimal linear feedback controller without droop

state variables and their integral parameters are the closest to the instability region. Therefore, simplified analyses based on 2-level VSCs are not enough for the grid state-space model and stability studies. By tuning the control parameters properly, the stability margins of the MMC state variables can be enhanced.

The eigenvalue stability analysis revealed that the DC voltage oscillations are mainly affected by two eigenvalue pairs, which are associated with the grid DC-side voltage and the integral state of the AC-side active power. These state variables are linked by the droop control gain. The study of the eigenvalue trajectory in response to variations in the droop control gain indicated a trade-off between these two eigenvalue pairs. While the stability margins of one pair improved, the other became more susceptible to instability by moving closer to the right half-plane. Therefore, an optimization strategy to readjust the droop gains can be advantageous in improving the DC voltage stability margins.

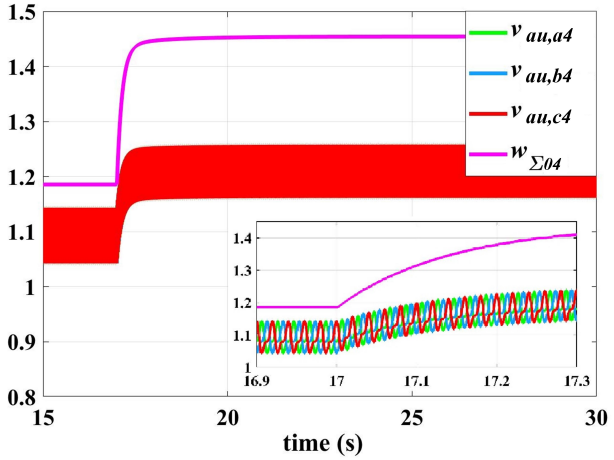

Figure 5.10: MMC4 zero-sequence energy sum and sum of the upper arm capacitor voltages after applying a 15% step reduction to the MMC4 AC-side active power at $t = 17$.

The improvement of DC voltage stability margins under the worst initial perturbation scenario was demonstrated through time-domain simulations using both the centralized and decentralized optimal linear feedback controllers. These controllers can be implemented with or without the droop control gain, with better performance achieved in the presence of the droop control function due to the synergies between the two. The use of the optimal controllers can also inherently satisfy the constraints of the control inputs and state variables, which is not possible with the droop controller alone.

Based on the time-domain simulations, it was observed that there is a noticeable difference in the response of the centralized and decentralized optimal controllers to disturbances. The decentralized optimal controller's performance heavily relies on the control of the zero-sequence energy sum of the converters, which enables it to maintain the DC-side voltage and AC-side active power of the grid relatively constant after the worst-case scenario. This is achieved by directing the perturbations to the arm capacitors of the MMC, resulting in a variation of the converters' zero-sequence energy sum. Consequently, the decentralized optimal controller may require an increased number of MMC sub-modules or higher voltage-rated MMC sub-module capacitors.

The discussion in this chapter is partially supported by the following contributions by the author:

A. Elahidoost and E. Tedeschi, "Control optimization of the offshore HVDC grid based on modular multilevel converter for improving DC voltage stability," *in The*

Renewable Energy & Power Quality Journal (RE&PQJ), vol. 18, no. 273, 2020, pp. 207–212, doi: 10.24084/repqj18.273 [18].

A. Elahidoost, L. Furieri, M. Kamgarpour and E. Tedeschi, "Optimal linear controller for minimizing DC voltage oscillations in MMC-based offshore multiterminal HVDC grids," *in IEEE Access*, vol. 9, pp. 98731-98745, 2021, doi: 10.1109/ACCESS.2021.3096291 [19].

Chapter 6

Decentralized optimal controller for minimizing oscillations in hybrid AC/DC grids

6.1 Introduction

Interconnection and expansion of the AC networks through HVDC grids based on MMCs to form a multiterminal hybrid AC/DC grid can also pose stability issues. These challenges can arise from dynamic interactions between/within AC and DC subgrids due to poorly damped modes that are potential sources of persistent and disruptive oscillations. It has been observed in the previous chapter's small-signal stability analysis that the distinct MMC eigenvalues associated with the zero-sequence circulating current and zero-sequence energy sum state variables and their integral parameters are the closest to the right half-plane and prone to instability. Hence, there is a demand for an optimal controller to ensure the stability of the multiterminal hybrid AC/DC grids under the interconnection and expansion procedure.

On the other hand, it is not uncommon to consider the AC-side of the network as a stiff grid when the main focus of the research is on HVDC grids' stability, leading to neglecting the AC generator and its controls' dynamics and its harmonic interactions with the DC-side of the grid. For instance, [111] proposes a Single-Input-Single-Output (SISO) feedback control model of a hybrid dual-infeed HVDC system to quantitatively investigate the effect of the dynamic interactions between the AC grid strength and control parameters on the stability margins. The goal is to propose a practical design and control methodology for HVDC systems; however,

it demands a number of analyses and extensive retuning. Furthermore, the AC grid is simulated as a voltage source behind series resistance and inductance, and the DC-side voltage and current are assumed to be constant. In [112], an analytical and effective strategy, named the inequality constraints-based method, is introduced to estimate the stability regions of the droop slopes in MMC-based multiterminal HVDC systems. This methodology can further be applied to find the optimal droop control parameters, but the paper only focuses on small disturbance stability at the equilibrium point. Moreover, the AC grid and HVDC cable models are simplified as a stiff grid and T-equivalent circuit, respectively. A control parameter optimization method based on the quadratic index and damping ratio characteristics is proposed in [113] to improve the small-signal stability and dynamic response of a point-to-point hybrid LCC-MMC HVDC system. The methodology is optimal based on the Monte Carlo approach but requires communications among converter stations. The AC grid in this work is represented through a voltage source behind series resistance and inductance, neglecting the generator and its controllers' dynamics. Meanwhile, [114] introduces a methodology for the optimal design of controller parameters to guarantee the small-signal stability of the interconnected MMC-HVDC grids for wind farm integration. The impedance-based analysis approach is used to retune the AC voltage controller optimally, and there are a number of simplifications in grid modeling, including the AC grid represented as a constant power source. The controller parameters' optimization is also investigated in [115] to maximize the phase margin of the MMC-HVDC integrated system, considering the delay effect. An MMC impedance optimization method is proposed that traverses all the potential controllers' parameters' values within the derived boundaries to improve high-frequency stability. Thus, the methodology can be complicated and time-consuming when the number of converter stations increases. Furthermore, the methodology simplifies the AC grid and HVDC cable modeling.

Considering the above discussion, as well as the stability issues and dynamic interactions due to the interconnection and expansion of the MMC-based HVDC grids, it can be concluded that there is a demand for (1) accurate modeling of the multiterminal hybrid AC/DC grids with sufficient details on all components (e.g., the generator and its controllers, MMC and its controller, and HVDC cable) to investigate the control and dynamic interactions between/within the AC and DC subgrids, and (2) an analytical and optimal control methodology to improve the interconnected grid stability and minimize the oscillations caused by the poorly damped modes that are identified from the grid's detailed model. Hence, the goal is to focus on the abovementioned demands to guarantee the stability of the MMC-based multiterminal hybrid AC/DC grids under the worst-case perturbation scenario.

Therefore, this chapter's primary contributions are:

- Investigating the poorly damped modes in an MMC-based multiterminal hybrid AC/DC grid. Such a grid is modeled in detail to account for the multiple sources of oscillations resulting from the dynamic interactions between/ within the AC and DC subgrids. It is shown that the poorly damped modes responsible for oscillations have a high sensitivity to the tuning parameters of the power system stabilizer (PSS) and MMC droop controller on the AC- and DC-side of the grid, respectively. Moreover, it is revealed from the detailed model of the grid that the MMC arm capacitors can contribute to minimizing oscillations arising from the AC-side of the grid. Such a phenomenon would have remained unnoticed if simplified models on either side of the grid were applied.
- Scrutinizing the applicability and feasibility of the decentralized optimal linear feedback controller to improve the stability margins and reduce oscillations under the worst-case perturbation scenario and grid control inputs' and state variables' constraints. These oscillations are primarily caused by the poorly damped modes in MMC-based multiterminal hybrid AC/DC grids. To this end, the performance of the controller is validated under the following cases:
  - worst-case perturbation scenario,
  - small and large disturbances (three-phase short circuit fault),
  - absence or presence of the traditional PSS or MMC droop controller, and
  - uncertainties in control parameters, grid parameters, and operating conditions.

Finally, a comparative analysis between the proposed approach and other relevant literature is presented in Table 6.1:

Table 6.1: Summary of the comparison between the proposed approach and other relevant references.

Ref.	Methodology	A	B	C	D	E	F	G	H	I
Proposed approach	Decentralized optimal linear feedback controller	✓	✓	✓	✓	✓	✓	✓	✓	✓
[80]	DC-side damper structure (impedance-based modeling)	✓	×	✓	×	×	✓	×	×	✓
[81]	Feedback linearization technique	✓	✓	×	×	×	×	×	×	×
[82]	Adaptive PLL controller	✓	✓	×	×	×	×	×	✓	×
[83]	Global MPC-based grid controller	×	✓	×	✓	✓	✓	×	×	×
[84]	Distributed supplementary control	×	✓	✓	×	×	×	×	×	×
[111]	Single input single output (SISO) feedback control model	✓	×	n.a.	n.a.	n.a.	×	✓	×	n.a.
[112]	Inequality constraints-based method for fast estimation of droop-slope stability regions	×	✓	✓	×	✓	×	✓	×	✓
[113]	Control parameter optimization based on quadratic index and damping ratio	✓	✓	×	✓	✓	×	✓	×	×
[114]	Impedance-based optimal design on controller parameters	✓	×	n.a.	n.a.	n.a.	×	✓	×	n.a.
[115]	MMC impedance optimization	✓	×	n.a.	n.a.	n.a.	×	✓	×	n.a.
[14]	Linear feedback controller	×	✓	×	✓	✓	×	×	×	×

A: Analysing control and dynamic interactions

B: Analytical methodology (no retuning or repetitive calculations or dynamic simulations)

C: Decentralized controller

D: Optimal controller (under worst-case perturbation scenario)

E: Under control inputs' and state variables' constraints (inequality constraints)

F: AC-side detailed model (synchronous generator with controllers)

G: Converter detailed model (MMC with controllers)

H: DC-side detailed model (HVDC cable)

I: Discussion on implementation feasibility (communication requirements, scalability)

n.a.: Not applicable/available

6.2 Hybrid AC/DC grid

The system under study is an MMC-based multiterminal hybrid AC/DC grid that is shown in Fig. 6.1. It is a 14-bus system composed of three AC grids interconnected through an MMC-based three-terminal HVDC network. One of the AC grids containing G1 and G4 has two areas that are 50 km apart. Among the three converter stations, MMC1 and MMC3 are controlled via the DC-droop mode, while MMC2 is in power mode control.

In the following sections, the grid's SSTI state-space model is obtained as a prerequisite for implementing the decentralized optimal controller to improve the grid stability. It is also used for analyzing the small-signal eigenvalue stability to identify the grid's poorly damped modes.

6.2.1 State-space model of the AC grid

The AC grid parameters adapted from [58] are given in Table 6.2. The generators are represented based on the detailed sixth-order model equipped with the Automatic Voltage Regulator (AVR) of the simplified excitation system type, Hydro Turbine Governor (HTG) of the HYGOV type, and speed-sensitive PSS [58]. AC loads are considered as constant impedance (Z). Therefore, the state-space representation of the AC grid with the state vector, $\mathbf{x}_G$, and the control input vector, $\mathbf{u}_G$, for every generator can be stated as:

$$\mathbf{x}_G = [\psi_{fd}\ \psi_{1d}\ \psi_{1q}\ \psi_{2q}\ \omega_m\ \delta \\ \gamma_{avr1}\ \gamma_{avr2}\ \gamma_{htg1}\ \gamma_{htg2}\ \gamma_{htg3}\ \gamma_{htg4}\ \gamma_{pss1}\ \gamma_{pss2}]^T \tag{6.1}$$

$$\mathbf{u}_G = [v^*_{avr}\ \omega^*_m]^T \tag{6.2}$$

where ψ_{fd}, ψ_{1d}, ψ_{1q}, and ψ_{2q} are the per-unit fields and *dq*-component rotor flux linkages. The state variables ω_m and δ are the rotor angular velocity and position, respectively. Moreover, γ is associated with the controller's integral state. The superscript * denotes the reference value, and v^*_{avr} and ω^*_m are the AVR reference voltage and HTG reference angular velocity, respectively. It is worth mentioning that the state variables γ_{pss1} and γ_{pss2} are valid for the reference generators G1, G2, and G3, and δ is only a state variable of G4.

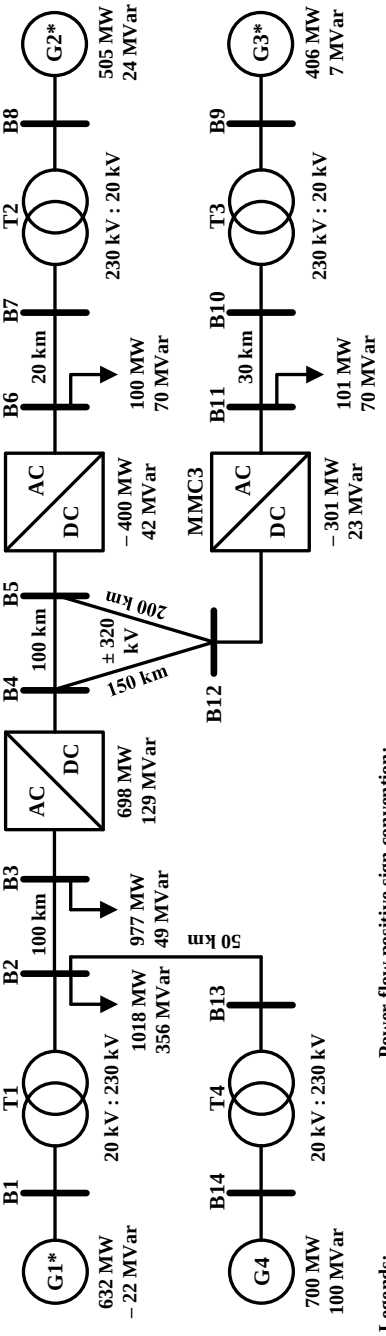

Figure 6.1: Hybrid AC/DC grid under study.

Table 6.2: AC grid parameters.

Synchronous generator			
Parameter	Value	Parameter	Value
S_{rated}	900 MVA	V_{rated}	20 kV
R_a	0.0025 pu	X_l	0.2 pu
X_d	1.8 pu	X_q	1.7 pu
X'_d	0.3 pu	X'_q	0.55 pu
X''_d	0.25 pu	X''_q	0.25 pu
T'_{d0}	8 s	T'_{q0}	0.4 s
T''_{d0}	0.03 s	T''_{q0}	0.05 s
H_{G1}	7 s	H_{G2}	7 s
H_{G3}	6 s	H_{G4}	6 s
Transformer			
Parameter	Value	Parameter	Value
S_{rated}	900 MVA	X_t	0.15 pu
$V_{primary}$	20 kV	$V_{secondary}$	230 kV
AC transmission line			
Parameter	Value	Parameter	Value
S_{rated}	100 MVA	V_{rated}	230 kV
r_l	0.0001 pu/km	x_l	0.001 pu/km

6.2.2 State-space model of the MMC and HVDC cable

The MMC model shown in Fig. 6.2 with parameters [100] given in Table 6.3 is developed based on the simplified average model that is derived from the converter energy-based representation with compensated modulation (CM) (refer to Chapter 3). The derivation of the MMC state-space model is recalled here for the sake of clarity and due to the presence of small differences in formulation with respect to Chapter 3. As mentioned earlier, the CM methodology compensates for the oscillations in the arm capacitor voltages by defining the insertion indices as the ratio of the reference control voltages to the measured or estimated arm capacitor voltages. Hence, the aggregated upper and lower arm capacitor voltages can be assumed to be balanced and represented as:

$$w_{ul} = \frac{1}{2} C_a v_{c,ul}^2 \tag{6.3}$$

where w_{ul} and $v_{c,ul}$ are the aggregated upper (u) or lower (l) arm capacitor energy and voltage ($v_{c,ul} = \sum_{i=1}^{N} v_{sm,ul}$), respectively.

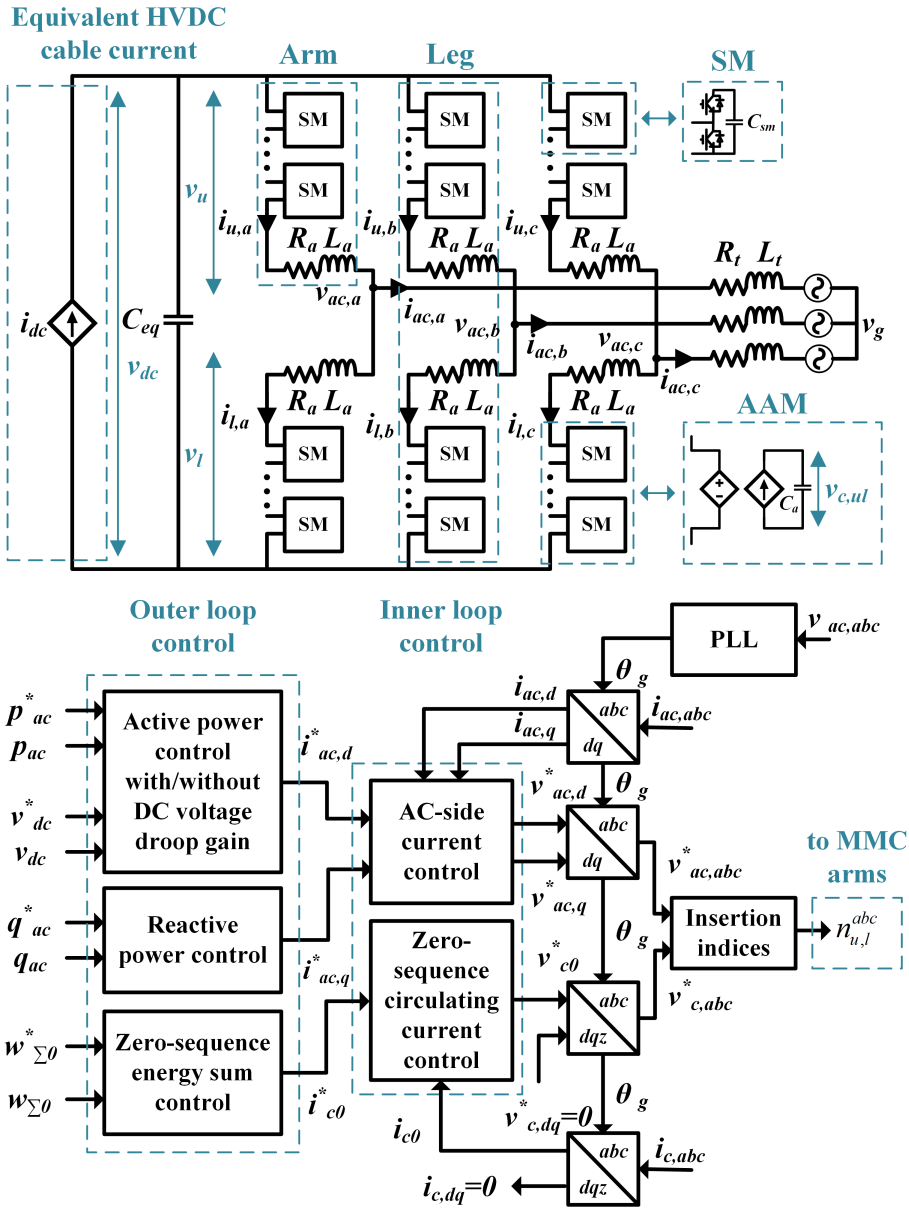

Figure 6.2: MMC topology and control.

Table 6.3: MMC and HVDC cable parameters.

MMC	
Parameter	Value
Base apparent power, S_b	900 MVA
Base DC voltage, V_b^{dc}	640 kV
Converter nominal AC voltage, V_{rated}^{ac}	380 kV
Frequency, ω	$2\pi 50$ rad/s
Arm resistance, R_a	0.885 Ω
Arm inductance, L_a	84.8 mH
Arm capacitance, $C_a = C_{sm}/N$	29.3 μF
Transformer resistance, R_t	1.77 Ω
Transformer reactance, X_t	17.7 Ω
DC link capacitance, C_{eq}	219.74 μF

HVDC cable			
Parameter	Value	Parameter	Value
R_{dc1}	2.65 Ω/km	L_{dc1}	0.6016 mH/km
R_{dc2}	0.1218 Ω/km	L_{dc2}	0.302 mH/km
R_{dc3}	0.016 Ω/km	L_{dc3}	2.8 mH/km
C_{dc}	0.16 μF/km		

Therefore, considering (3.2)-(3.5), the MMC dynamics can be written as:

$$\frac{d}{dt}i_{ac,dq} = \frac{1}{L_{ac}}(v^*_{ac,dq} - v_{g,dq} - R_{ac}i_{ac,dq} - j\omega L_{ac}i_{ac,dq}) \tag{6.4}$$

$$\frac{d}{dt}v_{dc} = \frac{1}{(C_{eq} + \frac{C_{dc}}{2})}(i_{dc} - 3i_c) \tag{6.5}$$

$$\frac{d}{dt}i_c = \frac{1}{L_a}(\frac{v_{dc}}{2} - v^*_c - R_a i_c) \tag{6.6}$$

$$\frac{d}{dt}v_\Sigma = \frac{1}{C_a}(n^*_c i_c - \frac{1}{2}n^*_{ac}i_{ac}) \tag{6.7}$$

where $v_{g,dq}$ is the dq-component of the equivalent AC-side voltage, and v_{dc} and i_{dc} are the DC-side voltage and current, respectively. Moreover, $R_{ac} = R_t + R_a/2$ and $L_{ac} = L_t + L_a/2$. The variable v_Σ is given by $(v_{cu} + v_{cl})/2$. Thus, the reference insertion indices n^*_{ac} and n^*_c can be defined as v^*_{ac}/v_Σ and v^*_c/v_Σ, respectively.

Accordingly, the state-space representation of the MMC with the vectors $\mathbf{x}_{mmc}$ and $\mathbf{u}_{mmc}$, while considering the converter control topology shown in Fig. 6.2,

becomes:

$$\mathbf{x}_{mmc} = [i_{ac,d}\ i_{ac,q}\ v_{dc}\ i_c\ v_\Sigma\ \xi_{iacd}\ \xi_{iacq}\ \xi_{pac}\ \xi_{qac}\ \xi_{ic0}\ \xi_{w\Sigma 0}\ \xi_{pll}\ \Theta_g]^T \tag{6.8}$$

$$\mathbf{u}_{mmc} = [v^*_{dc}\ p^*_{ac}\ q^*_{ac}\ w^*_{\Sigma 0}]^T \tag{6.9}$$

where p_{ac} and q_{ac} are the AC-side active and reactive powers, respectively. Additionally, $w_{\Sigma 0}$ is the zero-sequence energy sum that can be calculated as $w_{\Sigma 0} = w_u + w_l = \frac{1}{2}C_a(v^2_{cu} + v^2_{cl})$. The MMC control architecture (shown in Fig. 6.2) is based on the conventional cascaded inner and outer control loops with PI controllers that are tuned using the modulus and symmetrical optimum techniques (refer to Appendix A) [116]. The variable ξ is related to the PI controllers' integral state, and Θ_g is the measured AC grid voltage angle detected by a phase-locked loop (PLL).

The HVDC cable with parameters given in Table 6.3 is represented based on the frequency-dependent model with one pi-section and three parallel series branches [59]. Hence, the state-space representation for every HVDC cable contains three current states as follows:

$$\mathbf{x}_C = [i_{dc1}\ i_{dc2}\ i_{dc3}]^T \tag{6.10}$$

It is worth mentioning that the effect of the cable shunt capacitance is considered in (6.5).

6.3 Decentralized optimal controller problem formulation

The decentralized problem formulation introduced in Chapter 4 is repeated here for quick reference. The goal of the oscillation index, J_{osci}, is to minimize the fluctuations caused by the poorly damped modes via the optimal controller, $\mathbf{K}$, under the worst-case perturbation scenario:

$$J_{osci} = \min_{\mathbf{K}} \max_{\mathbf{x}(0)\in\mathbb{X}_\mathbf{0}} \int_0^\infty \mathbf{z}(t)^T\mathbf{z}(t)\,dt \tag{6.11}$$

$$s.t. \quad \dot{\mathbf{x}}(t) = \mathbf{A}\mathbf{x}(t) + \mathbf{B}\mathbf{u}(t) \tag{6.12}$$

$$\mathbf{z}(t) = \mathbf{C}\mathbf{x}(t) \tag{6.13}$$

$$\mathbf{u}(t) = \mathbf{K}\mathbf{x}(t) \tag{6.14}$$

where (4.1) is subject to:

$$\mathbf{x}(0) \in \mathbb{X}_0 = \{\mathbf{x}_i \in \mathbb{R}^{n_i} \ : \forall i \in \mathbb{Z}_{[1,r]}\ \mathbf{x}_i^T \mathbf{E}_\mathbf{x}{}^i \mathbf{x}_i \leq 1\} \tag{6.15}$$

$$\mathbf{u}(t) \in \mathbb{U} \ = \{\mathbf{u}_j \in \mathbb{R}^{m_j} \colon \forall j \in \mathbb{Z}_{[1,q]}\ \mathbf{u}_j^T \mathbf{E}_\mathbf{u}{}^j \mathbf{u}_j \leq 1\} \tag{6.16}$$

The signals of interest, $\mathbf{z}(t)$, whose oscillations should be minimized, are state variables linked to the poorly damped modes associated with either AC- or DC-side of the grid. In the following section, the small-signal eigenvalue stability and participation factor analysis are performed to idenitfy the most dominant modes with the lowest damping ratios and their corresponding participating state variables to minimize their oscillations. Matrices $\mathbf{A} \in \mathbb{R}^{99\times 99}$ and $\mathbf{B} \in \mathbb{R}^{99\times 19}$ are the grid state-space matrices found according to the grid overall state variables, $\mathbf{x}$, and control inputs, $\mathbf{u}$:

$$\mathbf{x} = [\mathbf{x}_{G1}^T\ \mathbf{x}_{G4}^T\ \mathbf{x}_{mmc1}^T\ \mathbf{x}_{C12}^T\ \mathbf{x}_{G2}^T\ \mathbf{x}_{mmc2}^T\ \mathbf{x}_{C23}^T\ \mathbf{x}_{G3}^T\ \mathbf{x}_{mmc3}^T\ \mathbf{x}_{C13}^T]^T \tag{6.17}$$

$$\mathbf{u} = [\mathbf{u}_{G1}^T\ \mathbf{u}_{G4}^T\ \mathbf{u}_{mmc1}^T\ \mathbf{u}_{G2}^T\ \mathbf{u}_{mmc2}^T\ \mathbf{u}_{G3}^T\ \mathbf{u}_{mmc3}^T]^T \tag{6.18}$$

The decentralized optimal linear feedback controller, $\mathbf{K}$, architecture, and implementation (6.14) are depicted in Fig. 6.3. As can be seen from the figure, the decentralized optimal controller is block-diagonal with three separate control zones to avoid the necessity for communication among converter stations over long distances. Namely, the state variables' variations (Δx_i), which can be measured or estimated through wide-area measurement systems, are sent to their associated optimal controller block ($\mathbf{K1}$, $\mathbf{K2}$, or $\mathbf{K3}$), and the resultant reference inputs' variations of the generators and MMCs control loops (Δu_j^*) are transferred only to their corresponding control zones (Zone1, Zone2, or Zone3).

The optimization objective (6.11) is subject to decoupled ellipsoidal constraints on the state variables (6.15) and control inputs (6.16), which are defined using the symmetric positive definite matrices ${\mathbf{E}_\mathbf{x}}^i > 0$ and ${\mathbf{E}_\mathbf{u}}^j > 0$. Accordingly, r and q are the total number of the ellipsoidal constraints on the state variables and control inputs, respectively ($r = 10$ and $q = 16$). Thus, $\sum_{i=1}^{r} n_i = n$, and $\sum_{j=1}^{q} m_j = m$. Namely, the decentralized optimal controller, $\mathbf{K}$, aims to minimize the maximum possible amount of the oscillations under the worst-case perturbation scenario found under the small-signal approximations defined by (6.15) and (6.16). The feasibility of implementing decoupled constraints on the state variables and control inputs improves the optimal controller flexibility based on the design requirements.

For instance, the decoupled ellipsoidal constraints on the state variables (6.16) of the hybrid AC/DC grid, which are defined according to Fig. 6.3(a), are such that a 10% limit is applied on the square root of the sum of the squares of the disturbances for every piece of grid equipment (every generator, MMC, and HVDC cable such that $r = 10$), describing the search area for the expected worst-case perturbation scenario:

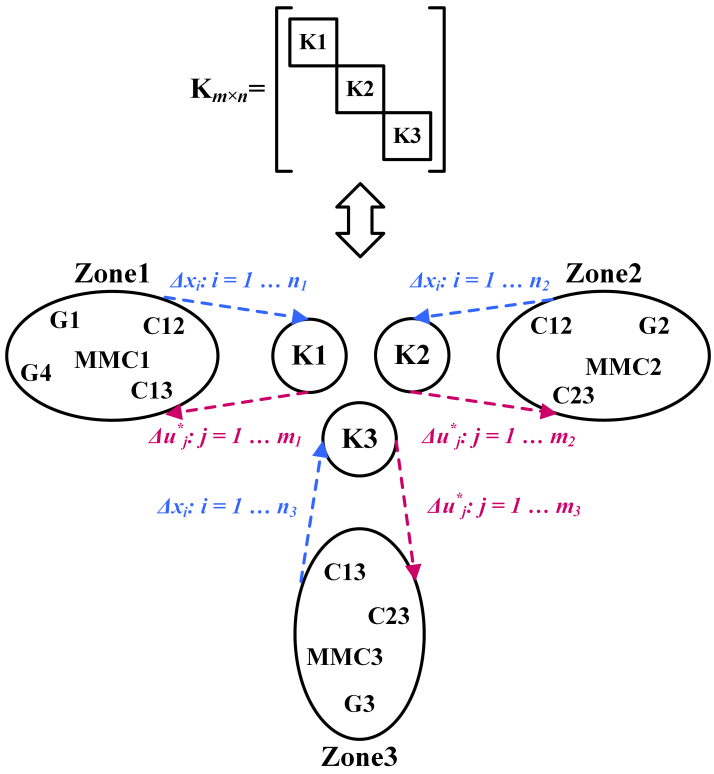

(a) Decentralized (block-diagonal) optimal controller architecture.

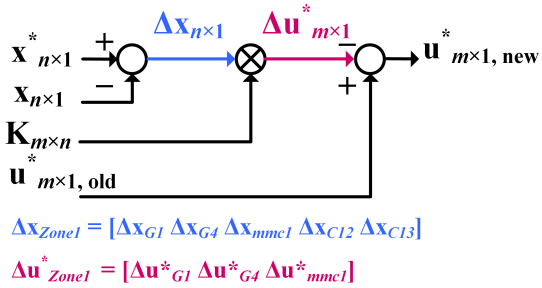

(b) Decentralized optimal controller implementation.

Figure 6.3: Decentralized optimal linear feedback controller architecture and implementation.

$$\Big(\Delta\psi_{fd}^2+\Delta\psi_{1d}^2+\Delta\psi_{1q}^2+\Delta\psi_{2q}^2+\Delta\omega_m^2+\Delta\delta^2+ \\ \Delta\gamma_{avr1}^2+\Delta\gamma_{avr2}^2+\Delta\gamma_{htg1}^2+\Delta\gamma_{htg2}^2+\Delta\gamma_{htg3}+ \\ \Delta\gamma_{htg4}^2+\Delta\gamma_{pss1}^2+\Delta\gamma_{pss2}^2\Big)^{1/2}\leq 0.1 \text{ pu} \tag{6.19}$$

$$\Big(\Delta i_{ac,d}^2+\Delta i_{ac,q}^2+\Delta v_{dc}^2+\Delta i_c^2+\Delta v_\Sigma^2+ \\ \Delta\xi_{iacd}^2+\Delta\xi_{iacq}^2+\Delta\xi_{pac}^2+\Delta\xi_{qac}^2+\Delta\xi_{ic0}^2+ \\ \Delta\xi_{w\Sigma 0}^2+\Delta\xi_{pll}^2+\Delta\Theta_g^2\Big)^{1/2}\leq 0.1 \text{ pu} \tag{6.20}$$

$$\Big(\Delta i_{dc1}^2+\Delta i_{dc2}^2+\Delta i_{dc3}^2\Big)^{1/2}\leq 0.1 \text{ pu} \tag{6.21}$$

Hence, (6.19)-(6.21) resulted from (6.16) and are associated with the decoupled ellipsoidal constraints on every generator, MMC, and HVDC cable, respectively. The 0.1 pu can be implemented in the optimization problem formulation by defining the symmetric positive definite matrices ${\mathbf{E_x}}^i$ as diagonal with all their entries equal to 100. Note that these decoupled ellipsoidal constraints, which impose a variation limit for a group of state variables, can be modified and grouped differently based on the prescriptions of the relevant grid codes and standards.

On the other hand, the decoupled ellipsoidal constraints on the control inputs' variations for every generator and MMC, resulting in $q = 16$, are defined as follows:

$$|\Delta v_{avr}^*|\leq 1 \text{ pu} \tag{6.22}$$

$$|\Delta\omega_m^*|\ \leq 1 \text{ pu} \tag{6.23}$$

$$|\Delta v_{dc}^*|\ \leq 1 \text{ pu} \tag{6.24}$$

$$\Big((\Delta p_{ac}^*)^2+(\Delta q_{ac}^*)^2\Big)^{1/2}\leq 1 \text{ pu} \tag{6.25}$$

$$|\Delta w_{\Sigma 0}^*|\leq 1 \text{ pu} \tag{6.26}$$

The 1 pu variation limit is selected to allow a high degree of freedom to the decentralized optimal controller to readjust the control inputs to reduce the oscillations caused by the poorly damped modes. Accordingly, the symmetric positive definite matrices ${\mathbf{E_u}}^j$ are defined as diagonal matrices with all their entries equal to 1.

Since the above optimization problem (6.11)-(6.16) is non-convex in its objective and constraints, obtaining its optimal solution is not straightforward. However, as shown in Chapter 4, it is possible to approximate it as a convex SDP problem using the Lyapunov stability and LMI theories. Hence, the decentralized optimal

controller problem formulation, (4.27)-(4.33), can be solved using the YALMIP optimization toolbox [101] of MATLAB in conjunction with the MOSEK solver [102] that is an interior-point optimizer for linear, quadratic, and conic problems.

6.4 Small-signal eigenvalue stability analysis

The small-signal eigenvalue stability analysis is carried out for the MMC-based multiterminal hybrid AC/DC grid to serve three primary purposes: first, to gain a better insight into the grid stability and dynamics; second, to find the grid's poorly damped modes; and third, to evaluate the decentralized optimal controller's performance to improve the damping ratio of the poorly damped modes and grid stability margins.

The state-space model of the grid obtained in the previous section is linearized around the operating point depicted by the power flow condition in Fig. 6.1. Hence, the matrices $\mathbf{A}_{99\times 99}$ and $\mathbf{B}_{99\times 19}$ that are among the inputs of the optimization procedure are obtained. Time-domain verification is used to validate the accuracy of the linearized model by comparing it with the circuit-based (component-based) model developed in MATLAB/Simulink via the Simscape toolbox. The results are shown in Fig. 6.4. A 1% step increase is applied to G1 reference rotor angular velocity at $t = 1$, and ω_m waveforms of the generators are given in Fig. 6.4(a). Next, Fig. 6.4(b) demonstrates the MMC arm capacitor voltages after a 10% step increase of p^*_{ac1} at $t = 1$. The simulation results show that the two models match pretty well, and the linearized model can accurately represent the grid dynamics under the transients.

Two pairs of poorly-damped modes are identified through the small-signal eigenvalue stability analysis as given in Table 6.4. The first pair, $\lambda_{1,2}$, is defined as an electromechanical mode since its damping ratio is less than 5%, and its frequency is in the range of 0.2-2 Hz. Participation factor analysis demonstrates that the state variables δ_4, w_{m1}, and w_{m4}, which are associated with G1 and G4, are the main contributors to this mode. Thus, Fig. 6.5 indicates the relative observability of this mode in rotor angular velocity state variables of the generators when $\lambda_{1,2}$ is excited. It is evident from the figure that $\lambda_{1,2}$ is an inter-area mode with G1 and G4 oscillating against each other. On the other hand, the second pair of the poorly damped modes, $\lambda_{3,4}$, with a damping ratio of 14%, is mainly affected by the MMC state variables $v_{\Sigma 2}$, $v_{\Sigma 1}$, $v_{\Sigma 3}$, $\xi_{w\Sigma 02}$, $\xi_{w\Sigma 01}$, and $\xi_{w\Sigma 03}$. This eigenvalue pair is categorized as a poorly damped mode since it has a low damping ratio as well as a high sensitivity to parametric variations, as shown in Fig. 6.6(b). That is, $\lambda_{1,2}$ is primarily influenced by the state variables on the generator-side of the grid, whereas the converter side state variables are responsible for $\lambda_{3,4}$ properties.

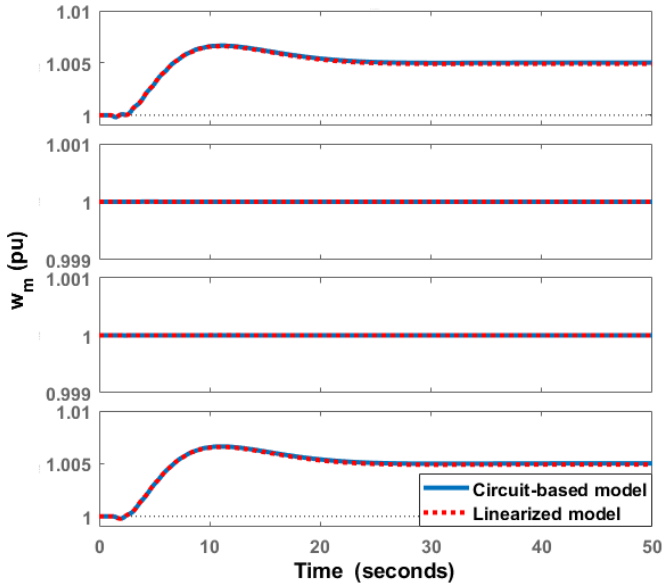

(a) Rotor angular velocity, w_m, of the generators G1, G2, G3, and G4 (from top to bottom).

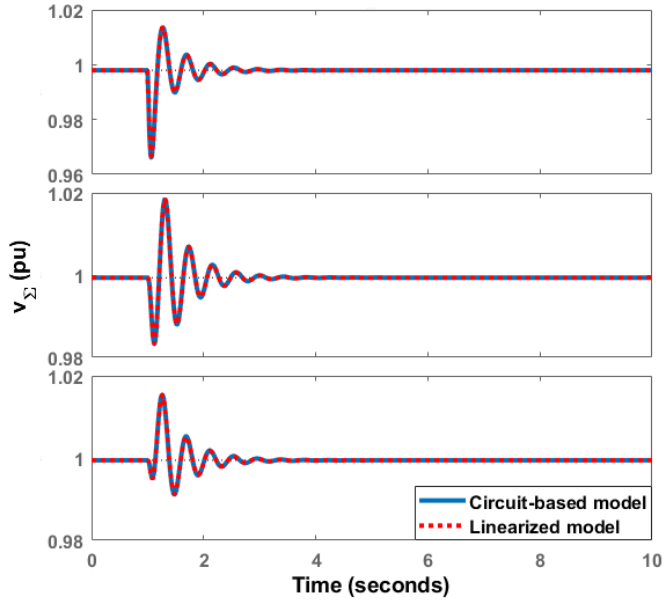

(b) Arm capacitor voltage, v_Σ, of the converters MMC1, MMC2, and MMC3 (from top to bottom).

Figure 6.4: Time-domain verification of the circuit-based model and linearized model of the MMC-based hybrid AC/DC study grid: (a) After applying a 1% step increase to G1 reference rotor angular velocity at $t = 1\ s$, and (b) after applying a 10% step increase to MMC1 reference active power at $t = 1\ s$.

Table 6.4: Poorly damped eigenvalues and their primary participating states.

MMC-based hybrid AC/DC grid under study				
No.	Eigenvalue (mode)	Damping ratio (%)	Frequency (Hz)	Main participating states*
$\lambda_{1,2}$	$-0.27 \pm j\ 5.46$	5	0.87	δ_4, w_{m1}, w_{m4}
$\lambda_{3,4}$	$-2.13 \pm j\ 14.89$	14	2.37	$v_{\Sigma 2}$, $v_{\Sigma 1}$, $v_{\Sigma 3}$, $\xi_{w\Sigma 02}$, $\xi_{w\Sigma 01}$, $\xi_{w\Sigma 03}$
After addition of the decentralized optimal controller				
No.	Eigenvalue (mode)	Damping ratio (%)	Frequency (Hz)	Main participating states*
$\lambda_{1,2}$	$-0.67 \pm j\ 5.69$	11.7	0.91	δ_4, w_{m1}, w_{m4}
$\lambda_{3,4}$	$-10.54 \pm j\ 15.31$	56.7	2.44	$v_{\Sigma 2}$, $v_{\Sigma 1}$, $v_{\Sigma 3}$, $\xi_{w\Sigma 02}$, $\xi_{w\Sigma 01}$, $\xi_{w\Sigma 03}$

* indices 1, 2, 3, and 4 refer to generator G1, G2, G3, or G4 or converter MMC1, MMC2, or MMC3.

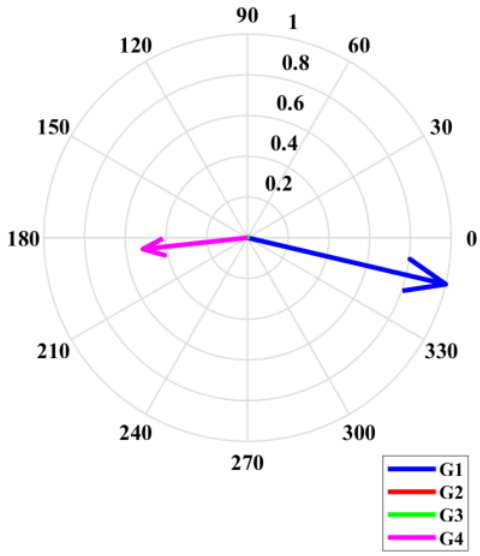

Figure 6.5: Observability (mode shape) of $\lambda_{1,2}$ in rotor angular velocity states of the generators.

Eigenvalue trajectory analysis is performed to investigate the sensitivity of the poorly damped modes to control parameters. It is found that $\lambda_{1,2}$ are very sensitive to PSS1 gain while the droop coefficient plays a pivotal role in $\lambda_{3,4}$ characteristics. As is apparent from Fig. 6.6(a), by increasing the PSS1 gain from 0.001 to 100, the system becomes unstable since $\lambda_{1,2}$ move toward the right half-plane. Similarly, the stability margins of $\lambda_{3,4}$ reduce as the MMC1 droop coefficient increases from 0.05 to 1 as presented in Fig. 6.6(b).

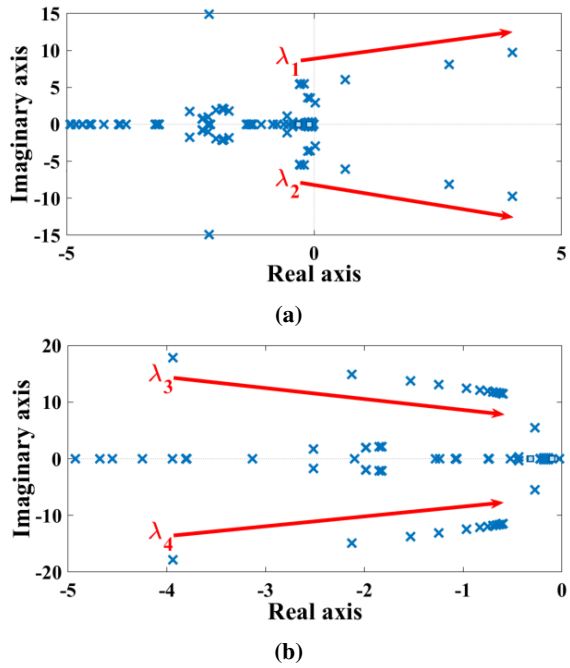

Figure 6.6: Eigenvalue trajectory for: (a) PSS1 gain variation from 0.001 to 100 (b) MMC1 droop variation from 0.05 to 1.

Now that the poorly damped modes and their corresponding state variables are identified, the decentralized optimal controller can be formulated such that:

$$\mathbf{z} = [w_{m1}\ w_{m4}\ \delta_4\ v_{\Sigma 1}\ w_{m2}\ v_{\Sigma 2}\ w_{m3}\ v_{\Sigma 3}]^T \tag{6.27}$$

Therefore, the optimization objective is to minimize the oscillations corresponding to the output vector's state variables, $\mathbf{z}$, under the worst-case perturbation scenario, to improve the damping ratios and stability margins of the poorly damped modes, $\lambda_{1,2}$ and $\lambda_{3,4}$. Hence, the matrix $\mathbf{C}_{99\times 99}$ from (6.13) can be described as diagonal with weights on the entries corresponding to the state variables of the matrix $\mathbf{z}$. Namely, the worst-case perturbation scenario that is defined under the optimization constraints (6.15) and (6.16) yields the maximum oscillations associated with the state variables (6.27), which belong to both the AC- and DC-side of the grid. The effect of the decentralized optimal controller on the poorly damped modes is summarized in Table 6.4. Evidently, $\lambda_{1,2}$ has moved from -0.27 to -0.67 with a slight change of frequency, which has improved the damping ratio from 5% to 11.7% (2.34 times). Likewise, the damping ratio of $\lambda_{3,4}$ has increased by a factor of 4.05 (from 14% to 56.7%), and the mode has further moved to the left from -2.13 to -10.54 (4.94 times).

6.5 Time-domain simulations

In this section, time-domain simulations are performed in MATLAB/Simulink to investigate the applicability of the decentralized optimal controller under four different case studies. Its performance is compared with the PSS and MMC droop controller, representing the state-of-the-art solutions for the considered application, since the poorly damped modes, $\lambda_{1,2}$ and $\lambda_{3,4}$, are highly sensitive to these two controllers' tuning parameters, as shown in the previous section. In the first case study, generator and converter control inputs are perturbed under different scenarios to evaluate the optimal controller performance under small disturbances. In the second case, the worst-case perturbation scenario found under the optimization constraints is simulated, as the optimal controller performance has never been tested when the exact worst-case condition is modeled. Then, in the third one, a three-phase short circuit, which is the worst type of fault in these systems [117], is applied on the AC-side of the grid to explore the optimal controller performance under large disturbances. Finally, the fourth test evaluates the optimal controller robustness against uncertainties in control and grid parameters and operating conditions.

6.5.1 Case study I: Perturbations

The purpose of this study is to evaluate the dynamic behavior of the decentralized optimal controller when it is subject to perturbations (small disturbances) on the generator side (exciting the mode $\lambda_{1,2}$) or converter side of the grid (exciting the mode $\lambda_{3,4}$). To this end, the optimal controller performance is analyzed when it is implemented into the grid operating under the conditions explained in Section 6.2, together with scenarios where the PSS or droop controller is deactivated:

Perturbations on the generator side:

First, a 2% step increase is applied at $t = 10\ s$ to G1 reference rotor angular velocity, ω^*_{m1}, which is the reference input to the HTG1 and PSS1. Simulation results are depicted in Fig. 6.7. It is apparent from the figure that when the decentralized optimal controller is implemented, either in the presence or absence of the PSS1, it is capable of limiting the ω_{m1} and δ_4 variations to a great extent, improving the damping of the mode $\lambda_{1,2}$. The controller achieves this by exploiting the converter storage capacity through slightly increasing the $v_{\Sigma 1}$ (0.04%), which results in the slight reduction of the MMC1 active power by 1.5%. In the absence of the decentralized optimal controller and when the PSS1 is active, the 2% step increase of the ω^*_{m1} results in a considerable decrease of the δ_4 and $i_{ac,d1}$, which substantially reduces the amount of active power delivered to the MMC1 (-15%). It should be noted that under this condition, the δ_4 and $i_{ac,d1}$ settle at new operating points after

approximately 170 s and 110 s, respectively.

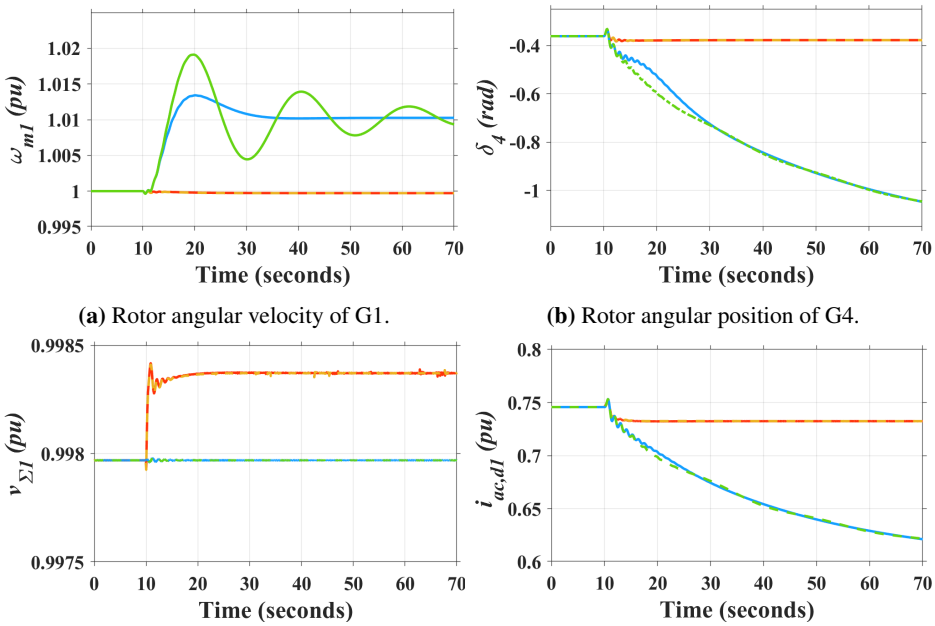

(a) Rotor angular velocity of G1.

(b) Rotor angular position of G4.

(c) Arm capacitor voltage of MMC1.

(d) AC-side current of MMC1.

Figure 6.7: Decentralized optimal controller performance after applying a 2% step increase to G1 reference rotor angular velocity at $t = 10\ s$: (yellow) with decentralized optimal controller only, (blue) with PSS1 only, (red) with both decentralized optimal controller and PSS1, and (green) without both decentralized optimal controller and PSS1.

Second, the G1 reference AVR voltage, v^*_{avr1}, is increased by 20% at $t = 10\ s$, and the results are shown in Fig. 6.8. It is apparent from the figure that the ω_{m1} and δ_4 settling time is much shorter in the presence of the decentralized optimal controller than in its absence, and their oscillations are better damped. This fast response is obtained at the cost of a 0.3% decrease of the MMC1 arm capacitor voltage and an 11% increase of the MMC1 d-component current. When both the decentralized optimal controller and PSS1 are deactivated, the waveforms contain oscillations, and the grid eventually becomes unstable after about 110 s.

Overall, it can be observed that when the perturbations occur on the generator side of the grid (exciting the mode $\lambda_{1,2}$), the decentralized optimal controller can operate even in the absence of the PSS1. Further, it can take up the PSS role in damping the oscillations more effectively and quickly by manipulating the converter storage capacity. Notably, the optimal controller performance is not dependent on the

PSS1. Even if the PSS is absent or poorly tuned, the optimal controller can guarantee grid stability when the poorly damped electromechanical modes are excited.

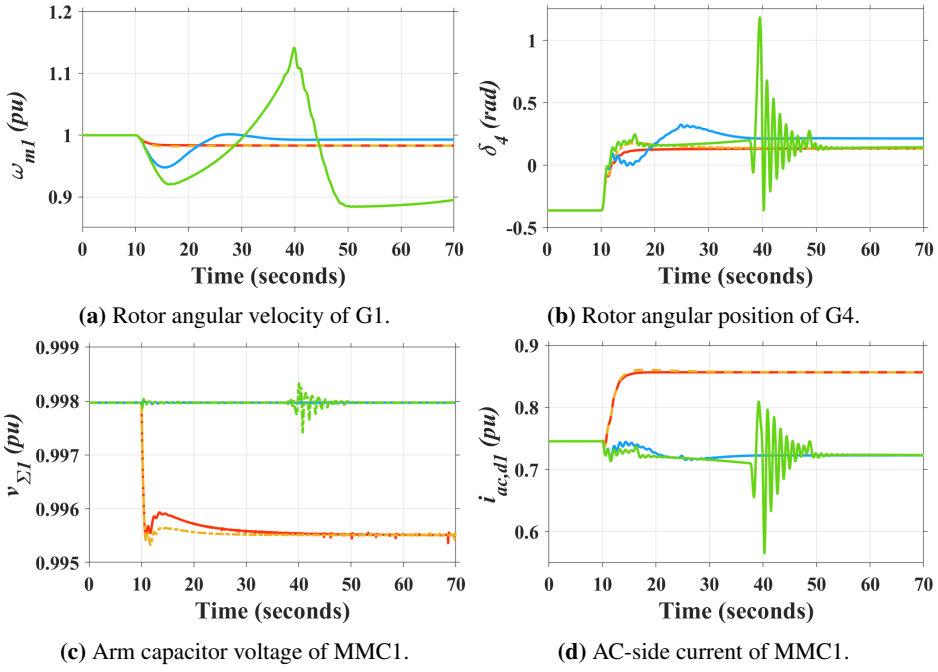

(a) Rotor angular velocity of G1.

(b) Rotor angular position of G4.

(c) Arm capacitor voltage of MMC1.

(d) AC-side current of MMC1.

Figure 6.8: Decentralized optimal controller performance after applying a 20% step increase to G1 reference AVR voltage at $t = 10\ s$: (yellow) with decentralized optimal controller only, (blue) with PSS1 only, (red) with both decentralized optimal controller and PSS1, and (green) without both decentralized optimal controller and PSS1.

Perturbations on the converter side:

First, a 20% step increase is applied to the MMC1 reference AC-side active power, p^*_{ac1}, at $t = 10\ s$ to excite the mode $\lambda_{3,4}$. According to Fig. 6.9, the grid becomes unstable if there is no droop or decentralized optimal controller. The simulation results for the other scenarios are demonstrated in Fig. 6.10. When there is only MMC1 droop control gain of 0.1 without the decentralized optimal controller, waveforms contain a high amount of oscillations at the frequency related to the mode $\lambda_{3,4}$, and the perturbation of p^*_{ac1} results in the δ_4 on the generator side varying from -0.36 to -0.38 rad. In the scenario with the decentralized optimal controller and droop, the oscillations are significantly reduced, and there is almost no oscillation when the optimal controller is operating without any droop controller on MMC1.

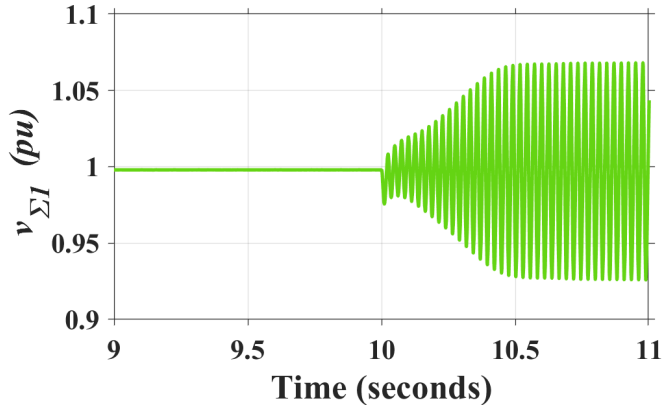

Figure 6.9: MMC1 arm capacitor voltage after applying a 20% step increase to MMC1 reference AC-side active power at $t = 10\ s$ when MMC1 droop control is deactivated.

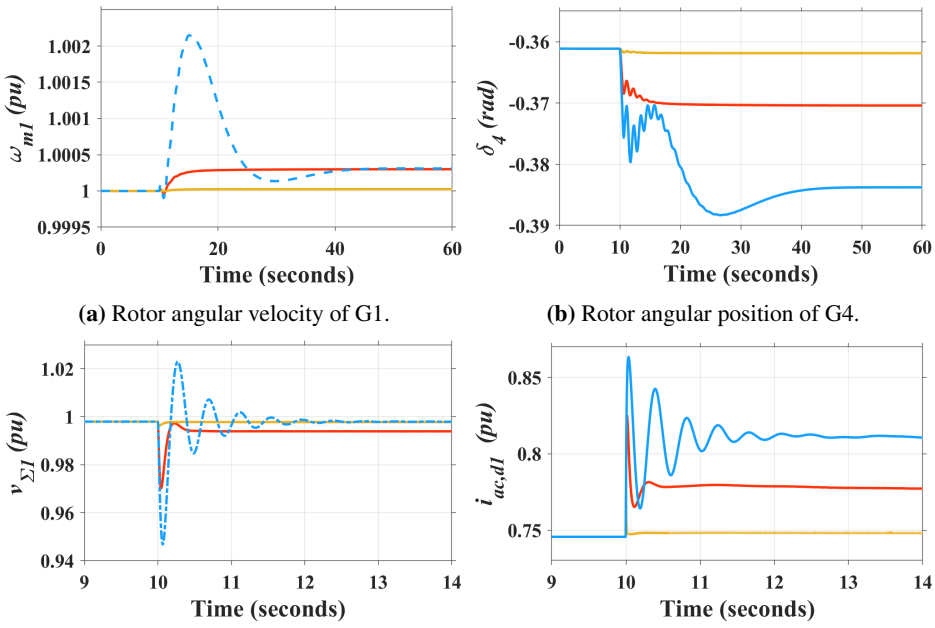

(a) Rotor angular velocity of G1.

(b) Rotor angular position of G4.

(c) Arm capacitor voltage of MMC1.

(d) AC-side current of MMC1.

Figure 6.10: Decentralized optimal controller performance after applying a 20% step increase to MMC1 reference AC-side active power at $t = 10\ s$: (yellow) with decentralized optimal controller only, (blue) with MMC1 droop only, (red) with both decentralized optimal controller and MMC1 droop.

Second, the MMC1 reference zero-sequence energy sum, $w^*_{\Sigma 01}$, is increased by 20% at $t = 10\,s$, and the grid becomes unstable in the absence of the decentralized optimal controller and droop controller on MMC1. The results are given in Fig. 6.11. As shown in the figure, waveforms fluctuate considerably at the frequency related to the mode $\lambda_{3,4}$ under the droop controller alone, and the oscillations decrease significantly when the decentralized optimal controller is operating either alone or together with the droop controller on MMC1.

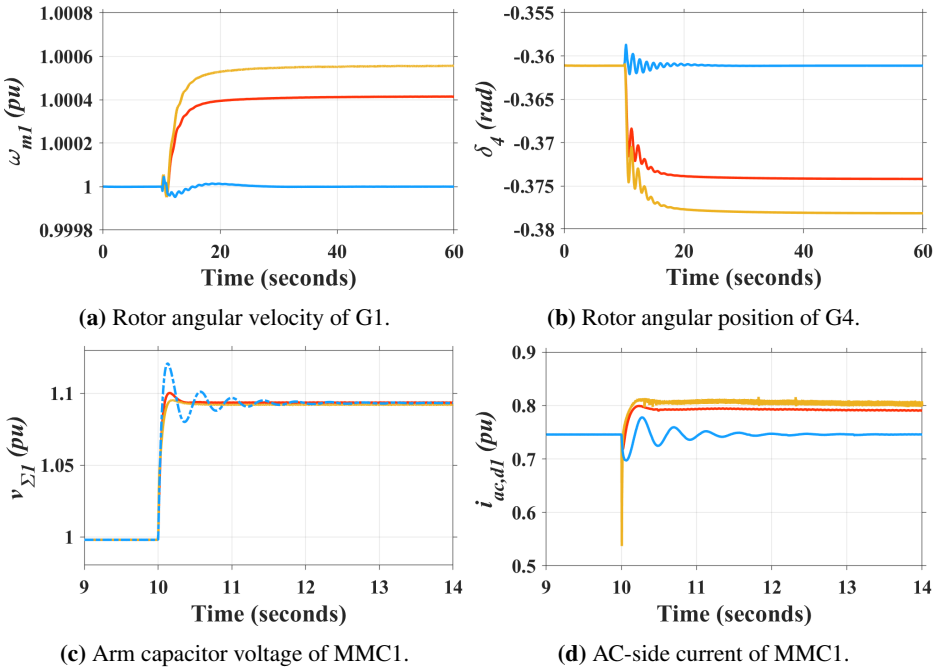

(a) Rotor angular velocity of G1.

(b) Rotor angular position of G4.

(c) Arm capacitor voltage of MMC1.

(d) AC-side current of MMC1.

Figure 6.11: Decentralized optimal controller performance after applying a 20% step increase to MMC1 reference zero-sequence energy sum at $t = 10\,s$: (yellow) with decentralized optimal controller only, (blue) with MMC1 droop only, (red) with both decentralized optimal controller and MMC1 droop.

Therefore, the decentralized optimal controller can efficiently damp the oscillations caused by the small perturbations on the converter side of the grid (exciting the mode $\lambda_{3,4}$), whether the droop controller on the MMC1 is active or not. The optimal controller is not sensitive to the droop controller gain, which is an advantage in the case of poor tuning of the droop controllers in multiterminal configurations.

6.5.2 Case study II: Worst-case perturbation scenario

In this study, the performance of the decentralized optimal controller is tested for the first time against the worst-case perturbation scenario obtained from the optimization procedure. The worst-case perturbation is found under the constraints defined in (6.15), (6.16), (6.19)-(6.21), and (6.22)-(6.26). Table 6.5 depicts the primary control inputs' variations ($\geq 20\%$), which are associated with the worst-case perturbation scenario, $\mathbf{x}_{0,worst}$. Simulation results are shown in Fig. 6.12. Without the decentralized optimal controller, and in the presence of PSS and MMC droop controller, the grid becomes unstable (see Fig. 6.12(d) at $t = 16\ s$.) under the worst-case perturbation scenario while the oscillations are within the frequency range related to the mode $\lambda_{1,2}$ (see Fig. 6.12(c) and Fig. 6.12(d)). On the other hand, the decentralized optimal controller (in the presence of PSS and MMC droop controller) can keep the system stable and damp the oscillations such that the grid waveforms settle at a new operating point. It is worth mentioning that the grid power-sharing control is out of the scope of this work, and it can further be managed by the grid's secondary controller at a higher level.

Consequently, the decentralized optimal controller can ensure the grid's stability under a higher range of dynamics and transients than the conventional grid controllers. Moreover, the optimal controller's applicability is validated under the condition claimed by the optimization results.

Table 6.5: Primary control inputs' variations ($\geq 20\%$) associated with the worst-case perturbation scenario, $\mathbf{x}_{0,worst}$.

Control input	Variation	Control input	Variation
Δv^*_{avr1}	0.2	Δq^*_{ac1}	0.57
$\Delta \omega^*_{m1}$	0.4	Δv^*_{avr2}	0.3
Δv^*_{avr4}	0.67	Δq^*_{ac2}	0.36
$\Delta \omega^*_{m4}$	0.28	$\Delta w^*_{\Sigma 02}$	-0.44

* indices 1, 2, 3, and 4 refer to generator G1, G2, G3, or G4 or converter MMC1, MMC2, or MMC3.

6.5.3 Case study III: Three-phase short circuit fault

In this section, the optimal controller performance under a large disturbance is investigated, although this is beyond the optimization scope based on the small-signal approximation. A three-phase short circuit fault is applied at bus B2 at $t = 10\ s$ and cleared after 500 ms. The fault is used to excite the inter-area mode $\lambda_{1,2}$ on the AC-side of the grid. The time-domain simulation results are demonstrated in Fig. 6.13. The figure shows that the ω_{m1} and δ_4 waveforms,

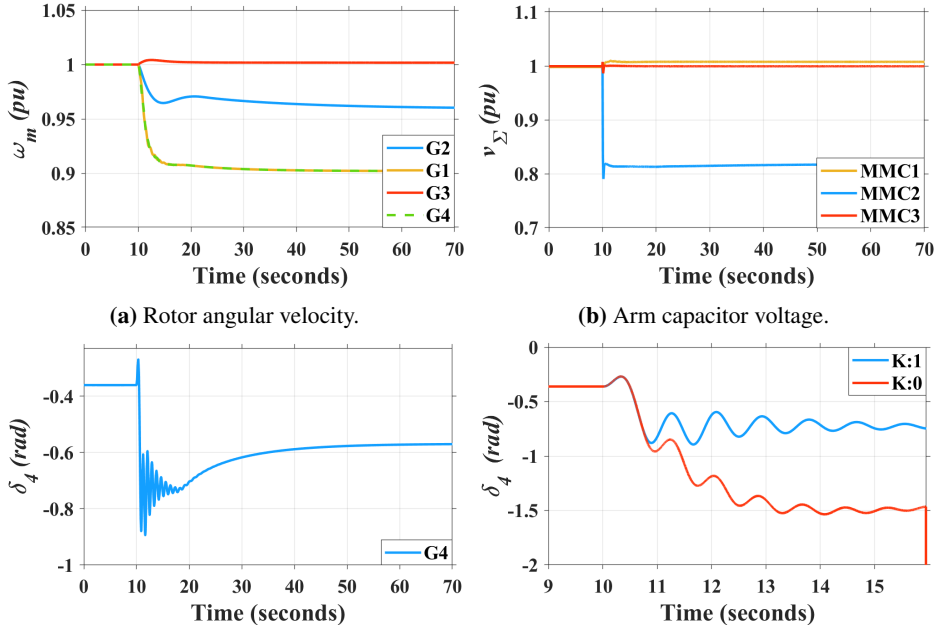

(a) Rotor angular velocity.

(b) Arm capacitor voltage.

(c) Rotor angular position.

(d) Rotor angular position. $\mathbf{K} = 1/0$ is with/without decentralized optimal controller, respectively.

Figure 6.12: Decentralized optimal controller performance under the worst-case perturbation scenario, $\mathbf{x}_{0,worst}$, applied at $t = 10\ s$.

which are oscillating at the frequency related to the mode $\lambda_{1,2}$, settle in a much shorter time under the decentralized optimal controller. Fig. 6.14 presents the ω_{m1} waveform under the same fault at a higher fictitious clearing time of 5 s. It is evident from the figure that the decentralized optimal controller can significantly reduce the ω_{m1} fluctuations after the fault and improve the grid stability compared with the PSS1.

Since the three-phase short circuit fault is the worst type of fault from the stability point of view [117], it can be anticipated that the decentralized optimal controller can mostly be reliable in assuring stability under other types of faults with the same clearing time as the three-phase fault. Additionally, the optimal controller offers better performance than the conventional power system stabilizer in minimizing the oscillations under the three-phase short circuit fault condition.

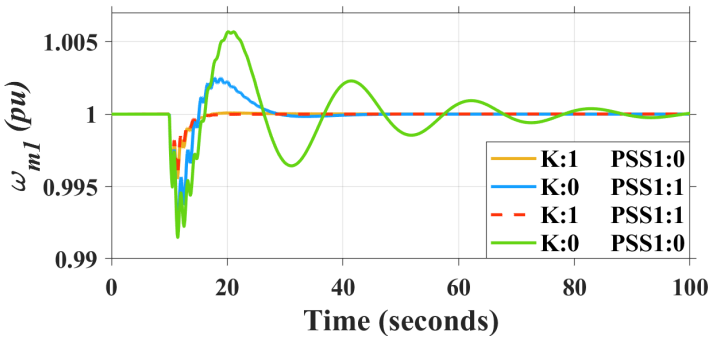

(a) Rotor angular velocity of G1.

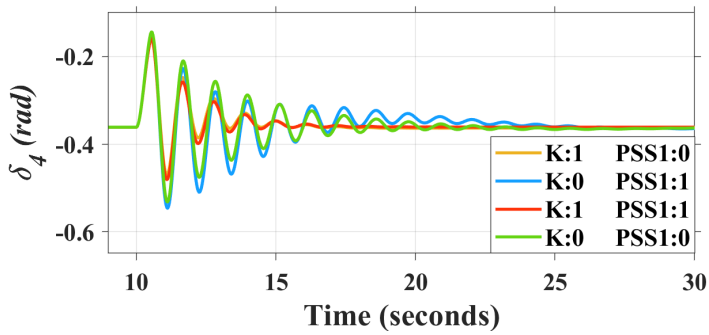

(b) Rotor angular position of G4.

Figure 6.13: Decentralized optimal controller performance under the three-phase short circuit fault at bus B2 applied at $t = 10\ s$ and cleared after 500 ms: (yellow) with decentralized optimal controller only, (blue) with PSS1 only, (red) with both decentralized optimal controller and PSS1, and (green) without both decentralized optimal controller and PSS1.

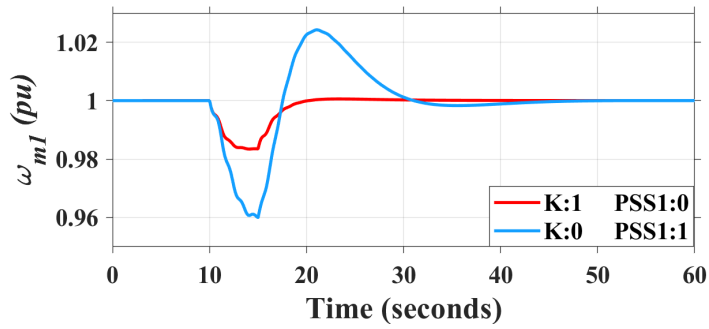

Figure 6.14: Performance comparison of the decentralized optimal controller and PSS1 under the three-phase short circuit fault at bus B2 applied at $t = 10\ s$ and cleared after 5 s.

6.5.4 Case study IV: Robustness against parameter and operating point uncertainties

This section analyzes the decentralized optimal controller's robustness in rejecting the impact of the parameter and operating point uncertainties. These uncertainties can arise from degradation, different operating and loading conditions, measurement errors, saturation, temperature variations, topology changes, and unmodeled fast dynamics of the switching devices [118]. Since the optimal controller is designed based on the overall state-space model of the grid and linearized around a particular operating condition, its capability to handle uncertainties should be investigated. Hence, the dynamic performance of the optimal controller is evaluated when it is subject to uncertainties in control parameters, grid parameters, and operating conditions under a 2% step increase to G1 reference rotor angular velocity at $t = 10\ s$ (disturbance on the generator side), and a 20% step increase to MMC1 reference AC-side active power at $t = 30\ s$ (disturbance on the converter side).

It is worth mentioning that the uncertainties considered in the grid parameters are fictitious and unrealistic since it is almost impossible to reach this level of parametric uncertainties in reality. However, the goal is to depict the robustness of the decentralized optimal controller to assure the grid's stability under disturbances in the presence of parametric uncertainties.

Robustness against control parameter uncertainties:

Control parameters may be poorly tuned without taking into account the interactions among grid equipment or need to be retuned due to grid reconfiguration. The two control parameters that have the highest impact on the grid's stability are the gains of the generator PSS1 and MMC1 droop controller.

Simulation results in Fig. 6.15 and 6.16 show the optimal controller dynamic performance when it is subject to control parameters other than the ones to which it is tuned. In Fig. 6.15, the PSS1 gain (-1) is divided and multiplied by five, resulting in gains of -0.2 and -5, respectively. As expected, the PSS1 gain variations affect the G1 rotor angular velocity more than the MMC1 arm capacitor voltage. Moreover, the PSS1 gain increase makes the grid more prone to instability, as previously shown in Fig. 6.6. On the other hand, Fig. 6.16 depicts the simulation results for MMC1 droop gain (0.1) variation by halving (0.05) and doubling (0.2) its value, which is a conventional and reasonable range for droop gain variation. The effect of the various MMC1 droop gains becomes apparent after the disturbance on the MMC1 reference AC-side active power at $t = 30\ s$ is applied. The increase in the MMC1 droop gain causes the waveforms to have higher overshoot at the moment of the disturbance on the MMC-side.

As is apparent from the figures, the decentralized optimal controller is robust enough to successfully perform and keep the grid stable under disturbances when there are uncertainties in the most critical control parameters.

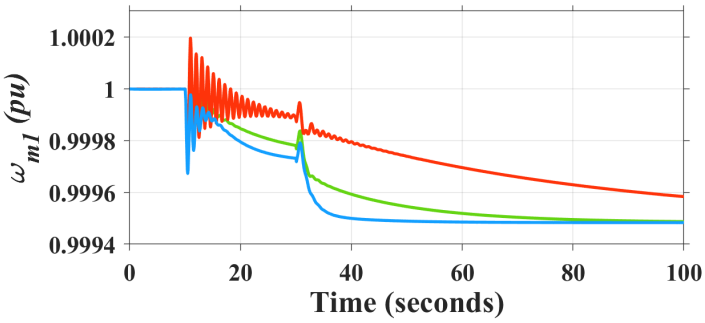

(a) Rotor angular velocity of G1.

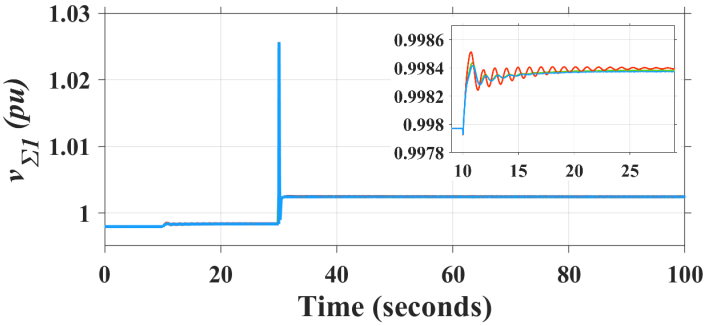

(b) Arm capacitor voltage of MMC1.

Figure 6.15: Decentralized optimal controller dynamic performance with PSS1 gain of: (green) G_1, (blue) G_1/5, and (red) G_1*5.

Robustness against grid parameter uncertainties:

Grid parameters may be wrongly measured/estimated or may vary due to degradation or equipment replacement. Hence, the robustness of the decentralized optimal controller is tested in this section against the uncertainties in the grid parameters, including the HVDC cable capacitance, MMC arm inductance, and generator synchronous reactance. Simulation results presented in Fig. 6.17, 6.18, and 6.19 demonstrate the dynamic performance of the optimal controller when parameter uncertainties occur on the AC- and DC-side of the grid.

As shown in Fig. 6.17, increase/decrease of the MMC1 DC-side capacitance by multiplying/dividing it by five has a negligible effect on ω_{m1} and $v_{\Sigma 1}$ waveforms. In other words, the uncertainty in the HVDC cable capacitance cannot cause in-

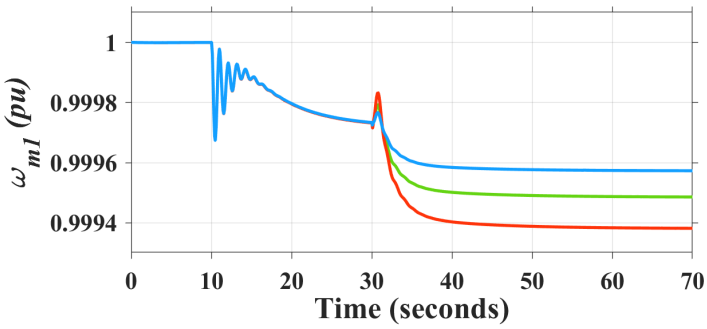

(a) Rotor angular velocity of G1.

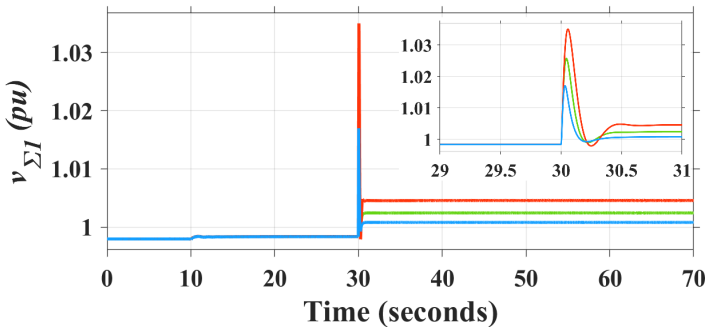

(b) Arm capacitor voltage of MMC1.

Figure 6.16: Decentralized optimal controller dynamic performance with MMC1 droop gain of: (green) D_1, (blue) D_1/2, and (red) D_1*2.

stability under the decentralized optimal controller performance. On the other hand, Fig. 6.18 and 6.19 depict the variation effect of the MMC1 arm inductance, L_{a1}, and G1 synchronous reactance, X_{d1}, on the decentralized optimal controller performance, respectively. As expected, the effect of the L_{a1} variation is more evident when the disturbance occurs on the converter side of the grid, whereas the disturbance on the generator side is more affected by the X_{d1} variation. In both cases, the optimal controller can keep the system stable under dynamics and transients.

Robustness against grid operating conditions:

Operating conditions can vary due to many reasons, including changes in grid source and load conditions. Since the decentralized optimal controller is designed under the operating condition depicted in Fig. 6.1, its robustness against operating point uncertainty is tested by 30% increase and decrease of the AC load active power at bus B2, L_{B2}. By the increase of the L_{B2}, the G1 active and reactive power

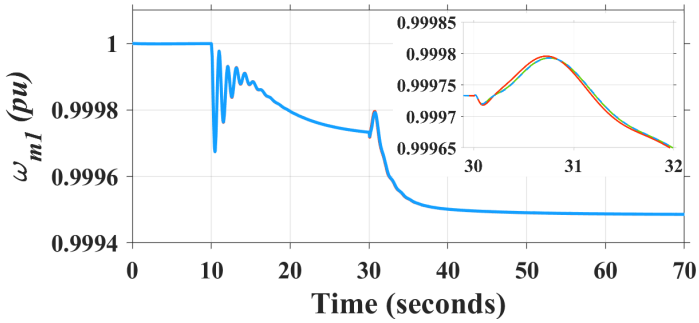

(a) Rotor angular velocity of G1.

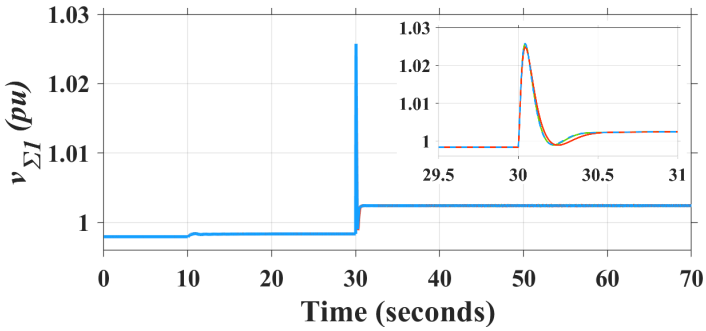

(b) Arm capacitor voltage of MMC1.

Figure 6.17: Decentralized optimal controller dynamic performance with MMC1 DC-side capacitance: (green) ($C_{dcl1} + C_{dc1}/2$), (blue) ($C_{dcl1} + C_{dc1}/2$)/5, and (red) ($C_{dcl1} + C_{dc1}/2$)*5.

become $P_{G1} = 909.4\ MW$ (44% increase) and $Q_{G1} = 57.4\ MVar$ while by the decrease of the L_{B2}, they become $P_{G1} = 338.5\ MW$ (46% decrease) and $Q_{G1} = -73.1\ MVar$, respectively. Simulation results are shown in Fig. 6.20. After exciting the electromechanical modes, $\lambda_{1,2}$, at $t = 10\ s$, the rotor angular velocity of G1 varies by a maximum of about 2%. However, the decentralized optimal controller shows that it can handle the uncertainties of the operating condition and assure the grid's stability.

6.6 Discussion

6.6.1 Pros and cons of the proposed methodology

The possibility of assuring the stability of the interconnected and expanded MMC-based hybrid AC/DC grid without running multiple time-consuming dynamic simulations and repetitive tuning of the grid controllers is probably the most prominent

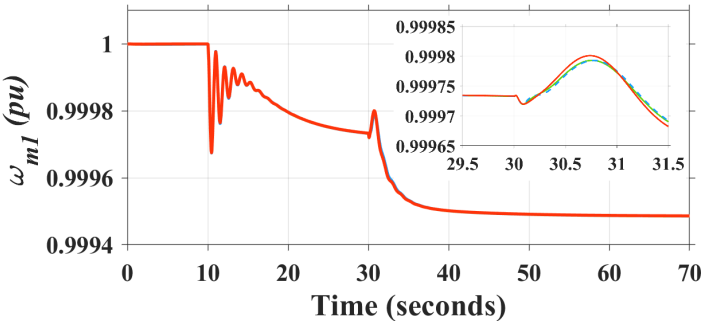

(a) Rotor angular velocity of G1.

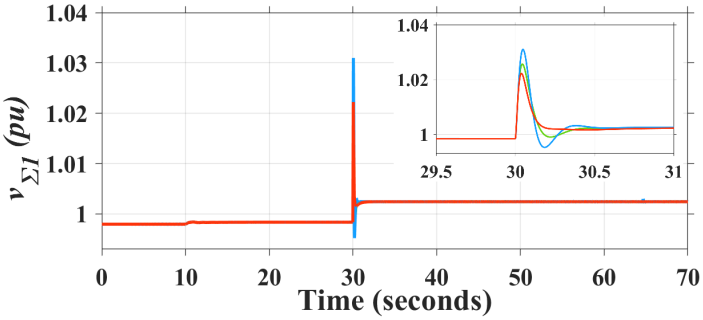

(b) Arm capacitor voltage of MMC1.

Figure 6.18: Decentralized optimal controller performance with MMC1 arm inductance of: (green) L_{a1}, (blue) L_{a1}/5, and (red) L_{a1}*5.

characteristic of the proposed decentralized optimal controller. This is because the controller is optimally designed under the grid worst-case perturbation/oscillation scenario and exhibits appropriate and satisfactory performance during normal operating conditions as well as small and large disturbances. Furthermore, once the controller is designed using the grid state-space model, its operation is only dependent on local communication at every converter station, owing to the controller's decentralized configuration.

As mentioned earlier, the decentralized optimal controller's operation depends on the availability of all the grid dynamic state variables. These state variables can be measured or estimated through the wide area measurement systems (WAMS), which can impose challenges due to the interoperability and presence of various operators and suppliers. Hence, measures are needed to run the controller successfully.

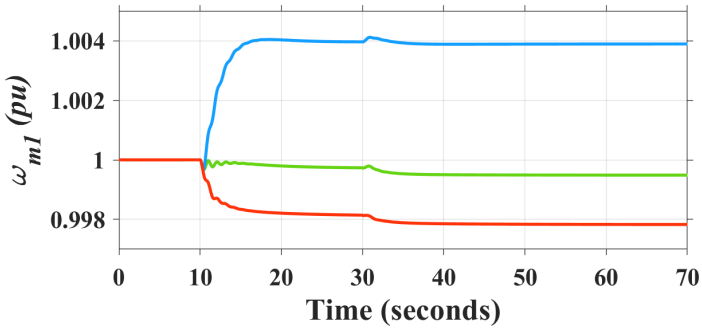

(a) Rotor angular velocity of G1.

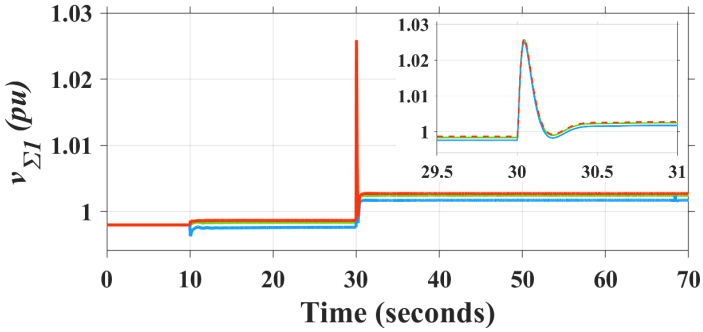

(b) Arm capacitor voltage of MMC1.

Figure 6.19: Decentralized optimal controller performance with G1 synchronous reactance of: (green) X_{d1}, (blue) X_{d1}/2, and (red) X_{d1}*2.

6.6.2 Scalability of the proposed methodology

The scalability of the proposed methodology can be evaluated considering the communication and computational requirements as well as the optimization methodology.

The performance of the decentralized optimal controller, which can improve the grid's stability under small and large dynamics and transients, is dependent on the zonal communication and computation of the grid's state variables, as can be seen in Fig. 6.3. Evidently, if the communication between the grid equipment and controller is lost in one zone, the decentralized optimal controller cannot function as intended in that zone. However, if the decentralized optimal controller is operating as an additional controller in the presence of the PSS and MMC droop controller, the loss of communication does not affect the conventional performance of the grid. The decentralized optimal controller can function properly again if the communication is restored. Notably, since the optimal controller is decentralized

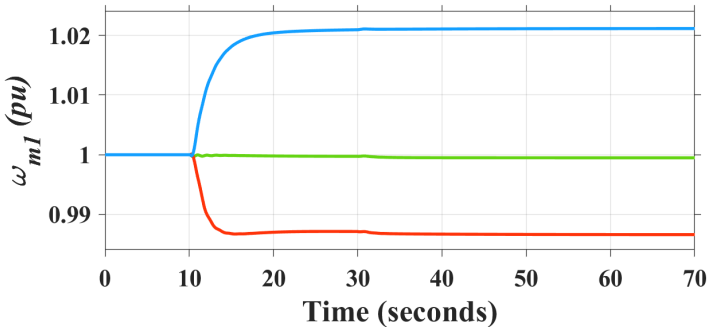

(a) Rotor angular velocity of G1.

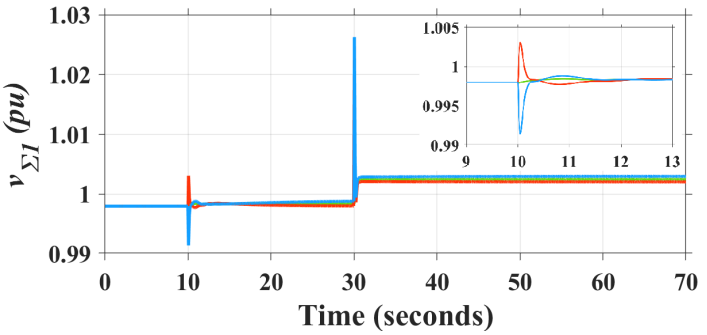

(b) Arm capacitor voltage of MMC1.

Figure 6.20: Decentralized optimal controller performance with load at bus B2 of: (green) L_{B2}, (blue) L_{B2}*0.7, and (red) L_{B2}*1.3.

(block-diagonal), an increase in the grid size does not affect the controller's performance.

On the other hand, the scalability of the proposed optimization problem is mostly dependent on the applied methodology. As mentioned earlier, the optimization formulation is approximated as a convex SDP problem using the Lyapunov stability and LMI theories. Hence, as long as the optimization methodology's inputs ($\mathbf{A}_{n\times n}$, $\mathbf{B}_{n\times m}$, and $\mathbf{C}_{n\times n}$) are available, and the optimization matrices ($\mathbf{E_x}^i$, $\mathbf{E_u}^j$, and Y) are reasonably tuned/selected, it should scale adequately with the grid size increase thanks to convexity and linearity. However, it should be noted that obtaining the optimization methodology's inputs, which are the grid state-space matrices, could be challenging when the number of the grid state variables increases and the system becomes large and highly complex. Moreover, if the optimization matrices are not tuned appropriately and reasonably, there might be convergence issues under some control inputs and state variables. Therefore, to improve the method-

ology's scalability in large-scale hybrid AC/DC grids, it might be necessary to further reduce the modeling order of the grid equipment.

6.6.3 Summary and conclusion

This chapter investigated the applicability of the decentralized optimal linear feedback controller in improving the stability margins and minimizing the oscillations caused by the poorly damped modes in an MMC-based multiterminal hybrid AC/DC grid. The optimal controller, which can be derived analytically, can assure the stability of the interconnected grid without the need for running time-consuming dynamic simulations and repetitive controllers' tuning. Furthermore, the controller's decentralized architecture can help avoid long-distance communication delays and failures threatening the network's reliability and stability.

Two pairs of poorly damped modes were found via the small-signal eigenvalue stability analysis ($\lambda_{1,2}$ and $\lambda_{3,4}$). One pair, $\lambda_{1,2}$, is an inter-area electromechanical mode associated with the generator's rotor angular velocity and position, whereas the other pair, $\lambda_{3,4}$, is linked with the MMC arm capacitor voltages. It was shown that the decentralized optimal controller can improve the damping ratio of the former pair (mode on the generator side) by 2.34 times and the latter one (mode on the converter side) by 4.05 times and enhance the stability margins of the grid by pushing these modes further away from the right half-plane ($\lambda_{1,2}$: from -0.27 to -0.67, and $\lambda_{3,4}$: from -2.13 to -10.54). Such phenomena would have been ignored if detailed models on both sides of the grid had not been applied.

Time-domain simulations revealed interactions and propagation of the oscillations and disturbances between the generator side (AC-side) and converter side (DC-side) of the grid. The state variables involved, which are the rotor angular velocity and position on the AC-side and MMC arm capacitor voltage on the DC-side, also contribute to the poorly damped modes of the grid and are very sensitive to the power system stabilizer (PSS) and MMC droop controller tuning parameters/gains. The higher these gains, the lower the grid stability margins, making the grid more prone to instability.

It was proved that the decentralized optimal controller can efficiently operate in the absence or presence of the PSS or droop controller to reduce the oscillations that occur due to the poorly damped modes' excitation and keep the system stable. In some cases, the optimal controller can take advantage of the energy stored in the MMC arm capacitors by manipulating the arm capacitor voltages to minimize the oscillations originating from the AC-side of the grid. It was also demonstrated that the optimal controller can ensure system stability under small and large disturbances and has better performance to limit the rotor angular velocity and po-

sition variations than the PSS under the three-phase short-circuit fault condition. Since this type of fault is the worst type from the stability point of view, it can be anticipated that the decentralized optimal controller can generally be reliable in guaranteeing stability under other types of faults.

Last but not least, the robustness of the decentralized optimal controller was evaluated against the uncertainties in control parameters, grid parameters, and operating conditions under the disturbances on the AC- and DC-side of the grid. The control parameters' uncertainties were modeled by varying the PSS gain and MMC droop gain. The grid parameters of interest are the generator synchronous reactance, MMC arm inductance, and DC-side capacitance. Additionally, an AC load was changed by $\pm 30\%$ to simulate the uncertainties in operating conditions. It was shown that the decentralized optimal controller is robust enough to keep the grid stable under disturbances when it is subject to all the abovementioned uncertainties.

The discussion in this chapter is supported by the following contribution by the author:

A. Elahidoost and E. Tedeschi, "Stability improvement of MMC-based hybrid AC/DC grids through the application of a decentralized optimal controller," *IET Gener. Transm. Distrib.* 00, 1– 19 (2022), doi: 10.1049/gtd2.12497 [20].

Chapter 7

Conclusions and future work

The main conclusions drawn from the findings and contributions of this thesis, together with suggestions for future work, are presented in this chapter.

7.1 Conclusions

This thesis has presented an optimal analytical methodology to improve the stability of the multiterminal HVDC grids, focusing on offshore wind applications. The analysis was performed in MMC-based HVDC grids, the preferred offshore technology, to account for the converter's control and dynamics challenges and opportunities originating from the arm capacitor energies. First, a centralized optimal linear feedback controller was introduced to ensure network stability under the worst-case perturbation scenario. Second, the centralized optimal controller was developed to be decentralized to eliminate the need for communication among converter stations to enhance the controller reliability. Furthermore, the optimization problem formulation was improved to decouple the control inputs and state variable constraints, allowing for more practicality and tractability in design and control. Last but not least, a potential stability decision-support criterion was proposed that can be applicable to TEP problems by identifying the HVDC link placement with minimum oscillations caused by the poorly damped modes under the worst-case perturbation scenario.

Hence, the original primary contributions are summarized and discussed in the following subsections.

7.1.1 Presenting a centralized optimal linear feedback controller:

The main aim of the centralized optimal linear feedback controller is to minimize the oscillations caused by the poorly damped modes under the worst-case perturbation scenario while considering the constraints on the control inputs and state variables.

The optimization methodology is analytical, and its formulation is approximated as a convex SDP problem using the Lyapunov stability and LMI theories. The inputs to the optimization procedure are the state matrices, while the outputs from the optimization problem formulation are the optimal controller, stability (oscillation) index, and worst-case perturbation scenario. Namely, the optimal controller can be found by running the optimization problem formulation once without analyzing the time-consuming dynamic and transient time-domain simulations for different scenarios. Additionally, there will be no need to retune the grid controllers under the interconnection and expansion procedure since the optimal controller designed based on the new grid configuration can guarantee stability.

The optimal controller is obtained under the worst-case perturbation scenario, which is found under the control inputs and state variables constraints. That is, the square root of the sum of the squares of the disturbances on the initial states' perturbations and, similarly, the square root of the sum of the squares of the control inputs are constrained. Knowing the worst-case perturbation scenario can be of paramount importance in the expansion planning stages of the multiterminal HVDC grids.

DC voltage stability is essential in multiterminal HVDC grids since it is sensitive to power imbalances due to the intermittent nature of the wind energy or fault conditions on the interconnected AC/DC terminals. DC voltage stability can be jeopardized either by resonances triggered under specific modes of operation or due to the non-passive behavior of the VSCs that can be considered as a source of instability. Accordingly, the performance of the centralized optimal controller in minimizing the DC voltage oscillations has been investigated in this thesis. It is worth mentioning that the optimal controller performance was first tested on the 2-level VSC-based HVDC grid, and then, on the MMC-based configuration, to account for the control and stability complexities originating from the circulating currents and arm capacitor voltages in the preferred HVDC converter topology.

It has been observed from the small-signal eigenvalue stability analysis of the MMC-based multiterminal HVDC grid that the two eigenvalue pairs causing the DC voltage oscillations are related to the DC-side voltage and integral state of the AC-side active power, which are connected through the droop control gain.

In addition, the eigenvalue trajectory analysis for droop variations has depicted a trade-off between these two eigenvalue pairs. One eigenvalue pair's stability margins have improved, while the other pair has become more prone to instability by further moving towards the right half-plane. To this end, the proposed optimization methodology can be beneficial to readjust/substitute the droop gains optimally in multiterminal configuration to improve the DC voltage stability margins.

The time-domain simulations have revealed that the centralized optimal controllers can enhance the DC voltage stability under the worst-case perturbation scenario when implemented either in the presence or absence of the droop control gain. In either case, the converters' zero-sequence energy sum has changed to keep the grid power balanced by diverting the variations to the arm capacitors to meet the grid control inputs' and the state variables' constraints. In the former case, better performance is obtained because the synergies between the centralized optimal controller and the droop control function can result in the minimization of the DC voltage oscillations with larger stability margins. The droop controller alone would not ensure such stability. On the other hand, the possibility of having the centralized optimal controller operating in the presence of the droop control gain may pave the way to its selective action, i.e., the possibility of being activated when the worst-case perturbation scenario occurs.

7.1.2 Applying a decentralized optimal linear feedback controller:

The centralized optimal controller has been replaced with the decentralized one to have the desired block-diagonal sparsity pattern such that each block can correspond to a converter station with all the other inter-converter entries being zero. Hence, there is no need for long-distance data communication between converter stations, resulting in a more reliable solution. In the decentralized problem formulation, the constraints on the initial state variables' perturbations and control inputs can be decoupled, which is physically more practical and sensible.

Comparing the performance of the decentralized optimal controller with the centralized one in minimizing the DC voltage oscillations has revealed the pivotal role of the converters' zero-sequence energy sum control under the decentralized optimal controller. Namely, this controller keeps the DC-side voltages and AC-side active powers relatively constant after the worst-case scenario by transferring the perturbations to the MMC arm capacitors resulting in the variation of the converters' zero-sequence energy sum. Hence, its performance may strongly rely on an increased number of the MMC sub-modules or a higher voltage rating of the MMC sub-module capacitors.

This thesis has investigated the applicability and feasibility of the decentralized

optimal controller in reducing oscillations caused by the poorly damped modes under the worst-case perturbation scenario and decoupled grid control inputs' and state variables' constraints in MMC-based multiterminal hybrid AC/DC grids.

Two pairs of the poorly damped modes have been found via the small-signal eigenvalue stability analysis: an inter-area electromechanical mode associated with the generator's rotor angular velocity and position (generator side) and a pair linked with the MMC arm capacitor voltages (converter side). Such phenomena would have been ignored if detailed models on both sides of the grid had not been implemented. Furthermore, the converter modeling simplifications that are typical in stability analysis and TEP problems can overlook the MMC arm capacitor energy significance. On the one hand, the MMC arm capacitor energy can contribute to dampen the oscillations through an optimal controller; on the other hand, it can be associated with the grid's poorly damped modes. Hence, an efficient controller such as the decentralized optimal controller can take advantage of the MMC arm capacitor energy in favor of its control goals.

It has been shown via the small-signal eigenvalue stability analysis that the decentralized optimal controller can significantly enhance the damping ratio and stability margins of the abovementioned poorly damped modes in the MMC-based multiterminal hybrid AC/DC grids.

Interactions and propagation of oscillations and disturbances between the grid's generator side (AC-side) and converter side (DC-side) have been revealed through the time-domain simulations. The state variables involved, which are the rotor angular velocity and position on the AC-side and MMC arm capacitor voltage on the DC-side, also contribute to the poorly damped modes of the grid and are very sensitive to the PSS and MMC droop controller tuning parameters/gains. The higher these gains, the lower the grid stability margins, making the grid more prone to instability.

It has been proved through the time-domain simulations that the decentralized optimal controller can efficiently operate in the absence or presence of the PSS or droop controller to reduce the oscillations that occur due to the poorly damped modes' excitation. It has also been demonstrated that the decentralized optimal controller can ensure grid stability under small and large disturbances and has better performance than the PSS under the three-phase short-circuit fault condition. Last but not least, it has been demonstrated that the decentralized optimal controller is robust enough to keep the grid stable against the uncertainties in control parameters, grid parameters, and operating conditions under the disturbances on the AC- and DC-side of the grid.

7.1.3 Introducing a stability-based decision-support criterion for TEP analysis:

A stability (oscillation) index has been introduced in this thesis that can be integrated into the TEP problems as a further decision-support criterion in the preliminary stages of expansion planning in multiterminal HVDC grids. This index can identify the HVDC link placement among several options with minimum oscillations on critical and poorly damped state variables under the worst-case perturbation scenario.

For instance, the DC voltage oscillation index was applied as a potential decision-support criterion for placing a new HVDC link between two independent point-to-point MMC-based offshore HVDC grids while considering the wind intermittency effect on grid operating conditions. It has been noted in this case study that the lowest oscillation index was obtained for the HVDC cable with the shortest length. The HVDC cable stability margin is expected to increase with the cable length. Hence, the results, in this case, suggest that the optimal controller's effectiveness in minimizing the DC voltage oscillations increases at lower stability margins. Namely, the shorter the cable length, the lower the DC voltage oscillation index with the centralized optimal controller.

7.2 Future work

The potential research directions for further work in the area of this thesis are as follows:

Verification of the optimal controller via PHIL: The feasibility and practicality of the proposed methodology can be further investigated through the experimental tests. Namely, the performance of the optimal controller can be analyzed using one (or more) physical MMCs in the Power Hardware In the Loop (PHIL) setting to simulate the realistic grid conditions.

Elaboration on interaction/coordination between the optimal controller and ancillary services: As a general rule, ancillary services such as frequency/inertia regulation, voltage regulation, and Power Oscillation Damping (POD) are required to maintain the reliable, secure, and stable operation of the interconnected power systems. Hence, it would interesting investigate the performance of the optimal controller in the presence or absence of these ancillary services, and to further elaborate on the interaction/coordination between them in multiterminal HVDC grids.

Benchmarking the optimal controller performance against other decentralized controllers: Apart from the qualitative comparison of the optimal controller's

characteristics with other controllers presented in chapter 6, a further assessment of the decentralized optimal controller can be carried out through benchmarking its performance against other relevant decentralized controllers, such as the ones proposed in [80, 84, 112].

Appendix A

Modulus optimum and symmetrical optimum tuning formulations

In the modulus optimum methodology, the PI controller proportional and integral gains can be tuned as follows:

$$k_i = \frac{1}{2bT_2} \qquad k_p = T_1 k_i \tag{A.1}$$

where in the case of the inner-loop AC-side current control, $b = \frac{1}{r_{ac}}$, $T_1 = \frac{l_{ac}}{r_{ac}}$, and $T_2 = T_{conv}$.

In the symmetrical optimum methodology, the PI controller proportional and integral gains can be tuned as below:

$$k_i = \frac{1}{a^3 b T_1^2} \qquad k_p = a^2 T_1 k_i \tag{A.2}$$

where in the case of the outer-loop control, $a = 2.41$, $b = \frac{v_{g,d}}{(c_{eq}+c_{dc}/2)v_{dc}}$, and $T_1 = 2T_{conv}$.

Appendix B

Optimization vectors and matrices for the 2L-VSC-based four-terminal HVDC grid

The optimization vectors and matrices for the 2L-VSC-based four-terminal HVDC grid that have not been given in the thesis chapter in the interest of brevity are presented in this appendix. To this end, the scenario with the added HVDC link of 1-4, d-component AC-side reference currents of $i^*_{ac,d1} = -0.875$, $i^*_{ac,d2} = 0.75$, $i^*_{ac,d3} = -0.875$, and $i^*_{ac,d4} = 1$, and DC voltage oscillation index of $\tilde{J}_{osci} = 4.25$ are considered.

The symmetric positive definite matrices ${\mathbf{E_u}}^j$, $\forall j \in \mathbb{Z}_{[1,q]}$ ($q = 4$) that are chosen to be diagonal matrices and should comply with (4.8) while enforcing the control input constraint of $\left((\Delta i^*_{ac,d})^2 + (\Delta i^*_{ac,q})^2\right)^{1/2} \leq 0.5$ pu are defined as follows:

$$ {\mathbf{E_u}}^j = \begin{bmatrix} 4 & 0 \\ 0 & 4 \end{bmatrix} \tag{B.1} $$

Similarly, the symmetric positive definite matrices ${\mathbf{E_x}}^i$, $\forall i \in \mathbb{Z}_{[1,r]}$ ($r = 15$) that are also chosen to be diagonal matrices and impose constraints (4.7) on the maximum allowed deviations of the initial state variables (4.39)-(4.42) are written as below:

$$ {\mathbf{E_x}}^i = \begin{bmatrix} 100 & 0 \\ 0 & 100 \end{bmatrix} \tag{B.2} $$

where enforces the constraint $\left((\Delta i_{ac,d})^2 + (\Delta i_{ac,q})^2\right)^{1/2} \leq 0.1$ pu.

$$\mathbf{E_x}^i = 100 \tag{B.3}$$

where enforces the constraints $|\Delta v_{dc}| \leq 0.1$ pu and $|\Delta i_{dc}| \leq 0.1$ pu.

$$\mathbf{E_x}^i = \begin{bmatrix} 10000 & 0 \\ 0 & 10000 \end{bmatrix} \tag{B.4}$$

where enforces the constraint $\left((\Delta\xi_{iacd})^2 + (\Delta\xi_{iacq})^2\right)^{1/2} \leq 0.01$ pu.

Hence, the worst initial perturbation scenario, $\mathbf{\Delta x_{0,worst}}$, is obtained such that the vector entries are at the boundary of the state variables' limit due to their decoupled confinement as mentioned above.

$$\begin{aligned}\mathbf{\Delta x_{0,worst}} = \big[&0.1 \quad 0 \quad 0.1 \quad 0.01 \quad 0 \quad -0.1 \quad 0 \quad 0.1 \quad 0.01 \quad 0 \quad 0.1 \quad 0.1 \\ &0 \quad 0.1 \quad 0.01 \quad 0 \quad 0.1 \quad 0 \quad 0.1 \quad 0.01 \quad 0 \quad 0.1 \quad 0.1\big]^T\end{aligned} \tag{B.5}$$

The resultant decentralized optimal controller, $\mathbf{K}$, is an 8×23 block-diagonal matrix where only the matrix entries associated with the converter stations and HVDC cables' connections are non-zero.

$$\mathbf{K} = \begin{bmatrix}
-0.11 & \approx 0 & 0.29 & -10.62 & \approx 0 & 0 & 0 & 0 & 0 & 0 & 0.002 & \\
\approx 0 & \approx 0 & \approx 0 & \approx 0 & -0.008 & 0 & 0 & 0 & 0 & 0 & \approx 0 & \\
0 & 0 & 0 & 0 & 0 & -0.002 & \approx 0 & 1.88 & -2.4 & \approx 0 & 0.006 & \\
0 & 0 & 0 & 0 & 0 & \approx 0 & \approx 0 & \approx 0 & \approx 0 & -0.008 & \approx 0 & \\
0 & 0 & 0 & 0 & 0 & 0 & 0 & 0 & 0 & 0 & 0 & \\
0 & 0 & 0 & 0 & 0 & 0 & 0 & 0 & 0 & 0 & 0 & \\
0 & 0 & 0 & 0 & 0 & 0 & 0 & 0 & 0 & 0 & 0 & \\
0 & 0 & 0 & 0 & 0 & 0 & 0 & 0 & 0 & 0 & 0 & \\
0 & 0 & 0 & 0 & 0 & 0 & 0 & 0 & 0 & 0 & 0 & -0.001 \\
0 & 0 & 0 & 0 & 0 & 0 & 0 & 0 & 0 & 0 & 0 & \approx 0 \\
0 & 0 & 0 & 0 & 0 & 0 & 0 & 0 & 0 & 0 & 0 & 0 \\
0 & 0 & 0 & 0 & 0 & 0 & 0 & 0 & 0 & 0 & 0 & 0 \\
-0.07 & \approx 0 & 0.36 & -9.23 & \approx 0 & 0 & 0 & 0 & 0 & 0 & 0.008 & 0 \\
\approx 0 & \approx 0 & \approx 0 & \approx 0 & -0.008 & 0 & 0 & 0 & 0 & 0 & \approx 0 & 0 \\
0 & 0 & 0 & 0 & 0 & -0.005 & \approx 0 & 3.5 & -4.61 & \approx 0 & 0.008 & -0.09 \\
0 & 0 & 0 & 0 & 0 & \approx 0 & \approx 0 & \approx 0 & \approx 0 & -0.008 & \approx 0 & \approx 0
\end{bmatrix} \tag{B.6}$$

Bibliography

[1] W. Zappa, M. Junginger, and M. van den Broek, "Is a 100% renewable european power system feasible by 2050?" *Applied Energy*, vol. 233-234, pp. 1027–1050, 2019. [Online]. Available: https://www.sciencedirect.com/science/article/pii/S0306261918312790

[2] O. Antoine, L. Papangelis, S. Michels Alfaro, A. Guittonneau, and A. Bertinato, "Technical requirements for connection to hvdc grids in the north sea," European Commission, B-1049 Brussels, Tech. Rep., 2020. [Online]. Available: https://op.europa.eu/en/publication-detail/-/publication/52f264ac-255f-11eb-9d7e-01aa75ed71a1/language-en

[3] M. Wang, T. An, H. Ergun, Y. Lan, B. Andersen, M. Szechtman, W. Leterme, J. Beerten, and D. Van Hertem, "Review and outlook of hvdc grids as backbone of transmission system," *CSEE Journal of Power and Energy Systems*, vol. 7, no. 4, pp. 797–810, 2021.

[4] L. Zhang, Y. Zou, J. Yu, J. Qin, V. Vittal, G. G. Karady, D. Shi, and Z. Wang, "Modeling, control, and protection of modular multilevel converter-based multi-terminal hvdc systems: A review," *CSEE Journal of Power and Energy Systems*, vol. 3, no. 4, pp. 340–352, 2017.

[5] W.-h. Xu, J.-z. Cao, X.-g. Wei, K.-p. Zha, and G.-f. Tang, "The development and type test of ±1100kv/5000a uhvdc valve," in *2012 Asia-Pacific Power and Energy Engineering Conference*, 2012, pp. 1–4.

[6] H. Rao, Y. Zhou, S. Xu, and Z. Zhu, "Research and development of ultra-high-voltage vsc for the multi-terminal hybrid ±800kv hvdc project in china southern power grid," in *Proceeding of Cigre ´Paris Session*, Paris, France, 2018, pp. 23–28.

[7] A. Dekka, B. Wu, R. L. Fuentes, M. Perez, and N. R. Zargari, "Evolution of topologies, modeling, control schemes, and applications of modular multilevel converters," *IEEE Journal of Emerging and Selected Topics in Power Electronics*, vol. 5, no. 4, pp. 1631–1656, 2017.

[8] J. A. Ansari, C. Liu, and S. A. Khan, "Mmc based mtdc grids: A detailed review on issues and challenges for operation, control and protection schemes," *IEEE Access*, vol. 8, pp. 168 154–168 165, 2020.

[9] A. Elahidoost and E. Tedeschi, "Expansion of offshore hvdc grids: An overview of contributions, status, challenges and perspectives," in *2017 IEEE 58th International Scientific Conference on Power and Electrical Engineering of Riga Technical University (RTUCON)*, 2017, pp. 1–7.

[10] X. Li, Z. Yuan, J. Fu, Y. Wang, T. Liu, and Z. Zhu, "Nanao multi-terminal vsc-hvdc project for integrating large-scale wind generation," in *2014 IEEE PES General Meeting | Conference Exposition*, 2014, pp. 1–5.

[11] Y. Wang, Z. Yuan, and J. Fu, "A novel strategy on smooth connection of an offline mmc station into mtdc systems," *IEEE Transactions on Power Delivery*, vol. 31, no. 2, pp. 568–574, 2016.

[12] "Making the most of europe's grids: Grid optimization technologies to build a greener europe," Wind Europe, September 2020. [Online]. Available: "https://windeurope.org/intelligence-platform/product/making-the-most-of-europe-s-grids/#overview"

[13] J. L. Rueda, W. H. Guaman, J. C. Cepeda, I. Erlich, and A. Vargas, "Hybrid approach for power system operational planning with smart grid and small-signal stability enhancement considerations," *IEEE Transactions on Smart Grid*, vol. 4, no. 1, pp. 530–539, 2013.

[14] A. Fuchs and M. Morari, "Actuator performance evaluation using lmis for optimal hvdc placement," in *2013 European Control Conference (ECC)*, 2013, pp. 1529–1534.

[15] ——, "Placement of hvdc links for power grid stabilization during transients," in *2013 IEEE Grenoble Conference*, 2013, pp. 1–6.

[16] A. Elahidoost, L. Furieri, E. Tedeschi, and M. Kamgarpour, "Optimizing hvdc grid expansion and control for enhancing dc stability," in *2018 Power Systems Computation Conference (PSCC)*, 2018, pp. 1–7.

[17] A. Elahidoost, L. Furieri, E. Tedeschi, and M. Kamgarpour, "Reducing hvdc network oscillations considering wind intermittency through optimized grid expansion decision," in *2018 IEEE Energy Conversion Congress and Exposition (ECCE)*, 2018, pp. 2683–2690.

[18] A. Elahidoost and E. Tedeschi, "Control optimization of the offshore hvdc grid based on modular multilevel converter for improving dc voltage stability," 18^{th} *International Conference on Renewable Energies and Power Quality (ICREPQ'20), later republished in The Renewable Energy and Power Quality Journal (RE&PQJ)*, vol. 18, pp. 207–212, 2020, cited By 1. [Online]. Available: https://www.scopus.com/inward/record.uri?eid=2-s2.0-85091679462&doi=10.24084%2frepqj18.273&partnerID=40&md5=3694c97475452bd42f185a559cfdbf41

[19] A. Elahidoost, L. Furieri, M. Kamgarpour, and E. Tedeschi, "Optimal linear controller for minimizing dc voltage oscillations in mmc-based offshore multiterminal hvdc grids," *IEEE Access*, vol. 9, pp. 98 731–98 745, 2021.

[20] A. Elahidoost and E. Tedeschi, "Stability improvement of mmc-based hybrid ac/dc grids through the application of a decentralized optimal controller," *IET Generation, Transmission & Distribution*, vol. 16, no. 15, pp. 3050–3068, 2022. [Online]. Available: https://ietresearch.onlinelibrary.wiley.com/doi/abs/10.1049/gtd2.12497

[21] "Energy revolution: A sustainable world energy outlook 2015, 100% renewable energy for all," GWEC: Global Wind Energy Council, Solar Power Europe, Green Peace, Sptember 2015. [Online]. Available: "https://wayback.archive-it.org/9650/20200416202821/http://p3-raw.greenpeace.org/international/Global/international/publications/climate/2015/Energy-Revolution-2015-Full.pdf"

[22] "Energy roadmap 2050: Impact assessment and scenario analysis," European Commission, 2011. [Online]. Available: "https://ec.europa.eu/energy/sites/ener/files/documents/roadmap2050_ia_20120430_en_0.pdf"

[23] "Re-thinking 2050: A 100% renewable energy vision for the european union," EREC: Eropean Renewable Energy Council, April 2010. [Online]. Available: "https://warwick.ac.uk/fac/soc/pais/research/csgr/green/foresight/energyenvironment/2010_erec_rethinkhing_2050.pdf"

[24] "Energy roadmap 2050," European Commission, 2012. [Online]. Available: "https://ec.europa.eu/energy/sites/ener/files/documents/2012_energy_roadmap_2050_en_0.pdf"

[25] A. Nami, J. Liang, F. Dijkhuizen, and G. D. Demetriades, "Modular multilevel converters for hvdc applications: Review on converter cells and functionalities," *IEEE Transactions on Power Electronics*, vol. 30, no. 1, pp. 18–36, 2015.

[26] A. Lesnicar and R. Marquardt, "An innovative modular multilevel converter topology suitable for a wide power range," in *2003 IEEE Bologna Power Tech Conference Proceedings,*, vol. 3, 2003, pp. 6 pp. Vol.3–.

[27] "Skagerrak HVDC grid fact sheet." [Online]. Available: "https://library.e.abb.com/public/d6886374d1134a02c1257dd500498dc8/POW0074%20Rev%201.pdf"

[28] "Troll A HVDC grid fact sheet." [Online]. Available: "https://library.e.abb.com/public/661c993a8c5b1f3bc1257e130044be18/POW0103_rev0.pdf?filename=POW0103_rev0.pdf"

[29] "NorNed HVDC grid fact sheet." [Online]. Available: "https://library.e.abb.com/public/e554905a1153efc2c1257c2f004b8304/NorNed_SEHVC%20M-063E.pdf"

[30] "Valhall HVDC grid fact sheet." [Online]. Available: "https://www.hitachienergy.com/references/hvdc/valhall"

[31] "BorWin1 HVDC grid fact sheet." [Online]. Available: "https://search.abb.com/library/Download.aspx?DocumentID=HVDC0068&LanguageCode=en&DocumentPartId=&Action=Launch"

[32] "BorWin2 HVDC grid fact sheet." [Online]. Available: "https://assets.new.siemens.com/siemens/assets/api/uuid:2c208787-94c1-42aa-a344-725ac2787dd4/factsheet-borwin2-en.pdf"

[33] "BorWin3 HVDC grid fact sheet." [Online]. Available: "https://assets.new.siemens.com/siemens/assets/api/uuid:dcc4289e-9325-4daf-9b29-f60e8ff3c194/Factsheet-BorWin3-en.pdf"

[34] "DolWin1 HVDC grid fact sheet." [Online]. Available: "https://library.e.abb.com/public/c1d7f2063ecb2966c1257c2f0043c99e/POW%200070%20Rev1%20LR.pdf"

[35] "DolWin2 HVDC grid fact sheet." [Online]. Available: "https://search.abb.com/library/Download.aspx?DocumentID=HVDC0064&LanguageCode=en&DocumentPartId=&Action=Launch"

[36] "DolWin3 HVDC grid fact sheet." [Online]. Available: "https://www.gegridsolutions.com/products/applications/hvdc/hvdc-vsc-dolwin3-case-study-en-2018-11-grid-pea-0578.pdf"

[37] "Caithness - Moray HVDC grid fact sheet." [Online]. Available: "https://library.e.abb.com/public/b81d2b00dd1d5d01c1257dda002653dd/POW0096%20rev%201.pdf"

[38] "Johan Sverdrup HVDC grid fact sheet." [Online]. Available: "https://library.e.abb.com/public/51e2841fc3ec5b01c1257e0e0025e78b/POW0099_rev0.pdf"

[39] "NordLink HVDC grid fact sheet." [Online]. Available: "https://www.hitachienergy.com/references/hvdc/nordlink"

[40] "North Sea Link (NSL) HVDC grid fact sheet." [Online]. Available: "https://library.e.abb.com/public/dffc67ed8a894573915bb34c5509254c/POW00105.pdf"

[41] "Dogger Bank HVDC grid fact sheet." [Online]. Available: "https://www.hitachienergy.com/references/hvdc/dogger-bank"

[42] "Shetland HVDC grid fact sheet." [Online]. Available: "https://www.hitachienergy.com/references/hvdc/shetland"

[43] "HVDC - High-voltage direct current transmission," Siemens. [Online]. Available: "https://assets.siemens-energy.com/siemens/assets/api/uuid:96c51c45-0ec8-4bdc-9531-29acfb134d9c/hvdc-referenzflyer.pdf"

[44] M. K. Bucher, R. Wiget, G. Andersson, and C. M. Franck, "Multiterminal hvdc networks—what is the preferred topology?" *IEEE Transactions on Power Delivery*, vol. 29, no. 1, pp. 406–413, 2014.

[45] A. Bayo Salas, "Control interactions in power systems with multiple vsc hvdc converters," Ph.D. thesis, KU Leuven, Leuven, Belgium, August 2018.

[46] A. Assegid Taffese, "Modeling, analysis, and control of mmc-based hvdc converters for grid services," Ph.D. thesis, Norwegian University of Science and Technology, Trondheim, Norway, February 2021.

[47] H. Akagi, "Classification, terminology, and application of the modular multilevel cascade converter (mmcc)," *IEEE Transactions on Power Electronics*, vol. 26, no. 11, pp. 3119–3130, 2011.

[48] L. Harnefors, A. Antonopoulos, S. Norrga, L. Angquist, and H.-P. Nee, "Dynamic analysis of modular multilevel converters," *IEEE Transactions on Industrial Electronics*, vol. 60, no. 7, pp. 2526–2537, 2013.

[49] A. Antonopoulos, L. Angquist, and H.-P. Nee, "On dynamics and voltage control of the modular multilevel converter," in *2009 13th European Conference on Power Electronics and Applications*, 2009, pp. 1–10.

[50] G. Bergna-Diaz, J. Freytes, X. Guillaud, S. D'Arco, and J. A. Suul, "Generalized voltage-based state-space modeling of modular multilevel converters with constant equilibrium in steady state," *IEEE Journal of Emerging and Selected Topics in Power Electronics*, vol. 6, no. 2, pp. 707–725, 2018.

[51] D. Jovcic and A. A. Jamshidifar, "Phasor model of modular multilevel converter with circulating current suppression control," *IEEE Transactions on Power Delivery*, vol. 30, no. 4, pp. 1889–1897, 2015.

[52] N.-T. Trinh, M. Zeller, K. Wuerflinger, and I. Erlich, "Generic model of mmc-vsc-hvdc for interaction study with ac power system," *IEEE Transactions on Power Systems*, vol. 31, no. 1, pp. 27–34, 2016.

[53] S. S. Khan and E. Tedeschi, "Modeling of mmc for fast and accurate simulation of electromagnetic transients: A review," *Energies*, vol. 10, no. 8, 2017. [Online]. Available: https://www.mdpi.com/1996-1073/10/8/1161

[54] G. Bergna-Diaz, J. A. Suul, and S. D'Arco, "Energy-based state-space representation of modular multilevel converters with a constant equilibrium point in steady-state operation," *IEEE Transactions on Power Electronics*, vol. 33, no. 6, pp. 4832–4851, 2018.

[55] Q. Tu, Z. Xu, and L. Xu, "Reduced switching-frequency modulation and circulating current suppression for modular multilevel converters," *IEEE Transactions on Power Delivery*, vol. 26, no. 3, pp. 2009–2017, 2011.

[56] G. Bergna Diaz, J. A. Suul, and S. D'Arco, "Small-signal state-space modeling of modular multilevel converters for system stability analysis," in *2015 IEEE Energy Conversion Congress and Exposition (ECCE)*, 2015, pp. 5822–5829.

[57] J. Freytes, L. Papangelis, H. Saad, P. Rault, T. Van Cutsem, and X. Guillaud, "On the modeling of mmc for use in large scale dynamic simulations," in *2016 Power Systems Computation Conference (PSCC)*, 2016, pp. 1–7.

[58] P. Kundur, *Power System Stability and Control*. New York, NY, USA: McGraw-Hill, 1994.

[59] J. Beerten, S. D'Arco, and J. A. Suul, "Frequency-dependent cable modelling for small-signal stability analysis of vsc-hvdc systems," *IET Generation, Transmission & Distribution*, vol. 10, no. 6, pp. 1370–1381, 2016. [Online]. Available: https://ietresearch.onlinelibrary.wiley.com/doi/abs/10.1049/iet-gtd.2015.0868

[60] S. D'Arco, J. A. Suul, and J. Beerten, "Analysis of accuracy versus model order for frequency-dependent pi-model of hvdc cables," in *2016 IEEE 17th Workshop on Control and Modeling for Power Electronics (COMPEL)*, 2016, pp. 1–8.

[61] A. Morched, B. Gustavsen, and M. Tartibi, "A universal model for accurate calculation of electromagnetic transients on overhead lines and underground cables," *IEEE Transactions on Power Delivery*, vol. 14, no. 3, pp. 1032–1038, 1999.

[62] B. Gustavsen and A. Semlyen, "Rational approximation of frequency domain responses by vector fitting," *IEEE Transactions on Power Delivery*, vol. 14, no. 3, pp. 1052–1061, 1999.

[63] "Guide for the development of models for HVDC converters in a HVDC grid," Technical Brochures WG B4.57, 2014.

[64] V. Kaura and V. Blasko, "Operation of a phase locked loop system under distorted utility conditions," in *Proceedings of Applied Power Electronics Conference. APEC '96*, vol. 2, 1996, pp. 703–708 vol.2.

[65] S. D'Arco, J. A. Suul, and M. Molinas, "Implementation and analysis of a control scheme for damping of oscillations in vsc-based hvdc grids," in *2014 16th International Power Electronics and Motion Control Conference and Exposition*, 2014, pp. 586–593.

[66] J. Umland and M. Safiuddin, "Magnitude and symmetric optimum criterion for the design of linear control systems: what is it and how does it compare with the others?" *IEEE Transactions on Industry Applications*, vol. 26, no. 3, pp. 489–497, 1990.

[67] A. Gualu Endegnanew, "Stability analysis of high voltage hybrid ac/dc power systems," Ph.D. thesis, Norwegian University of Science and Technology, Trondheim, Norway, September 2017.

[68] J. Machowski, Z. Lubosny, J. Bialek, and J. Bumby, *Power System Dynamics: Stability and Control*. Wiley, 2020. [Online]. Available: https://books.google.no/books?id=LZwmyAEACAAJ

[69] D. Mondal, A. Chakrabarti, and A. Sengupta, *Power System Small Signal Stability Analysis and Control*. Elsevier Science, 2014. [Online]. Available: https://books.google.no/books?id=v7Y1nwEACAAJ

[70] K. Ogata, *Modern Control Engineering*, ser. Instrumentation and controls series. Prentice Hall, 2010. [Online]. Available: https://books.google.no/books?id=Wu5GpNAelzkC

[71] P. Sauer and M. Pai, *Power System Dynamics and Stability*. Prentice Hall, 1998. [Online]. Available: https://books.google.no/books?id=dO0eAQAAIAAJ

[72] R. Shah, J. C. Sánchez, R. Preece, and M. Barnes, "Stability and control of mixed ac–dc systems with vsc-hvdc: a review," *IET Generation, Transmission & Distribution*, vol. 12, pp. 2207–2219(12), May 2018.

[73] G. Pinares and M. Bongiorno, "Analysis and mitigation of instabilities originated from dc-side resonances in vsc-hvdc systems," *IEEE Transactions on Industry Applications*, vol. 52, no. 4, pp. 2807–2815, 2016.

[74] A. A. Taffese, A. G. Endegnanew, S. D'Arco, and E. Tedeschi, "Power oscillation damping with virtual capacitance support from modular multilevel converters," *IET Renewable Power Generation*, vol. 14, no. 5, pp. 897–905, 2020. [Online]. Available: https://ietresearch.onlinelibrary.wiley.com/doi/abs/10.1049/iet-rpg.2019.0517

[75] W. Wang and M. Barnes, "Power flow algorithms for multi-terminal vsc-hvdc with droop control," *IEEE Transactions on Power Systems*, vol. 29, no. 4, pp. 1721–1730, 2014.

[76] C. Buchhagen, C. Rauscher, A. Menze, and J. Jung, "Borwin1 - first experiences with harmonic interactions in converter dominated grids," in *International ETG Congress 2015; Die Energiewende - Blueprints for the new energy age*, 2015, pp. 1–7.

[77] H. Saad, Y. Fillion, S. Deschanvres, Y. Vernay, and S. Dennetière, "On resonances and harmonics in hvdc-mmc station connected to ac grid," *IEEE Transactions on Power Delivery*, vol. 32, no. 3, pp. 1565–1573, 2017.

[78] Q. Zhou, Y. Ding, K. Mai, X. Bian, and B. Zhou, "Mitigation of subsynchronous oscillation in a vsc-hvdc connected offshore wind farm integrated to grid," *International Journal of Electrical Power & Energy Systems*, vol. 109, pp. 29–37, 2019. [Online]. Available: https://www.sciencedirect.com/science/article/pii/S0142061518326711

[79] C. Yin, X. Xie, S. Xu, and C. Zou, "Review of oscillations in vsc-hvdc systems caused by control interactions," *The Journal of Engineering*, vol. 2019, no. 16, p. 1204–1207, March 2019.

[80] A. J. Agbemuko, J. L. Domínguez-García, and O. Gomis-Bellmunt, "Impedance-based modelling of hybrid ac/dc grids with synchronous generator for interaction study and dynamic improvement," *Electric Power Systems Research*, vol. 179, p. 106086, 2020. [Online]. Available: https://www.sciencedirect.com/science/article/pii/S0378779619304055

[81] J. C. Gonzalez-Torres, G. Damm, V. Costan, A. Benchaib, and F. Lamnabhi-Lagarrigue, "Transient stability of power systems with embedded vsc-hvdc links: stability margins analysis and control," *IET Generation, Transmission & Distribution*, vol. 14, no. 17, pp. 3377–3388, 2020. [Online]. Available: https://ietresearch.onlinelibrary.wiley.com/doi/abs/10.1049/iet-gtd.2019.1074

[82] L. Dewangan and H. J. Bahirat, "Controller interaction and stability margins in mixed scr mmc-based hvdc grid," *IEEE Transactions on Power Systems*, vol. 35, no. 4, pp. 2835–2846, 2020.

[83] A. Fuchs, M. Imhof, T. Demiray, and M. Morari, "Stabilization of large power systems using vsc–hvdc and model predictive control," *IEEE Transactions on Power Delivery*, vol. 29, no. 1, pp. 480–488, 2014.

[84] J. C. Gonzalez-Torres, G. Damm, V. Costan, A. Benchaib, and F. Lamnabhi-Lagarrigue, "A novel distributed supplementary control of multi-terminal vsc-hvdc grids for rotor angle stability enhancement of ac/dc systems," *IEEE Transactions on Power Systems*, vol. 36, no. 1, pp. 623–634, 2021.

[85] Z. Zhuo, N. Zhang, J. Yang, C. Kang, C. Smith, M. J. O'Malley, and B. Kroposki, "Transmission expansion planning test system for ac/dc hybrid grid with high variable renewable energy penetration," *IEEE Transactions on Power Systems*, vol. 35, no. 4, pp. 2597–2608, 2020.

[86] M. Moradi-Sepahvand and T. Amraee, "Hybrid ac/dc transmission expansion planning considering hvac to hvdc conversion under renewable penet-

ration," *IEEE Transactions on Power Systems*, vol. 36, no. 1, pp. 579–591, 2021.

[87] H. Xie, Z. Bie, and G. Li, "Reliability-oriented networking planning for meshed vsc-hvdc grids," *IEEE Transactions on Power Systems*, vol. 34, no. 2, pp. 1342–1351, 2019.

[88] A. A. Eajal, A. H. Yazdavar, E. F. El-Saadany, and K. Ponnambalam, "On the loadability and voltage stability of islanded ac–dc hybrid microgrids during contingencies," *IEEE Systems Journal*, vol. 13, no. 4, pp. 4248–4259, 2019.

[89] J. Qiu, Z. Y. Dong, J. Zhao, Y. Xu, F. Luo, and J. Yang, "A risk-based approach to multi-stage probabilistic transmission network planning," *IEEE Transactions on Power Systems*, vol. 31, no. 6, pp. 4867–4876, 2016.

[90] H. Ergun, B. Rawn, R. Belmans, and D. Van Hertem, "Stepwise investment plan optimization for large scale and multi-zonal transmission system expansion," in *2016 IEEE Power and Energy Society General Meeting (PESGM)*, 2016, pp. 1–1.

[91] ——, "Technology and topology optimization for multizonal transmission systems," *IEEE Transactions on Power Systems*, vol. 29, no. 5, pp. 2469–2477, 2014.

[92] S. Boyd, L. EL Ghaoui, E. Feron, and V. Balakrishnan, *Linear Matrix Inequalities in System and Control Theory*. Philadelphia: SIAM Studies in Applied Mathematics, 1994, vol. 15.

[93] "Wind energy in europe: Scenarios for 2030," Wind Europe, September 2017. [Online]. Available: "https://windeurope.org/wp-content/uploads/files/about-wind/reports/Wind-energy-in-Europe-Scenarios-for-2030.pdf"

[94] A. A. van der Meer, M. Ndreko, J. A. Bos, M. Gibescu, M. A. M. M. van der Meijden, and W. L. Kling, "Stability assessment of vsc-hvdc connected large-scale offshore wind power: A north-sea region case study," in *2015 IEEE Eindhoven PowerTech*, 2015, pp. 1–6.

[95] M. Henderson, J. Gagnon, and D. Bertagnolli, "Planning issues for hvdc," in *2006 IEEE PES Power Systems Conference and Exposition*, 2006, pp. 28–32.

[96] W. Wang, M. Barnes, O. Marjanovic, and O. Cwikowski, "Impact of dc breaker systems on multiterminal vsc-hvdc stability," *IEEE Transactions on Power Delivery*, vol. 31, no. 2, pp. 769–779, 2016.

[97] G. Pinares, "Analysis of the dc dynamics of vsc-hvdc systems connected to weak ac grids using a frequency domain approach," in *2014 Power Systems Computation Conference*, 2014, pp. 1–7.

[98] H. Svendsen, "Hourly wind and solar energy time series from reanalysis dataset," SINTEF Energi AS, Norway, Tech. Rep., 2017. [Online]. Available: http://hdl.handle.net/11250/2468143

[99] I. Graabak, H. Svendsen, and M. Korpås, "Developing a wind and solar power data model for europe with high spatial-temporal resolution," in *2016 51st International Universities Power Engineering Conference (UPEC)*, 2016, pp. 1–6.

[100] W. Leterme, N. Ahmed, J. Beerten, L. Ängquist, D. V. Hertem, and S. Norrga, "A new hvdc grid test system for hvdc grid dynamics and protection studies in emt-type software," in *11th IET International Conference on AC and DC Power Transmission*, 2015, pp. 1–7.

[101] J. Lofberg, "Yalmip : a toolbox for modeling and optimization in matlab," in *2004 IEEE International Conference on Robotics and Automation (IEEE Cat. No.04CH37508)*, 2004, pp. 284–289.

[102] E. D. Andersen and K. D. Andersen, *The Mosek Interior Point Optimizer for Linear Programming: An Implementation of the Homogeneous Algorithm*. Boston, MA: Springer US, 2000, pp. 197–232. [Online]. Available: https://doi.org/10.1007/978-1-4757-3216-0_8

[103] R. Wachal, "Guide for the development of models for hvdc converters in a hvdc grid,," CIGRE, Working Group B4.57, Tech. Rep., December 2014.

[104] E. Prieto-Araujo, A. Egea-Alvarez, S. Fekriasl, and O. Gomis-Bellmunt, "Dc voltage droop control design for multiterminal hvdc systems considering ac and dc grid dynamics," *IEEE Transactions on Power Delivery*, vol. 31, no. 2, pp. 575–585, 2016.

[105] M. N. Ambia, K. Meng, W. Xiao, A. Al-Durra, and Z. Y. Dong, "Adaptive droop control of multi-terminal hvdc network for frequency regulation and power sharing," *IEEE Transactions on Power Systems*, vol. 36, no. 1, pp. 566–578, 2021.

[106] B. Zhang and H. Nademi, "Modeling and harmonic stability of mmc-hvdc with passive circulating current filters," *IEEE Access*, vol. 8, pp. 129 372–129 386, 2020.

[107] X. Chen, L. Wang, H. Sun, and Y. Chen, "Fuzzy logic based adaptive droop control in multiterminal hvdc for wind power integration," *IEEE Transactions on Energy Conversion*, vol. 32, no. 3, pp. 1200–1208, 2017.

[108] S. D. Tavakoli, E. Sánchez-Sánchez, E. Prieto-Araujo, and O. Gomis-Bellmunt, "Dc voltage droop control design for mmc-based multiterminal hvdc grids," *IEEE Transactions on Power Delivery*, vol. 35, no. 5, pp. 2414–2424, 2020.

[109] Government.no, "Norway opens offshore areas for wind power," 2020. [Online]. Available: "https://www.regjeringen.no/en/aktuelt/norway-opens-offshore-areas-for-wind-power/id2705986/"

[110] entsoe.eu, "Commission regulation (eu) 2016/1447 of 26 august 2016 establishing a network code on requirements for grid connection of high voltage direct current systems and direct current-connected power park modules," 2016. [Online]. Available: "http://data.europa.eu/eli/reg/2016/1447/oj"

[111] C. Guo, S. Yang, W. Liu, and C. Zhao, "Single-input–single-output feedback control model and stability margin analysis for hybrid dual-infeed hvdc system," *IEEE Journal of Emerging and Selected Topics in Power Electronics*, vol. 9, no. 3, pp. 3061–3071, 2021.

[112] Y. Zou, J. Qin, L. Zhang, and J. Yu, "Inequality constraints based method for fast estimation of droop slope stability regions for mmc-based mtdc systems," *IEEE Transactions on Power Delivery*, vol. 36, no. 6, pp. 3689–3700, 2021.

[113] C. Guo, P. Cui, and C. Zhao, "Optimization and configuration of control parameters to enhance small-signal stability of hybrid lcc-mmc hvdc system," *Journal of Modern Power Systems and Clean Energy*, vol. 10, no. 1, pp. 213–221, 2022.

[114] J. Lyu, X. Cai, and M. Molinas, "Optimal design of controller parameters for improving the stability of mmc-hvdc for wind farm integration," *IEEE Journal of Emerging and Selected Topics in Power Electronics*, vol. 6, no. 1, pp. 40–53, 2018.

[115] T. Huang, F. Yang, D. Zhang, and X. Chen, "High-frequency stability analysis and impedance optimization for an mmc-hvdc integrated system considering delay effects," *IEEE Journal on Emerging and Selected Topics in Circuits and Systems*, vol. 12, no. 1, pp. 59–72, 2022.

[116] S. Sanchez, G. Bergna, and E. Tedeschi, "Tuning of control loops for grid-connected modular multilevel converters under a simplified port representation for large system studies," in *2017 Twelfth International Conference on Ecological Vehicles and Renewable Energies (EVER)*, 2017, pp. 1–8.

[117] J. C. Das, *Short-Circuits in AC and DC Systems: ANSI, IEEE, and IEC Standards*. USA: CRC Press, Taylor & Francis Group, 2017.

[118] M. M. Belhaouane, M. Ayari, X. Guillaud, and N. B. Braiek, "Robust control design of mmc-hvdc systems using multivariable optimal guaranteed cost approach," *IEEE Transactions on Industry Applications*, vol. 55, no. 3, pp. 2952–2963, 2019.

ISBN 978-82-326-7614-9 (printed ver.)
ISBN 978-82-326-7613-2 (electronic ver.)
ISSN 1503-8181 (printed ver.)
ISSN 2703-8084 (online ver.)

NTNU

Norwegian University of
Science and Technology